Theory of lanthanide systems : valence transitions and interplay of Kondo effect and disorder

José Luiz Ferreira da Silva Jr

Communauté
UNIVERSITÉ Grenoble Alpes

THÈSE

Pour obtenir le grade de

DOCTEUR DE LA COMMUNAUTÉ UNIVERSITÉ GRENOBLE ALPES

Spécialité : **Physique de la matière condensée & rayonnement**

Arrêté ministériel : 7 août 2006

Présentée par

José Luiz FERREIRA DA SILVA JUNIOR

Thèse dirigée par **Claudine LACROIX** et
codirigée par **Sébastien BURDIN**

préparée au sein du **Laboratoire Institut Néel**
dans **l'École Doctorale de Physique**

Théorie des systèmes de lanthanide: transitions de valence et effet Kondo en présence de désordre

Thèse soutenue publiquement le **23 mars 2016**,
devant le jury composé de :

M. Daniel MALTERRE
Professeur, Institut Jean Lamour, CNRS et Université de Lorraine, Président du jury

Mme. Anuradha JAGANNATHAN
Professeure, Laboratoire de Physique des Solides, CNRS et Université Paris-Sud, Rapporteur

M. Indranil PAUL
Chargé de recherches, Laboratoire Matériaux et Phénomènes Quantiques, CNRS et Université Paris-Diderot, Rapporteur

Mme. Gertrud ZWICKNAGL
Professeure, Institut für Mathematische Physik, Technische Universität Braunschweig, Examinatrice

M. Ilya SHEIKIN
Directeur de recherches, Laboratoire National des Champs Magnétiques Intenses, CNRS et Université Grenoble Alpes, Examinateur

Mme. Claudine LACROIX
Directrice de recherches, Institut Néel, CNRS et Université Grenoble Alpes, Directrice de thèse

M. Sébastien BURDIN
Maître de conférences, Laboratoire Ondes et Matières d'Aquitaine (LOMA), CNRS et Université de Bordeaux, Co-Directeur de thèse

Abstract

The topics of the thesis concerns two theoretical aspects of the physics of 4f electron systems.

In the first part the topic of intermediate valence and valence transitions in lanthanide systems is explored. For that purpose, we study an extended version of the Periodic Anderson Model which includes the Coulomb interaction between conduction electrons and the localized f electrons (Falicov-Kimball interaction). If it is larger than a critical value, this interaction can transform a smooth valence change into a discontinuous valence transition. The model is treated in a combination of Hubbard-I and mean-field approximations, suitable for the energy scales of the problem. The zero temperature phase diagram of the model is established. It shows the evolution of the valence with respect to the model parameters. Moreover, the effects of an external magnetic field and ferromagnetic interactions on the valence transitions are investigated. Our results are compared to selected Yb- and Eu-based compounds, such as $\mathrm{YbCu_2Si_2}$, $\mathrm{YbMn_6Ge_{6-x}Sn_x}$ and $\mathrm{Eu(Rh_{1-x}Ir_x)_2Si_2}$.

In the second part of the thesis, we study lanthanide systems in which the number of local magnetic atoms is tuned by substitution of non-magnetic atoms, also known as Kondo Alloys. In such systems it is possible to go from the single Kondo impurity to the Kondo lattice regime, both characterized by different type of Fermi liquids. The Kondo Alloy model is studied within the Statistical Dynamical Mean-Field Theory, which treats different aspects of disorder and is formally exact in a Bethe lattice of any coordination number. The distributions of the mean-field parameters, the local density of states and other local quantities are presented as a function of model parameters, in particular the concentration of magnetic moments x, the number of conduction electrons per site n_c and the Kondo interaction strength J_K. Our results show a clear distinction between the impurity ($x \ll 1$) and the lattice ($x \approx 1$) regimes for a strong Kondo interaction. For intermediate concentrations ($x \approx n_c$), the system is dominated by disorder effects and indications of Non-Fermi liquid behavior and localization of electronic states are observed. These features disappear if the Kondo interaction is weak. We further discuss the issue of low dimensionality and its relation to the percolation problem in such systems.

Résumé

Cette thèse a comme sujet général l'etude théorique de deux aspects de la physique des systèmes d'electrons $4f$.

La première partie est consacrée aux systèmes intermétalliques de lanthanides à valence intermédiaire ou possédant une transition de valence. Dans ce but, nous étudions une version étendue du modèle d'Anderson périodique, auquel est ajoutée une interaction coulombienne entre les électrons de conduction et les électrons f localisés (intéraction de Falicov-Kimball). Si cette interaction est plus forte qu'une valeur critique, le changement de valence n'est plus continu, mais devient discontinu. Le modèle est traité par un ensemble de approximations appropriées aux échelles d'énergie du problème : Hubbard-I et le champ moyen. Le diagramme de phases du modèle à température nulle et l'évolution de la valence avec les paramètres du modèle sont déterminés. En plus, les effets d'un champ magnétique extérieur et des interactions ferromagnétiques entre les électrons localisés sont examinés. Nos résultats sont comparés à quelques composés à base de Yb et Eu, comme $\mathrm{YbCu_2Si_2}$, $\mathrm{YbMn_6Ge_{6-x}Sn_x}$ et $\mathrm{Eu(Rh_{1-x}Ir_x)_2Si_2}$.

Dans la deuxième partie nous étudions des systèmes de lanthanides dans lesquels le nombre d'atomes magnétiques localisés peut être modifié par substitution par des atomes non-magnétiques (Alliages Kondo). Dans ces systèmes il est possible de passer du régime d'impureté Kondo au régime de réseau Kondo ; à basse température ces deux régimes sont des liquides de Fermi dont les caractéristiques sont différentes. Le modèle d'alliage Kondo est étudié dans la théorie du champ moyen dynamique statistique, qui traite différents aspects du désordre et qui est formellement exacte dans un arbre de Bethe avec un nombre de coordination quelconque. Les distributions des paramètres de champ moyen, des densité d'états locales et d'autres quantités locales sont présentées en fonction des paramètres du modèle, en particulier la concentration de moments magnétiques x, le nombre d'électrons de conduction par site n_c, et la valeur de l'interaction Kondo J_K. Nos résultats montrent une différence nette entre les régimes d'impureté ($x \ll 1$) et de réseau ($x \approx 1$) pour une interaction Kondo forte. Pour des concentrations intermédiaires ($x \approx n_c$), le système est dominé par le désordre et des indications d'un comportement non-liquide de Fermi et d'une localisation des états électroniques sont observés. Ces caractéristiques disparaissent quand l'interaction Kondo est faible. Nous discutons aussi la question d'une basse dimensionnalité et la relation avec le problème de percolation dans ces systèmes.

Remerciements

Tout d'abord je voudrais remercier le président du jury Daniel Malterre, les rapporteurs Anuradha Jagannathan et Indranil Paul, et les examinateurs Gertrud Zwicknagl et Ilya Sheikin pour avoir accepté de faire partie de mon jury de thèse et pour le temps qu'ils ont consacré à la lecture de ce manuscrit et pour leur participation lors de la soutenance.

Je remercie chaleureusement mes deux directeurs de thèse Claudine Lacroix et Sébastien Burdin. Pendent cette période j'ai eu le plaisir de profiter de leur expérience, leurs compétences scientifiques et humaines et je les remercie pour tout ce que j'ai appris. Je remercie Claudine pour avoir accepté de diriger mon doctorat en France et avoir été disponible pendant ces années. Je remercie Sébastien pour les nombreux échanges, surtout par mail ou par téléphone, pour m'avoir accueilli dans son laboratoire lors mes visites à Bordeaux et pour le temps dédié à mes recherches et à ma thèse.

Je remercie Vladimir Dobrosavljevic, notre collaborateur pour la deuxième partie de cette thèse, pour tous ses conseils et pour les connaissances qu'il m'a fait partager. D'autre part, pour la première partie de cette thèse, j'ai eu le plaisir d'avoir de nombreuses discussions intéressantes avec des expérimentateurs du domaine. Dans ce contexte, je remercie particulièrement Daniel Braithwaite, Daniel Malterre, Thomas Mazet, Olivier Isnard et William Knafo pour les échanges que nous avons eus et qui m'ont permis de mieux connaitre les aspects expérimentaux liés à la mesure de la valence et aux différents composés.

Je remercie l'ensemble des personnels de l'Institut Néel que j'ai côtoyé pendant ces années, les membres de l'équipe Théorie de la Matière Condensée et du département Matière Condensée et Basse Temperature, en particulier le directeur du département Pierre-Etienne Wolff et le responsable de l'équipe Simone Fratini. Un très grand merci à tous les doctorants et postdocs que j'ai pu rencontrer au laboratoire, et plus spécialement à tous ceux avec qui j'ai eu le plaisir de partager le bureau.

Je remercie mes collègues et professeurs de Porto Alegre: Acirete Simões, Roberto Iglesias, Miguel Gusmão, Christopher Thomas et Edgar Santos pour m'avoir encouragé à venir faire ma thèse à Grenoble.

Je remercie Glaucia pour les bons moments que nous avons partagés à Grenoble, ma famille pour son soutien « à longue portée » et mes amis pour leur sympathie.

Enfin, je suis reconnaissant envers le CNPq, qui a financé ma bourse de thèse en France, pour son soutien.

Contents

Chapter 1

Introduction

This thesis has as general topic the description of anomalous lanthanides materials, an important class of strongly correlated systems. In general, strongly correlated materials present partially filled d or f orbitals, which have a small spacial extension compared to s and p orbitals. It leads to interactions among electrons on them that are stronger than the electronic bandwidths. For such reason, the conventional band theory fails in these materials and novel methods have been developed in the last 50 years to deal with them.

In lanthanide systems the relevant orbitals are $4f$ orbitals, which are the most localized among all types of orbitals. Such degree of localization produces extreme phenomena as in heavy fermions, for example[1].

Through the whole work the mathematical formalism of second quantization and Green's functions are employed and the notations are most often the usual ones. For that we refer to textbooks in References [2], [3] and [1]. The physical constants k_B (Boltzmann's constant) and $\hbar$ (reduced Planck's constant) are implicitly taken as one, so energies and temperature are in the same unities.

In this chapter some key concepts on the subject of $4f$-electron systems will be introduced. The basis of such systems is the formation (or not) of stable magnetic moments in lanthanide ions, which can be described theoretically by the impurity Anderson model (Section 1.1.1).

1.1 Magnetic Impurities in metals

Magnetic impurities exist in a metal if the impurity ions have partially filled d or f orbitals. Examples of such behavior are Fe impurities in Cu and Au, in which the impurities contributes to the magnetic susceptibility through a Curie-Weiss term, typical of local moments. In addition, transport measurements showed an electrical resistivity minimum in the same metals. The appearance of these features not only depends on the impurity atom but also on the metallic host.

1.1.1 The impurity Anderson model

The explanation for the local moment formation was put forward by Anderson[4]. He introduced a simple model to explain it, known nowadays as the Single Impurity Anderson model (SIAM):

$$H = \sum_{\mathbf{k},\sigma} \epsilon(\mathbf{k}) c^{\dagger}_{\mathbf{k},\sigma} c_{\mathbf{k},\sigma} + E_f \sum_{\sigma} f^{\dagger}_{\sigma} f_{\sigma} + U f^{\dagger}_{\uparrow} f_{\uparrow} f^{\dagger}_{\downarrow} f_{\downarrow} + \frac{V}{\sqrt{N}} \sum_{\mathbf{k},\sigma} \left(c^{\dagger}_{\mathbf{k},\sigma} f_{\sigma} + h.c. \right) \tag{1.1}$$

The operator $c_{\mathbf{k},\sigma}$ ($c^{\dagger}_{\mathbf{k},\sigma}$) creates(annihilates) one conduction electron in the band with a wave-vector $\mathbf{k}$ and spin orientation σ. Its energy is given by the electronic dispersion $\epsilon(\mathbf{k})$. The impurity site is represented by a non-degenerate local level with energy E_f and its electrons by the operators f_{σ} and $f^{\dagger}_{\sigma}$. The doubly occupied impurity state has an extra energy U (electronic repulsion)., which will be the key ingredient to moment formation. The last term is the hybridization V between the impurity and the conduction band and it can be taken as k-independent in a good approximation.

The impurity site behaves as a local moment as long as it is occupied by one electron only, which will happen if $E_f < \mu$ and $E_f + U > \mu$, being μ the Fermi level of conduction electrons (Figure 1.1) . We adopt the mean-field description of the problem proposed by Anderson [4], employing the Hartree-Fock approximation for the Coulomb repulsion:

$$U f^{\dagger}_{\uparrow} f_{\uparrow} f^{\dagger}_{\downarrow} f_{\downarrow} \rightarrow U \left\langle \hat{n}_{f,\downarrow} \right\rangle \hat{n}_{f,\uparrow} + \left\langle \hat{n}_{f,\uparrow} \right\rangle \hat{n}_{\downarrow} - U \left\langle \hat{n}_{f,\uparrow} \right\rangle \left\langle \hat{n}_{f,\downarrow} \right\rangle , \tag{1.2}$$

The operators $\hat{n}_{f,\sigma} = f^{\dagger}_{\sigma} f_{\sigma}$ are replaced by their averaged values that must be calculated self-consistently.

We summarize the important mean-field results[1]. Within this approximation, the criterion for local moment formation is to have a net magnetization in the impurity $\langle \hat{n}_{f,\uparrow} \rangle \neq \langle \hat{n}_{f,\downarrow} \rangle$, to be determined from the impurity density of states:

$$\rho^{f}_{\sigma}(\omega) = \frac{\Delta/\pi}{(\omega - \varepsilon_{f,\sigma})^2 + \Delta^2} \tag{1.3}$$

The impurity density of states has a lorentzian shape. It is centered in the energy $\varepsilon_{f,\sigma} \equiv E_f + U \langle \hat{n}_{f,\overline{\sigma}} \rangle$ ($\overline{\sigma} = -\sigma$) and it has a width Δ given by:

$$\Delta \equiv \frac{\pi V^2}{N} \sum_{\mathbf{k}} \delta(\omega - \epsilon(\mathbf{k})) = \pi V^2 \rho^{cc}(\omega) \approx \pi V^2 \rho^{cc}(\varepsilon_{f,\sigma}), \tag{1.4}$$

where N is the number of lattice sites. In the last approximation the conduction electrons density of states ρ^{cc} was considered constant in this range of energy.

A solution with $\langle \hat{n}_{f,\uparrow} \rangle \neq \langle \hat{n}_{f,\downarrow} \rangle$ exists as long as the the following condition is obeyed:

$$U \rho^{f}(\mu) > 1, \tag{1.5}$$

[1] Further details are presented in Refs. [4, 1, 3].

This condition is a local version of the *Stoner criterion*, that is used as a criterion for band ferromagnetism in metals[5]. The local moment is stable if the f (or d) density of states is sufficiently large for a given U, that, on its turn, must be finite. An equivalent form of the Stoner criterion is $U/\pi\Delta > 1$, where it becomes evident that the local moment formation is favored if the hybridization V or the conduction electrons density of states close to the impurity level energy is small. That is the reason why moment formation depends on the characteristics of the impurities and the metallic host.

Mixed-valence regime

The local moment formation occurs when the singly occupied level is stable and all the others impurity configurations (empty or the doubly occupied) have energies much higher than the resonant level width Δ. However, if the position of the empty level approaches the Fermi level ($-E_f \to \mu$) and becomes comparable to Δ, the local moment becomes unstable. This situation (Fig. 1.1.b) corresponds to the *mixed-valence regime* of Anderson model, in which the average occupation of the impurity site is less than one. A similar situation arises when the doubly occupied state becomes close to the Fermi level, the impurity average occupation (or valence) being between one and two. Two other non-magnetic regimes of the SIAM arises when the local levels are completely empty or full. The physics of mixed-valence regime will be explored in details in the Part I.

1.1.2 The Kondo model

Taking as granted that the local moment is formed, we can ask now how does it interacts with the conduction electrons and what are the consequences of such interaction. For that purpose, Schrieffer and Wolff performed a canonical transformation of the Anderson model (Eq. 1.1) known as *Schrieffer-Wolff* transformation[6]. It is a projection of the Anderson model into its $n_f = 1$ subspace, so that the other impurity configurations ($n_f = 0$ and $n_f = 2$) are treated as virtual states.

The resulting hamiltonian is known as the Kondo model:

$$H = \sum_{\mathbf{k},\sigma} \epsilon(\mathbf{k}) c^\dagger_{\mathbf{k},\sigma} c_{\mathbf{k},\sigma} + J_K \mathbf{S} \cdot \mathbf{s} \tag{1.6}$$

In this model, the impurity magnetic moment interacts locally with the conduction electron spin through an exchange interaction. The Kondo coupling J_K is related to the parameters of Anderson model by

$$J_K = V^2 \left(\frac{1}{\mu - E_f} + \frac{1}{E_f + U - \mu} \right) \tag{1.7}$$

and it is a positive quantity. Then the Kondo interaction has an antiferromagnetic nature.

The Kondo model was first predicted by Kondo[7] already in 1964, who used it to explain the resistivity minimum observed in normal metals with a very low concentration of magnetic impurities, which was firstly reported in gold samples by de Haas, de Boer and van der Berg[8]

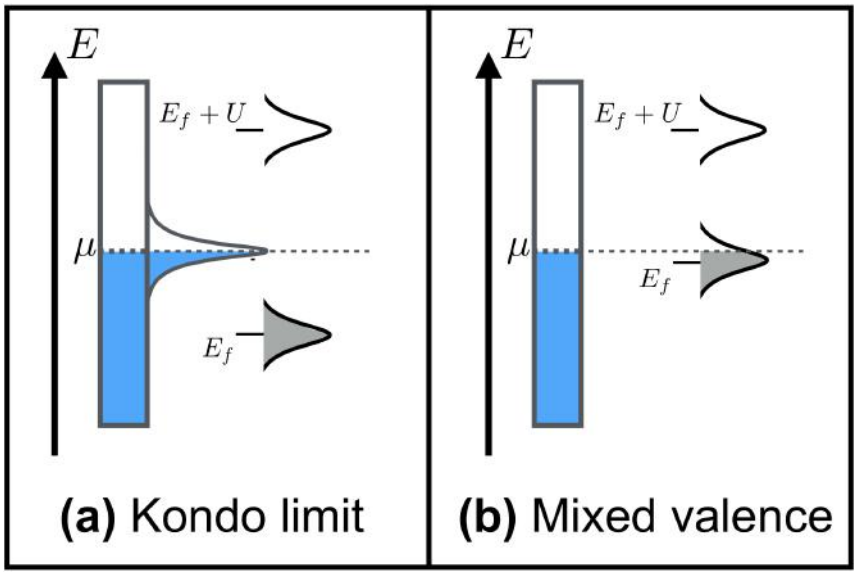

Figure 1.1: Schematic representation of SIAM parameters in **(a)** the Kondo and **(b)** the mixed valence regime. The conduction band is represented by the blue area and it is filled up to the Fermi energy μ. The impurity levels are located at E_f and E_f+U and they are broadened by Δ (Eq. 1.4). In the Kondo limit **(a)**, the impurity level E_f is well below the Fermi energy μ, while the doubly occupied state is above with an energy E_f+U. Virtual processes in which conduction electrons hops on and off the impurity levels generate a peak in the Fermi energy (Abrikosov-Suhl resonance) for $T < T_K$. In the mixed valence regime **(b)**, the level E_f, broadened by the hybridization, approaches μ. The impurity level is partially filled with a non-integer number of electrons. Both situations lead to an enhanced density of states at the Fermi energy, but the underlying mechanism is different.

thirty years before. Kondo used perturbation theory to determine a $\log T$ dependence responsible for the minimum. The perturbation theory remains valid for temperatures above the Kondo temperature,

$$T_K = De^{-1/J_K \rho^c(\mu)}, \tag{1.8}$$

where D is the conduction electrons bandwidth.

The solution of the $T < T_K$ regime required non-perturbative methods inexistent at that time. The key concept that emerges from this problem is the gradual screening of the magnetic impurities with decreasing temperature, which leads to an effective non-magnetic impurity as $T \to 0$. This idea came from the Anderson's "poor man scaling" [9, 1] and it was later formally developed by Wilson in his pioneer work on Numerical Renormalization Group[10].

For $T \ll T_K$ the conduction electrons scattering on the impurity progressively screens its magnetic moment. The many-body process creates a sharp peak in the density of states located at the Fermi energy, known as Abrikosov-Suhl (or Kondo resonance). The width of the Kondo resonance is proportional to T_K, which leads to enhanced contribution on the magnetic susceptibility and specific heat at low temperatures. The physical picture of the Kondo regime for $T < T_K$ is presented in Figure 1.1, including the Kondo resonance. We stress that this

situation is different from the mixed-valent regime shown in the right, which is discussed in details in Section 2.3.1.

1.2 Lattice models

In the last section it was discussed the consequences of having isolated magnetic impurities in non-magnetic metals. In systems with a periodical lattice of magnetic ions, it is necessary to generalize the above picture.

The simplest model to describe metals containing both itinerant and localized electrons is the Periodic Anderson model (PAM):

$$H = \sum_{\mathbf{k},\sigma} \epsilon(\mathbf{k}) c^\dagger_{\mathbf{k},\sigma} c_{\mathbf{k},\sigma} + E_f \sum_{i,\sigma} f^\dagger_{i\sigma} f_{i\sigma} + U \sum_i f^\dagger_{i\uparrow} f_{i\uparrow} f^\dagger_{i\downarrow} f_{i\downarrow} + V \sum_{i,\sigma} \left(c^\dagger_{i\sigma} f_\sigma + h.c. \right) \quad (1.9)$$

This is a generalization of the Anderson Impurity model (Eq. 1.1) in which every lattice site contains a non-degenerate local level with energy E_f. The local nature of these levels implies that the Coulomb repulsion U between two f-electrons on the same site is large.

The Periodic Anderson model possesses several regime of parameters. The two most relevant are the mixed valence and the local moment (or Kondo) regimes, which are characterized by the same parameters than in the SIAM. Nevertheless, the nature of both regimes is different in the lattice: in the mixed valence regime of PAM, the system Fermi energy depends on the f-levels occupation given that the total number of electrons $(c+f)$ is conserved (see Section 2.3.1). In the Kondo limit the difference lies in the fact that the impurity scattering becomes coherent due to the periodicity of local moments, giving a coherent state at low temperatures (Section 6.1).

In the Kondo limit the local levels are occupied with one electron and charge fluctuations are frozen, but virtual processes involving the empty and the doubly occupied level generate spin fluctuations. In this case a generalized version of Schireffer-Wolff transformation can be applied to the PAM in order to establish the effective hamiltonian from a projection into the $n_f = 1$ subspace. As far as the terms in V^2 are concerned, the effective hamiltonian is a lattice version of the Kondo model, called Kondo Lattice model (KLM):

$$H = \sum_{\mathbf{k},\sigma} \epsilon(\mathbf{k}) c^\dagger_{\mathbf{k},\sigma} c_{\mathbf{k},\sigma} + J_K \sum_i \mathbf{S}_i \cdot \mathbf{s}_i \quad (1.10)$$

In this model there is one local moment in each lattice site interacting locally with conduction electrons via an antiferromagnetic exchange J_K. The Kondo interaction favors again the formation of a non-magnetic singlet state between local moments and conduction electrons, however it is in competition with an additional indirect exchange interaction among local moments. This interaction, known as RKKY interaction, is mediated by conduction electrons or, more precisely, by the oscillations in the electronic spin density induced by local moments (the Friedel oscillations). The RKKY interactions can be written as:

$$H_{RKKY} = \sum_{ij} J(r_{ij}) \mathbf{S}_i \cdot \mathbf{S}_j \quad (1.11)$$

where the magnetic coupling $J(r_{ij})$ at large distance r_{ij} is proportional to

$$J(r_{ij}) \sim J_K^2 \rho(\mu) \frac{\cos(2k_F r_{ij})}{(k_F r_{ij})^3}. \tag{1.12}$$

Here r_{ij} is the distance between the moments $\mathbf{S}_i$ and $\mathbf{S}_j$ and k_F is the Fermi wave-vector of conduction electrons (the interaction strength decays with the distance r_{ij} and its sign depends on $2k_F r_{ij}$). The RKKY interaction alone can lead to ferro-, antiferro- or helimagnetism. In heavy fermions the magnetic order is often antiferromagnetic, for example, in $\mathrm{CeAl_2}$ [11].

The Doniach's diagram

The competition of the Kondo effect and magnetic order has been considered first by Doniach[12], who proposed a phase diagram known now as Doniach diagram (Figure 1.2)[13, 14]. It a comparison between the energy scales of the two phases: the Kondo temperature $T_K \sim \exp(-1/J_K \rho^c(\mu))$ and the magnetic ordering temperature $T_N \sim J_K^2 \rho^c(\mu)$. For a particular system, if the parameter $J\rho^c(\mu)$ is such that $T_K > T_N$ (i.e. if $J_K \rho^c(\mu)$ is small enough), the local magnetic moments will be quenched and the system ground state is non-magnetic. On the other hand, for $T_N > T_K$, i.e. for large $J_K \rho^c(\mu)$, the magnetic order is stable at low temperatures.

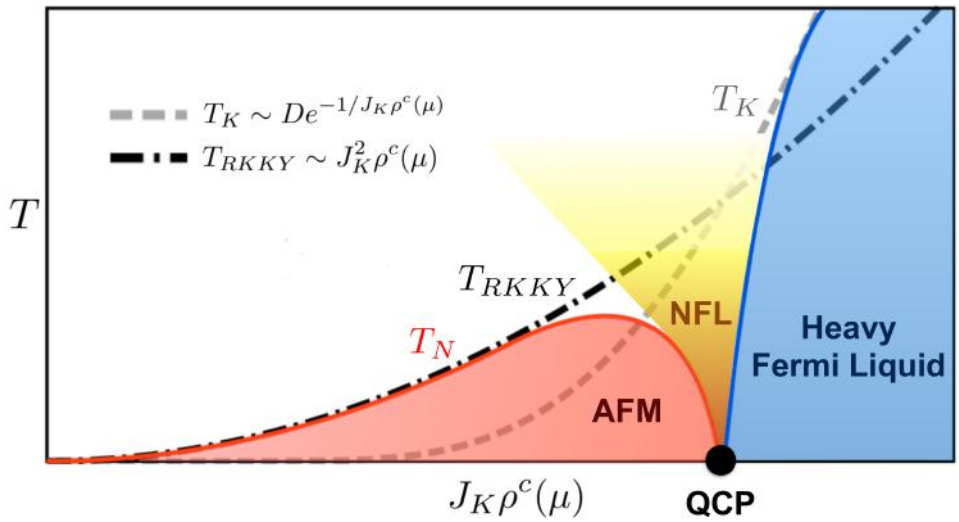

Figure 1.2: Doniach diagram for the Kondo Lattice, illustrating the competition between antiferromagnetism(AFM) and the heavy fermion regime. These phases are separated by a Quantum Critical Point (QCP) at zero temperature. Non-Fermi Liquid (NFL) behavior appears in the vicinity of the QCP.

By tuning the parameter $J\rho^c(\mu)$, which can be done experimentally with pressure or doping, the system can pass from one ground-state to the other. The two phases are separated at zero temperature by a quantum critical point(QCP), i.e. a second-order phase transition,

where quantum fluctuations are large[14, 15, 16]. The QCP is often "hidden" by a superconducting dome as in $CeCu_2Si_2$[17] and close to this QCP can be observed a Non-Fermi Liquid behavior(NFL)[18, 19].

Heavy-fermions

Let us discuss in more details the non-magnetic ground-state of the Kondo Lattice. It is a Fermi Liquid phase characterized by an extremely large effective mass of charge carriers. Systems in this phase are called *heavy electrons systems*[14, 20]. One example is $CeAl_3$, which has a Sommerfeld coefficient $\gamma = 1620 mJ/mol.K^2$ [21], which corresponds to an electronic effective mass three orders of magnitude larger than the electron mass. The key concept to understand this behavior is the *coherent* nature of Kondo effect in the lattice. The coherence is achieved by the periodic electronic scattering on the Kondo singlets, which generates quasiparticles with a very narrow bandwidth. It is in contrast with the incoherent scattering in the single impurity scenario that leads to a large resistivity at low temperatures[14]. The "heavy" nature of quasiparticles can be interpreted as a partial delocalization of f-electrons due to the hybridization to conduction electrons via Kondo effect. In Chapter 6.1 we will cover these aspects in more details.

1.3 Thesis presentation

In this thesis we are interested in two different aspects of the physics described in this introduction. Part I covers the study of valence transitions in lanthanide intermetallics, focusing on the valence dependence on pressure, doping, external magnetic fields and ferromagnetism. In Part II the topic is the study of magnetic-nonmagnetic substitutions in Kondo alloys and the effect of disorder in such systems. Both parts present theoretical studies on these subjects using methods appropriated for each case.

A common interest of both subjects is to provide a different perspective on the physics of $4f$ electron systems, departing from the Doniach's conjecture on Kondo Lattices. Although extensively used to understand the behavior of concentrated lanthanide systems, the Doniach diagram has strong limitations, since it is valid only in the Kondo Lattice limit.

Part I

Model for valence transitions in lanthanide systems

Chapter 2

Generalities on valence transitions in lanthanides

In the first part of this thesis we will discuss the problem of valence transitions in some intermetallic lanthanide compounds from a theoretical perspective. The objective is to understand the different effects that play a role in such transitions and compare the results with the interplay of lanthanide valence, pressure, temperature, applied magnetic field and ferromagnetism present in real systems.

In the following three introductory sections some general aspects on the valence transition problem will be presented, starting from an overview of the intermediate valence states in rare-earth systems. Then we will show the characterization of intermediate valence states by experimental measurements, including both static and dynamic probes of valence states. In the third introductory section some models for the description of valence transitions and intermediate valence states will be introduced, having in mind their pertinence with respect to the model that will be used in this work.

2.1 Introduction

2.1.1 Valence of lanthanide ions

Before entering in the physics of intermetallic lanthanides and their valence states, let me briefly discuss some chemical and physical properties of lanthanides in their atomic and ionic form[1]. In the lanthanide series $4f$ orbitals are very localized penetrating the xenon-like core considerably, and do not overlap with outer orbitals (like 5s and 5p). Therefore they almost do not participate in chemical bonding and they are weakly affected by different environments.

Most lanthanides have atomic configuration $[\mathrm{Xe}]4\mathrm{f}^{\mathrm{n}}6\mathrm{s}^2$. Exceptions include lanthanum, cerium, gadolinium and lutetium, having $[\mathrm{Xe}]4\mathrm{f}^{\mathrm{n}}5\mathrm{d}^1 6\mathrm{s}^2$ configuration. When forming ions, all lanthanides loose their $6s$ electrons easily and the first and second ionization energies are

[1] For a complete discussion check Reference [22]

almost constant in the whole series. In most cases a third electron is also lost and a trivalent configuration is stable, corresponding (without any exception) to electronic configurations [Xe]$4f^n$ from the lanthanum ($n = 0$) until the lutetium ($n = 14$). All lanthanides can be trivalent, but divalent and tetravalent configurations are possible if the extra stability from empty, half-filled and complete 4f subshell is achieved.

The inefficient shielding of the nuclear potential by 4f electrons increases the attraction of 5s and 5d electrons, reducing the ionic radius when the atomic number increases. Therefore lanthanides in their metallic form have a decreasing metallic radius (and primitive cell volume) as it goes to higher atomic numbers, leading to the so called lanthanide contraction shown in Figure 2.1. The metallic radius follows the ionic radius except for ytterbium and europium, that have metallic radius at least 20pm larger than the regular pattern. They have the valence state $2+$ stable due to the extra stability of half and completely filled shells and the additional 4f electron reduces the atomic core potential by shielding, increasing the atomic size. As we will see later in this work, the energetic proximity of $2+$ and $3+$ oxidation states in Eu and Yb leads to large valence variations in Eu and Yb intermetallic compounds.

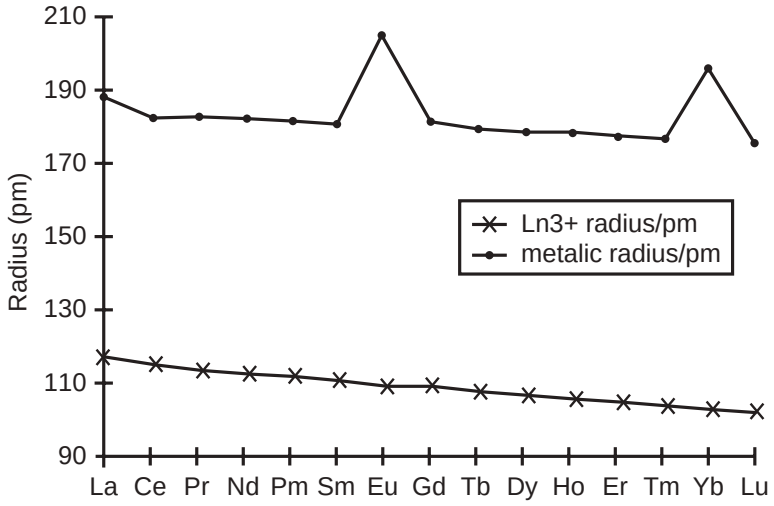

Figure 2.1: Measurements of ionic (trivalent state) and metallic radius for the lanthanide series extracted from Reference [22]. The slow decrease of the radius along the series evidences the lanthanide contraction: the nuclear potential screening by 4f electrons is less effective and the outer orbitals contract when the atomic number increases. The pronounced anomaly in the metallic radius of Eu and Yb comes from their tendency towards divalent valence states, as explained in the text.

Table 2.1 shows some properties of different valence states for *anomalous* lanthanides ions. They are referred as anomalous because quite often the trivalent state is not stable with respect to divalent or tetravalent states. It is remarkable that such behavior shows up only in atoms in the beginning (Ce), the middle (Sm and Eu) and the end (Tm and Yb) of the series. It reflects the aforementioned energetic advantage in having empty, half-filled or filled shells.

Table 2.1 reveals another feature of the valence transitions: the competition between *mag-*

Rare-earth ion	valence (f^n)	S	L	J	$g_{\text{Landé}}$	μ (μ_B)
Ce	$4+$ (f^0)	0	0	0	0	0
	$3+$ (f^1)	1/2	3	5/2	6/7	2.54
Sm	$2+$ (f^6)	3	3	0	0	0
	$3+$ (f^5)	5/2	5	5/2	2/7	0.84
Eu	$3+$ (f^6)	3	3	0	0	0
	$2+$ (f^7)	7/2	0	7/2	2	7.94
Yb	$2+$ (f^{14})	0	0	0	0	0
	$3+$ (f^{13})	1/2	3	7/2	8/7	4.54

Table 2.1: Valence states, multiplet quantum numbers, magnetic Landé factor g_L and Bohr's magnetic moment μ_B for four anomalous lanthanide ions. Adapted from Reference [23].

netic and *non-magnetic* valence states. The total angular momentum and effective magnetic moment of such configurations are quite large as a consequence of the Hund's rules. For instance, the europium undergoes to a transition between a trivalent state with $J = 0$, by the cancellation of spin and orbital angular moment, to a fully spin-polarized divalent state with magnetic moment close to $8\mu_B$. Therefore magnetic and valence transitions are strongly coupled.

2.1.2 Two historical examples

The archetypal example of lanthanide system exhibiting a valence transition is the metallic cerium. Its pressure-temperature phase diagram is quite rich [24], possessing among many solid phases, two distinct fcc phases γ and α with two different lattice parameters (Fig. 2.2). By applying pressure in this region of the phase diagram, the system undergoes to an isostructural transition from the low-pressure γ phase to the high-pressure α phase. At room temperature the γ-α transition occurs around 0.7GPa, where the lattice constant changes abruptly from 5.16Å(γ) to 4.85Å(α)[25].

The first order transition line that separates both phases ends in a critical point located at $T_c \approx 600K$ and $p_c \approx 1.7 - 2\text{GPa}$. The origin of such volume collapse ($\sim 15\%$) lies in a discontinuous valence changing of the Ce ions from 3.67 to 3.06[26, 27], for the α and γ phases, respectively. The increase of cerium valence leads to a larger primitive cell's volume because the screening of the nuclear potential is reduced by the decrease of electronic occupation of the f orbitals. The same valence transition can be estimated by magnetic susceptibility data[28, 26]. The magnetic moments found are $1.14\mu_B$ and $2.49\mu_B$ for the α and γ phases, respectively, which provides estimated valence values of 3.55 and 3.06 when compared to $2.54\mu_B$ of the free Ce^{3+} ion (see Table 2.1).

The second historical example of valence transition is the samarium calchogenide SmS. This material undergoes to a similar isostructural transition (simple cubic) under pressure associated to a change of the Sm valence. Its low-pressure phase at $300K$ is black, semiconducting and the samarium ions are divalent. At $p = 0.6GPa$ a semiconductor-metal transition takes place, visually marked by the golden color of the system in the metallic phase. The gold phase

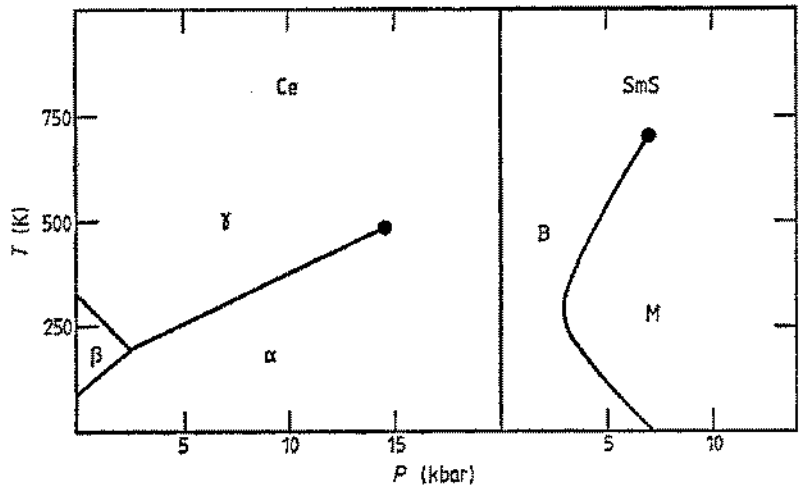

Figure 2.2: Phase diagram for metallic Ce (left) and SmS (right) extracted from Reference [23].

(M-SmS) has an intermediate valence $Sm^{2.75+}$ determined by lattice measurements.

Metallic Ce, SmS and other mixed valence have been studied intensively between the decades of 1970 and 1980. For further details on these experiments and on the different aspects of the problem covered in this chapter the reviews of Varma[29], Khomskii[30] and Lawrence *et al.*[23] are suggested.

2.1.3 General aspects of intermediate valence states

First of all, an important distinction should be made between *homogeneous* and *inhomogeneous* mixed-valence states[2]. In both cases the lanthanide average valence is different from a integer value, but locally the valence behavior is completely different. In an inhomogeneous mixed-valence state each ion in the lattice is in a well defined (integer) valence state and ions with different valences occupy inequivalent positions, generating a charge ordered state. Two examples of rare-earth materials with charge ordered states are $\mathrm{Eu_3S_4}$ and $\mathrm{Sm_3S_4}$[31].

In homogeneous mixed-valence systems all the ions occupy equivalent lattice sites, the average valence in each ion is the same and it is not an integer value. The valence state is in a quantum mechanical state described by a linear combination of two different valence states:

$$|\psi\rangle = a\,|f^n\rangle + b\,\left|f^{n+1}\right\rangle, \tag{2.1}$$

Other states are excluded in the combination due to the large Coulomb repulsion inside f orbitals.

The condition to have an intermediate valence state is that both atomic levels E_n and E_{n+1} are close to each other and both close to the Fermi energy. In reality, since the f levels weakly hybridize with the other electronic states (spd bands), there is a finite width Δ (Eq.

[2]The nomenclature employed here follow the same lines present in Varma's review on mixed valence[29].

1.4) for these states. So it is required that $|E_n - E_{n+1}| < \Delta$ in order that the mixed valence state exists.

It is important from the beginning to differentiate the mixed-valence state from the Kondo state formed in magnetic impurities (see Figure 1.1). Contrary to the Kondo state, the formation of the local moment in the mixed valence state is forbidden by the very large charge fluctuations in the f level. The valence is related to the coefficients in a wave-function as in Eq. 2.1 and its value ranges between two integers. Since one can go continuously from the Kondo to the mixed valence case , it is very hard (if not impossible) to characterize a system as "purely" Kondo or mixed-valence. An attempt to separate the two physical scenarios is the analysis of valence transitions. Given that the Kondo regime requires a nearly integer valence state, while in a mixed-valent state it is not necessary, one could naively state that every transition in which the valence variation is small, the dominant effect for valence changing is Kondo effect. However, if the valence variation is large, it is connected to the competition of two different atomic ground states for f electrons (mixed-valence). Unfortunately the physical situation is much more complex than that and such classification can not be taken as granted.

2.2 Experimental techniques to measure valence

In Section 2.1 we reviewed some general aspects of valence fluctuation and chemical properties of lanthanide ions and monoatomic metallic systems. In this section we discuss some relevant experimental features observed in lanthanide systems with valence fluctuations that motivate our theoretical work.

The purpose of this chapter is to give a brief introduction to experimental techniques from a theorist point of view, which is far from being complete and rigorous. In Section 4.3 we present another experimental discussion, focused on specific systems, where we may recall some points discussed below.

2.2.1 Time-scales of valence fluctuation

If the valence state of a given ion in the metallic environment is a linear superposition of two nearly degenerate valence configurations, it means that it is possible to associate a time-scale to the fluctuation between these configurations. As we saw in Section 1.1.1, the charge fluctuation of a f level has a characteristic energy Δ (Eq. 1.4), the f-level width, and it is inversely proportional to the characteristic time of fluctuations.

Let us suppose, for the sake of the argument, that $\Delta \sim 1meV$ for two nearly degenerate valence states in a rare-earth atom. Then a good estimative for the characteristic time of valence fluctuations is given by

$$\tau_{vf} \sim \frac{h}{\Delta} \sim 10^{-12} s, \tag{2.2}$$

where $h = 4.135 \times 10^{-15} eV \cdot s$ is the Planck constant.

The characteristic time of valence fluctuations is an important issue regarding the experimental observation of this phenomenon. If the experiment probes the system in a time larger

than τ_{vf}, then the observed valence is *an average* of two valence configurations. On the other hand, if the experiment operates in a time-scale *smaller than* τ_{vf}, one can resolve both valence states independently. Hence there are two possible types of measurements for the valence: *slow* and *fast* measurements.

The experimental time-scale τ_{ext} depends on many factors, which include the energy of the probe (for example, photons or neutrons) and the underlying physical mechanisms occurring in the system during and after the interaction with the probe. Since in many cases the estimate τ_{ext} is rather imprecise or dubious and a deeper discussion on the experimental techniques is out of the scope of the present work, we restrict ourselves to the division between static and dynamic measurements.

2.2.2 Static measurements

Structural analysis by X-ray diffraction

As we saw in Section 2.1.1, there is a direct relation between the metallic radius and the valence state. If one can synthesize a family of compounds with different rare-earth ions, for example ReO (being Re a lanthanide) or a metallic Re, it would be possible to compare the lattice parameters (measured, for instance, from X-ray diffraction) and extrapolate the average valence. One example of this comparative analysis was employed to explain the anomalous behavior of Eu and Yb seen in Figure 2.1. In another type of experiment one could measure the variation of unit-cell parameters for the same compound in different external conditions (temperature, external pressure and others). For instance, the well-known α-γ transition of metallic cerium, in which a substantial volume variation is detected.

The basic hypothesis employed in lattice measurements is that any volume change is mainly an effect of a valence variation, but other mechanisms can modify the lattice parameters. For instance, in real materials the application of pressure (or doping) can modify the band structure even if the valence keeps constant.

Lattice constant measurements is a comparative method which requires an initial knowledge (or guess) for the valence in a given compound or under certain conditions, which is another important limitation. Nevertheless, this method is useful to predict phase transitions and anomalous valence states and it has its historical importance in the field that makes it worth to mention.

Magnetic measurements

Other possible experiments that reveal intermediate valence states are the magnetic susceptibility measurements. In an homogeneous mixed valence state containing one magnetic and one nonmagnetic configuration as present in Equation 2.1, it is expected that fluctuations would prevent magnetic ordering at low temperatures. For example, SmS in its intermediate valence phase (metallic) is non-magnetic at very low temperatures [32, 33].

The temperature behavior of magnetic susceptibility in a true mixed valent state is the following: at high temperatures, the susceptibility follows a Curie's law $\chi(T) = C/T$, where C is proportional to the average between the magnetic moments in the two valence states weighted

by the contribution of each one in the valence. This behavior is also seen in inhomogeneous mixed-valence states, so both types of intermediate valence can not be distinguished from the magnetic susceptibility in this range of temperatures.

Homogeneous mixed-valence states generally do not order at low temperature. One exception is thulium, since the two relevant valence states are magnetic. The magnetic order is inhibited by the strong local charge fluctuations. When the system approaches the zero temperature the magnetic susceptibility reaches a constant value.

A phenomenological expression for the magnetic susceptibility of intermediate valence systems was given by Sales and Wohleben[34]:

$$\chi(T) = \frac{\mu_n^2 v(T) + \mu_{n-1}^2 (1 - v(T))}{T + T_{vf}} \tag{2.3}$$

Here μ_n and μ_{n-1} are the magnetic moments for the $4f^n$ and $4f^{n-1}$ states, respectively. $v(T)$ represents the average valence of the rare-earth ion that, in principle, depends on the temperature. This formula has a Curie-Weiss behavior in which the characteristic energy scale of valence fluctuation T_{vf} (proportional to the width of the virtual level Δ) acts as a Curie temperature. Note that at zero temperature it predicts $\chi(0) = \mu^2 v(0)/T_{sf}$ if there is only one magnetic valence state (with moment μ) in the mixture.

2.2.3 Dynamical measurements

Mössbauer spectroscopy

Mössbauer spectroscopy[31] probes the shifts in nuclear transition energies due to different environments for the atomic nucleus, through the atomic absorption and emission of energetic gamma rays. One part of this effect comes from the difference of s electron densities that, in the context of interest here, can be attributed to the addition or removal of 4f electrons. With less electrons in the 4f orbitals there is less nuclear screening and, consequently, the 5s electronic shell comes closer to the nuclear core. This is called *isomer shift* [3].

There are at least two important features in Mössbauer spectra in the context of valence determination. The average line shift is a measure of the average f orbitals occupation, while the linewidth is related to its fluctuations. Since it probes several ions in the crystal, this technique is capable of differentiate the inhomogeneous from the homogeneous intermediate valence states. In the former case it is seen as the apparition of two separated spectral lines corresponding to two valence states. Contrastingly, the homogeneous case gives a single spectral line positioned between those of well defined valence states are expected (Figure 2.3).

The isomer shift measurement is considered a slow technique since it does not separate the two states that compose the mixed-valence. Estimation of characteristic time provided by Coey and Massenet [31] is on the order of $10^{-9}s$, which is well above the estimated $\tau_{vf} \sim 10^{-12}s$.

In addition to the fact that the Mössbauer technique is suitable enough to rule out the existence of inhomogeneous mixed-valence states, it has a good experimental resolution even

[3] It is also named chemical shift, since it is sensitive to different covalent bondings (formed from s electrons).

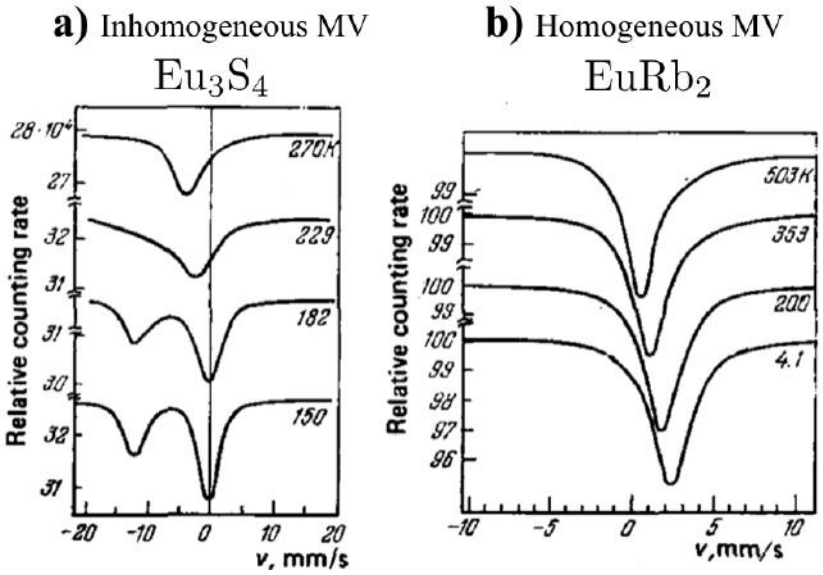

Figure 2.3: Mössbauer spectra for Eu on the inhomogeneous mixed-valent $\mathrm{Eu_3S_4}$ (left) [31] and the homogeneous $\mathrm{EuRb_2}$ (right) [35] as a function of the temperature. In the inhomogeneous case two peaks appear in the spectrum at low temperatures, corresponding to two different valence states of europium in inequivalent lattice sites. For an homogeneous mixed-valence state only one peak is seen and its position varies with the temperature, signaling a variation in the average valence. Figure extracted from Reference [30].

in early measurements. One of the issues is again the necessity to compare the isomer shift for a given system with a similar one, which is very bad to extract quantitative results. Finally, this technique can only be applied to Mössbauer active elements, that includes all the lanthanide elements with the important exception of cerium.

Neutron scattering

Techniques involving neutrons are very useful to determine the existence and the properties of magnetic ordering in solids and the characteristics of many types of excitations. There are two types of neutron scattering measurements: neutron diffraction and inelastic neutron scattering. Neutron diffraction allows, among other things, to determine magnetic peaks associated to magnetic order and the magnetic moment values. This technique is, in most cases, not particularly relevant for intermediate valence compounds, since very often these systems are in non-magnetic ground states dominated by strong charge fluctuations.

Contrary to the former example, the inelastic (and quasielastic[4]) neutron scattering reveals important aspects of the intermediate valence regime[23, 36]. The mixed-valence state manifests itself through a temperature-independent large linewidth of the quasielastic peak that is claimed [36] to be proportional to Δ (Eq. 1.4). For instance, the values of Δ obtained

[4]Even that the two techniques are different from the experimental point of view, the physical interpretation can be thought as the same in a superficial consideration.

from the spectra of $YbCu_2Si_2$ and $CePd_3$ are $\sim 30meV$ and $\sim 40meV$, respectively. These linewidths are two orders of magnitude larger than those of a rare-earth material in a stable valence configuration[36].

Inelastic neutron scattering can also determine whether the spin dynamics is related to the charge fluctuations or the Kondo effect. While in the former case the linewidth does not depend on the temperature, in the latter it increases considerably with T. This behavior is seen in both Kondo lattice ($CeCu_2Si_2$ and $CeAl_3$) and Kondo impurity (Fe in Cu) systems[36].

Resonant Inelastic X-Ray Scattering

Among all the techniques to measure the valence of materials, the most accurate is the resonant inelastic X-ray scattering[37]. It is a spectroscopic technique in which a very energetic photon interacts with electrons in deep-lying electronic levels, promoting them to empty states that later decay, emitting another photon with different momentum and energy. Through the analysis of the energy, momentum and polarization of the scattered photon it is possible to determine the properties of excitations in the system.In order to enhance the scattering cross section, it is crucial to choose the photon energy to be in one of the atomic X-ray transitions of the system (the resonant character). RIXS is element dependent, since one can select each atom on the material through the photon energy. Also it is orbital dependent from the selection rules involving the photon's emission and absorption.

The accuracy on the valence measurements by RIXS technique comes from the fact that one can identify each valence state by a peak in the spectrum. Both peaks are fitted by gaussian functions and their integrated weights are compared in order to extract the average valence. For instance, if two valence states $4f^n$ and $4f^{n+1}$ forms an intermediate valence state, then the valence extracted from RIXS experiment is ($I(n)$ is the integrated weight of the peak associated to the $4f^n$ state):

$$v = n + \frac{I(n+1)}{I(n) + I(n+1)} \tag{2.4}$$

Let us see in more detail the resonant X-ray technique for the case of ytterbium. In Figure 2.4 (right) the processes occurring in the Yb atom are schematically depicted. The initial state is an intermediate valence state between $4f^n$ and $4f^{n+1}$ (v are the other valence electrons coming from spd orbitals). A highly energetic photon is absorbed by the atom and a $2p$ core electron is excited above the Fermi level, generating the excited state. The energy of such state depends on the number of $4f$ electrons through their interaction with the $2p$ core-hole state. Then a second core electron, here from $3d$ orbital, fills the core-hole and excited state decays by the emission of a photon. The energy of the final states also depend on the amount of f electrons, so the initially mixed state is separated in two. This separation is seen in the spectra on Figure 2.4(left).

RIXS is the most precise spectroscopic technique for valence transition, nevertheless there are other examples. The pioneer example in this context is X-Ray Photoemission Spectroscopy (XPS)[39]. Photoemisson consists in sending a high energetic photon to the material and measure the energy of the electron taken from the interaction with the absorbed photon. From

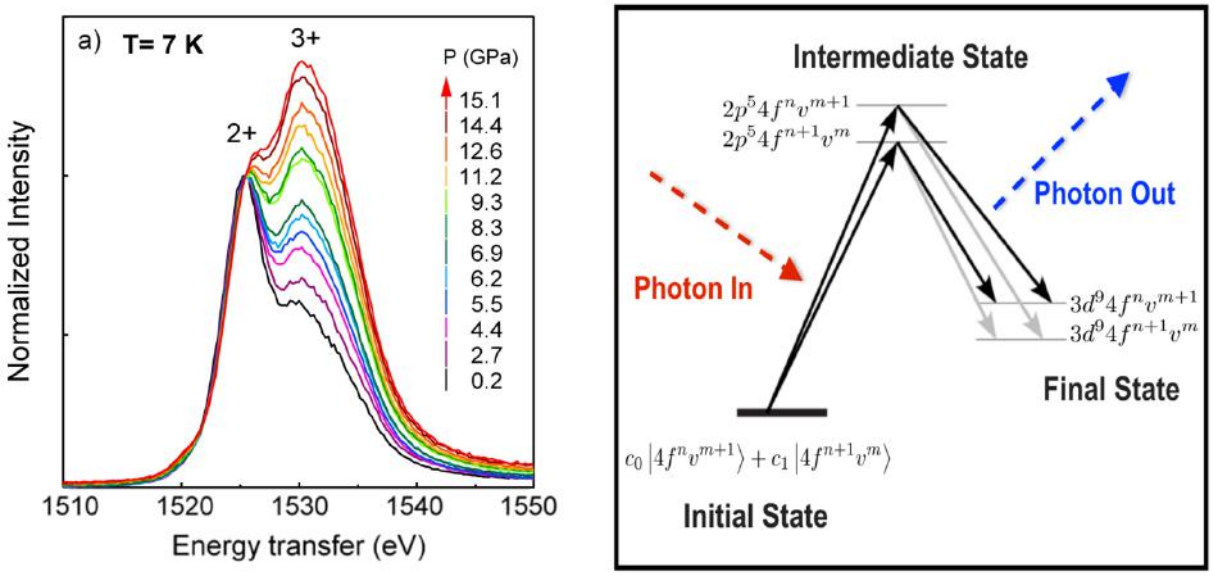

Figure 2.4: **Left:** An example of resonant inelastic X-ray spectrum: $\mathrm{YbCu_2Si_2}$ under pressure. Two peaks can be identified for each valence state and the proportion between their integrated weight determines the average valence state. Figure extracted from Ref. [38]. **Right:** Schematic representation of the RIXS, illustrating the splitting of the superposing state $c_0 |4f^n v^{m+1}\rangle + c_1 |4f^{n+1} v^m\rangle$ by the absorption and emission of photons. Extracted from Ref. [37].

the XPS spectrum one can identify peaks associated to the transition $4f^n \to 4f^{n-1}$, so it is possible to determine the difference in energy of two valence configurations.

Regarding the experimental time-scale, the above mentioned techniques (RIXS and XPS) are considered as fast probes because they can resolve two different valence states. In spectroscopy it is inferred by the energy of the incident photon and for X-Rays it is greater than $100eV$, giving $\tau \lesssim 10^{-16}s$. This value is well below the estimation provided in Eq. 2.2.

Summary

In this section we have mentioned some experimental techniques that provides some informations on the valence states of rare-earth atoms in crystals. The valence observations depend on the relation between the experimental time-scale τ_{exp} compared to the typical time of local charge fluctuations on the 4f levels τ_{vf}. Two valence states are observed separately only if $\tau_{exp} < \tau_{vf}$, since the experimental setup has sufficient "resolution" to do it. Otherwise, if $\tau_{exp} > \tau_{vf}$, an average behavior between these two states is observed. While the latter situation is exemplified by bulk techniques as lattice constants or magnetic susceptibility measurements, the former contains spectroscopic techniques as photoemission and X-ray scattering measurements.

2.3 Models for valence transitions

Having reviewed in Section some experimental manifestations of the intermediate valence states of rare-earth ions, we put in perspective the theoretical models proposed to describe the valence properties. Since the literature on the subject is vast, we limit ourselves to the presentation of models that we consider the most pertinent.

In the first subsection the mixed valence regime on the single impurity (SIAM) and periodic Anderson(PAM) models is discussed. While the PAM describes well the crossover from the Kondo to the intermediate valence regimes and continuous valence transitions, it fails in provide a mechanism to the discontinuities observed in many materials. For that purpose, we discuss in the last two subsections the Falicov-Kimball model, which is historically the first model that describes the discontinuous valence transitions, and models containing explicit volume effects (Kondo Volume Collapse), which are a second route to understand the pressure dependence in valence for some compounds.

2.3.1 Anderson impurity and lattice models

The single impurity Anderson model (Eq. 1.1) has an intermediate valence regime depending on its parameters, as it was discussed in Section 1.1.1. The rough criterion for intermediate valence in SIAM depends on the position of the impurity levels (E_f and E_f+U) with respect to the Fermi level μ and their width Δ (defined in Eq.1.4) due to the hybridization with the conduction electrons. If $|E_f-\mu|<\Delta$ or if $|E_f+U-\mu|<\Delta$, then the broaded level "cuts" the Fermi energy and the electronic occupation on the impurity level is non-integer[5]. The situation corresponding to the condition $|E_f-\mu|<\Delta$ was depicted in Fig. 1.1.b and the impurity has $n_f<1$ electrons.

The intermediate valence case corresponds to the asymmetric regime of Anderson model ($U\gg|E_f|,\Delta$) and it was studied by Haldane using scaling theory[40]. He had shown that the criterium for a mixed-valence regime in this model is $|E_f^*|\lesssim\Delta$, where

$$E_f^* = E_f + \frac{\Delta}{\pi}\ln\left(\frac{D}{\Delta}\right)$$

is the scaling-invariant "effective position" of the local level E_f. In this regime the charge fluctuations do not disappear by the scaling procedure and the occupation on the impurity site n_f is not integer at $T=0$.

The situation above should be contrasted to $-E_f^*\gg\Delta$, in which the charge fluctuations are frozen for $\widetilde{T}\gg\Delta$ and a local moment is stable. In this case the system is in the Kondo limit, where the Kondo model is valid. The passage from the two situations described here is continuous and the physical quantities, such as the occupation n_f, susceptibility and specific heat, are smooth universal functions of E_f^*/Δ. As a consequence, it is hard to separate both regimes from the experimental point of view. Besides, the SIAM is unable to describe coherent

[5] Given the large value of U in f orbitals, the second condition is not expected in real systems

effects from the dense regime, which play a very important role at low temperatures. For that reason it is appropriate to discuss the lattice model.

Regarding the local charge fluctuations on the f level, the condition to obtain a mixed-valence state in the Periodic Anderson Model (Eq. 1.9) is the same as in single impurity model, i.e. $|E_f - \mu| < \Delta$. The difference comes from the fact that the Fermi energy μ is fixed. In the SIAM, μ does not depend on the impurity occupation and it is determine purely by the conduction electrons concentration n_c. In the PAM, the Fermi level depends on the local levels occupation, since the total number of electrons is conserved, independently if they are in local levels or in the band.

In the intermediate valence state of PAM the Fermi energy is *pinned* in the 4f level peak (located in E_f). Any large change in the valence leads to a feedback in the chemical potential[1], restoring the valence value. It occurs because the conduction electron density of states is much smaller than the contribution from the f electrons, so it is difficult to accommodate the electrons leaving the f orbitals in the band. As a consequence, the valence variation described by the PAM is always small if other effects are not taken into account.

From the experimental point of view two situations may arise: the valence variation can be continuous or not. The discontinuity can accentuate the passage from the Kondo to the intermediate valence regime if one of the valence configurations is close to the magnetic one, as in the α phase of metallic Ce. For continuous variations the passage is not marked, however one estimative can be done through the Sommerfeld coefficient γ of specific heat, that is expected to be one order of magnitude higher in the Kondo regime (since it is a heavy fermion) than in the intermediate valence. The coefficient γ in the mixed valence regime is larger than those in ordinary metals, since the density of states at the Fermi energy is enhanced by its proximity to the f level.

The major drawback in the PAM is the absence of mechanisms allowing large valence changes, which is in contrast to the experimental examples presented in Section 2.1.2. For that reason, we present in the next subsection the Falicov-Kimball model, which describes continuous and discontinuous valence variations. Lastly, the Kondo Volume Collapse model and its description of volume instabilities in metallic Ce are discussed.

2.3.2 The Falicov-Kimball model

The first model used to describe the behavior of valence transitions in rare-earth materials was proposed by L. Falicov and J. Kimball in 1969 [41]. Their purpose was to study the semiconductor-metal transition of some transition-metal oxides and $\mathrm{SmB_6}$ [6] by the analysis of different intra-atomic interactions involving Bloch (conduction electrons) and Wannier states from 4f orbitals (or 3d for the transition metals). The hamiltonian is written as:

$$\mathcal{H}_{FK} = \sum_{\mathbf{k}\sigma} \varepsilon(\mathbf{k}) c^{\dagger}_{\mathbf{k}\sigma} c_{\mathbf{k}\sigma} + \sum_{i\sigma} E_f f^{\dagger}_{i\sigma} f_{i\sigma} + U_{fc} \sum_{i\sigma\sigma'} \hat{n}^{f}_{i\sigma} \hat{n}^{c}_{i\sigma'} \tag{2.5}$$

The notation is the same as in the PAM (Eq. 1.9), defined in Chapter 1. The last term in Eq.

[6] $\mathrm{SmB_6}$ is nowadays classified as a Kondo Insulator [42].

(2.5) describes the repulsive interaction U_{fc} between conduction and local electrons [7]. Falicov and Kimball [41] established that critical interaction value U_{fc}^* separates continuous variations of the local levels occupation ($U_{fc}<U_{fc}^*$) as a function of E_f to first-order transitions($U_{fc}>U_{fc}^*$), where occupation jumps appeared.

The model in Equation 2.5 was studied using several approximations (analytical and numerical) and for different dimensions and lattice structures. Early works from Gonçalves da Silva and Falicov [43], Khomskii and Kocharjan [44], Hewson and Riseborough[45] and Singh *et al.* [46] pointed out the role of an additional hybridization in the Falicov-Kimball model using Hartree-Fock approximation. As a general result, these papers have confirmed the assertion that the repulsive interaction U_{fc}, if sufficiently large, would lead to valence jumps as a function of external parameters (incorporated by E_f) at $T=0$.

Recently the Falicov-Kimball model was subject of several other studies, mainly because its spin-less version can be seen as a simplified Hubbard model in which DMFT equations are exactly solvable. These considerations are out of the scope of the present thesis and the review article by Freericks and Zlatić [47] is recommended in this context.

2.3.3 Models explicitly including volume effects

Models containing explicitly volume effects were proposed to understand the unusual behavior in the γ-α transition of metallic Ce (cf. Section 2.1.2). In this compound a pressure-induced first order transition at $0.7GPa$ appears with a volume change close to 15%, as it was discussed in Section 2.1.2. The general idea of such models comes from the empirical fact that the Kondo temperature is strongly dependent on the volume[48, 49, 50]. Neutron scattering measurements of the resonant level width Γ, which is proportional to the Kondo temperature, give $\Gamma_\gamma=6-16meV$ and $\Gamma_\alpha>70meV$ for the γ and α phases of Ce, respectively[50].

The Kondo Volume Collapse model was proposed in 1982 concurrently by two different groups[51, 52]. Allen and Martin [51] have shown that an additional contribution to the free-energy from the coupling between $4f$ and conduction electrons must be considered. They have obtained from the equation of state, fed by experimental values, a first order transition with a critical endpoint close to $p_c=0.7GPa$ and $T_c=850K$. The estimated Kondo temperature are $T_{K\gamma}=54K$ and $T_{K\alpha}=765K$, which are close to the experimental results mentioned above.

In the work of Lavagna and collaborators[52] the Kondo lattice model was studied in the mean-field approximation[53] with a volume-dependent Kondo coupling $T_K(\mathcal{V}) \sim e^{-(\mathcal{V}-\mathcal{V}_0)/\mathcal{V}_0}$ ($\mathcal{V}_0$ is the volume at zero pressure). Following the same reasoning as above, they have obtained the isotherms in the p-$\mathcal{V}$ phase diagram.

The issue of Kondo Volume Collapse in the γ-α transition was later addressed from *ab initio* calculations using a combination of density functional theory (DFT) and dynamical mean-field theory[54, 55, 56]. Within this approach it is possible to incorporate the full set of f orbitals and the realistic band structure in the presence of strong correlations [57]. The results can be summarized by the figure 8 in Reference [55]. It shows an increasing spectral weight in the

[7] In the original work by Falicov and Kimball the local states represents holes, and not electrons, and U_{fc} is an attractive interaction instead of a repulsive one. Nevertheless it will be adopted the electronic version here to simplify the connection to our work later.

Fermi energy when the lattice volume is reduced, accompanied by a reduction of spectral weight in the Hubbard satellites. This corresponds to an increasing valence for Ce and a delocalization of the 4f electrons, as observed in experiments.

2.4 Summary

Let us summarize the aspects of valence transitions in lanthanide systems presented in this chapter. Firstly we have discussed the anomalous behavior of some lanthanide ions (such as Ce, Yb and Eu) in a crystalline environment that possesses two valence configurations very close in energy. It leads to an intermediate valence value that can be modified by applying pressure or doping the system. One example of such behavior is the metallic Ce (Section 2.1.2), in which the Ce valence vary discontinuously (at room temperature) from 3.06 to 3.67 by the application of pressure.

In Section 2.3 some techniques to perform valence measurements were presented. We have separated the techniques with respect to static and dynamic measurements. The former type relates the lanthanide valence to crystallographic and magnetic properties of the compound. In the latter group are placed more accurate and "modern" techniques, allowing a precise determination of valence. From this group we highlight the resonant inelastic X-ray scattering technique, which has been largely employed in the latest experimental works on the subject.

Lastly the most relevant models for valence transitions in rare-earth systems were discussed. The standard description is given by the Periodic Anderson model, which contains the Kondo and the intermediate valence regime and coherence among f electrons is taken in account (contrary to the single impurity model). Its major problem in the context of valence transitions is the absence of mechanisms to make it discontinuous, required to describe the compounds like the metallic Ce.

Two possible improvements on the issue of discontinuous transitions are the inclusion of a local electronic repulsion among conduction and localized electrons (Falicov-Kimball interaction) or explicit volume effects (volume collapse models). While the volume collapse approach is focused on the Kondo lattice regime, the Falicov-Kimball interaction plays a big role in the mixed-valence phase and it might be the origin of first-order transitions for compounds with large valence changes. Having it on mind, we will present in details the model chosen to describe valence transitions in the thesis.

Chapter 3

The Extended Periodic Anderson Model

In this chapter we present the model that will be employed in the description of valence transitions of lanthanide compounds. The basic idea is to include in the Periodic Anderson model (Eq.1.9) an additional Falicov-Kimbal interaction (Section 2.3.2) in order to have the combined effects of Coulomb repulsions (intraorbital and interobital) and the hybridization between the two orbitals. As we shall confirm in the next chapter results, the Falicov-Kimball interaction will be the driving mechanism to render valence transitions discontinuos, what is not expected in the original PAM.

The Extended Periodic Anderson model (EPAM) hamiltonian is the following:

$$\mathcal{H}_{EPAM} = \sum_{\mathbf{k}\sigma} \epsilon(\mathbf{k}) c^{\dagger}_{\mathbf{k}\sigma} c_{\mathbf{k}\sigma} + E_f \sum_{i\sigma} f^{\dagger}_{i\sigma} f_{i\sigma} + U \sum_{i} \hat{n}^{f}_{i\uparrow} \hat{n}^{f}_{i\downarrow} + V \sum_{i\sigma} \left(c^{\dagger}_{i\sigma} f_{i\sigma} + f^{\dagger}_{i\sigma} c_{i\sigma} \right) + U_{fc} \sum_{i\sigma\sigma'} \hat{n}^{f}_{i\sigma} \hat{n}^{c}_{i\sigma'} \quad (3.1)$$

In this hamiltonian, $\epsilon(\mathbf{k})$ is the kinetic energy of conduction electrons (being D its bandwidth), E_f is the energy of local (f) level in each site of the lattice, U is the Coulomb repulsion given that the local level in the site i is doubly occupied, V is the hybridization between the conduction band and f orbitals and U_{fc} is the local Coulomb repulsion among conduction and f electrons. We will consider a fixed total (c+f) number of electrons *per lattice site* n_{tot}, which determine the chemical potential μ.

The model above retains *a priori* the most relevant physical aspects of the problem. For instance, we are keeping only a single f orbital instead of the seven possible in the case (L=3), which is justifiable by the considerations of the Hund's rules and crystal field done in Section 4.2.2. The hybridization is assumed constant, even though it may have a *k*-dependence for symmetry reasons.

The EPAM hamiltonian in Eq. 3.1 cannot be solved without using approximations for the interacting terms. Obviously the approximation scheme must be consistent with the energy

magnitudes of the system that we want to describe, then let us point out briefly the energy scales of the problem, and afterwards we present our approximation scheme to solve this problem.

3.1 Energy scales in EPAM

The kinetic energy of conduction electrons is roughly proportional to the bandwidth of each material, which depends (among other things) on the type of relevant orbitals that combine to form the conduction band. In a common metal, containing mainly *s* and *p* orbitals, the bandwidths are as large as $10eV$. However these typical values are one order of magnitude smaller ($1eV$) for intermetallic systems, since the composition of the relevant conduction bands (those that are close to the Fermi energy) contain an important amount of *d* orbitals.

Regarding the hybridization values, it also depends on the material band structure. It corresponds to the overlap between the atomic 4f wave-functions and the Bloch states representing conduction electrons. Its typical values are $0.1eV$.

The f level energy, E_f, is not a simple quantity to be measured experimentally. In order to achieve an intermediate valence state it is crucial that the local level lies inside the conduction band, otherwise one would obtain only integer values for the valence. In this case E_f must be in the same range of energy as the electronic bandwidth ($1eV$). One would expect that the valence variations in this model happen when E_f is close to the chemical potential, a picture that will be verified in the results of Chapter 4.

Lastly the energy scales of the two Coulomb interactions, U and U_{fc}, must be analyzed. Even if they share the same physical origin, the electromagnetic interaction between pairs of electrons, their magnitudes are quite different. The intra-orbital interaction U is, by far, the largest energy involved in the problem. Its values observed by photoemission and absorption experiments in rare-earth ions are in the range of 5 to $10eV$.

Term	Energy scale
D	1 eV
E_f	1 eV
V	0.1 eV
U	5-10 eV
U_{fc}	? eV

Table 3.1: The energy magnitude of each term in hamiltonian 3.1.

The value of U_{fc} interaction

The most important question that arises in the analysis of the energy scales of the EPAM is the value of the interaction U_{fc}. This question, as far as I know, is still open and there is not much information in the literature.

Within a first principle approach, U_{fc} should be calculated from an expression of the type:

$$U_{fc} = \int \phi_c^*(\mathbf{r}')\phi_f^*(\mathbf{r})\frac{e^2}{|\mathbf{r}-\mathbf{r}'|}\phi_c(\mathbf{r}')\phi_f(\mathbf{r})d\mathbf{r}d\mathbf{r}' \tag{3.2}$$

Here $\phi_c(\mathbf{r})$ and $\phi_f(\mathbf{r})$ are the Wannier functions corresponding to conduction and localized electrons. This direct Couloumb interaction is strongly reduced by screening effects and quite often is neglected in other compounds. In lanthanides it might be relevant if $\phi_c(\mathbf{r})$ contains a large contribution from *d* orbitals.

The simple argument that relates the magnitude of U_{fc} to the amount of d orbitals that form the conduction band is qualitatively verified in two cerium compounds: metallic Ce and $\mathrm{CeCu_2Si_2}$. The former compound possesses d states close to the Fermi energy, while in the latter s and p orbitals from the anionic part are dominant. Then U_{fc} is expected to be larger in Ce than in $\mathrm{CeCu_2Si_2}$, and only one of them, Ce, shows a first-order valence transition. A detailed discussion of several compounds will be done in Section 4.3 and the point made here to justify the addition of the Falicov-Kimball interaction will be reviewed.

3.2 Previous works

The EPAM was studied in several works. An early study [46] on the context of Falicov-Kimball model have pointed out the suitability of EPAM for the valence transitions in SmS. The rebirth of the model came in 2000 when Onishi and Miyake proposed [58, 59] its use to explain the unusual superconductivity of $\mathrm{CeCu_2Si_2}$[60], in which the superconducting dome has an anomalous pressure dependence.

Further investigations using different methods were made. The magnetic field dependence of valence transitions was studied in slave-boson mean-field theory [61] and applied to compounds as $\mathrm{CeRhIn_5}$ [62] and $\mathrm{YbXCu_4}$ ($\mathrm{X = In, Ag, Cd}$)[63]. In unidimensional systems DMRG was employed to analyse charge, spin and superconducting correlations [64, 65], confirming the connection between valence fluctuations and superconductivity in the model. Other approaches include DMFT [66], variational Monte Carlo [59] and projector-based renormalization method [67].

In all the works mentioned in this section, the effect of U_{fc} is observed: a continuous valence variation as a function of other model parameters (for instance, E_f) becomes a first-order valence transition above a critical value of U_{fc}. This critical value defines a quantum critical endpoint in E_f-U_{fc} phase diagram, whose generic form (see Figure 4.1) is independent of the dimensionality or method employed. In the next section we describe the approximations we have used for the EPAM.

3.3 Approximations for the Extended Periodic Anderson Model

3.3.1 U_{fc} term: the mean-field approximation

Following the discussions in Section 3.1, we might safely assume that the Falicov-Kimball interaction is weaker than the Coulomb repulsion U and, possibly, smaller or of the same order as the electronic bandwidth D. In this case the simplest treatment is the mean-field approximation for this interaction.

The mean-field approximation for a two-body interaction term is based on the substitution of the one-body operators by their average value (denoted by $<\hat{n}^f_{i\sigma}>$) and a fluctuation around it:

$$\hat{n}^f_{i\sigma} \equiv <\hat{n}^f_{i\sigma}> + \delta\hat{n}^f_{i\sigma}$$

Then:

$$\hat{n}^f_{i\sigma}\hat{n}^c_{i\sigma'} = <\hat{n}^f_{i\sigma}><\hat{n}^c_{i\sigma}> + <\hat{n}^f_{i\sigma}>\delta\hat{n}^c_{i\sigma'} + <\hat{n}^c_{i\sigma'}>\delta\hat{n}^f_{i\sigma} + \delta\hat{n}^f_{i\sigma}\delta\hat{n}^c_{i\sigma'} \tag{3.3}$$

Assuming that the fluctuations are small, the term in $(\delta n)^2$ can be neglected and it is possible to write:

$$\hat{n}^f_{i\sigma}\hat{n}^c_{i\sigma'} = <\hat{n}^c_{i\sigma'}>\hat{n}^f_{i\sigma} + <\hat{n}^f_{i\sigma}>\hat{n}^c_{i\sigma'} - <\hat{n}^f_{i\sigma}><\hat{n}^c_{i\sigma'}> \tag{3.4}$$

We are interested in homogeneous mixed valence states, then the average occupation of c and f electrons in all lattice sites must be exactly the same. It implies that the averages on Equation 3.4 are site independent. With this restriction, the Falicov-Kimball interaction to be considered from now is:

$$V_{FK} = U_{fc}\sum_{i\sigma}\left(n_c\hat{n}^f_{i\sigma} + n_f\hat{n}^c_{i\sigma}\right) - NU_{fc}n_fn_c \tag{3.5}$$

We have defined the averages $n_f = <\hat{n}^f_{i\uparrow}> + <\hat{n}^f_{i\downarrow}>$ and $n_c = <\hat{n}^c_{i\uparrow}> + <\hat{n}^c_{i\downarrow}>$, for shortness. Note that the effect of V_{FK} in mean-field approximation is to shift the positions of the f-level and the conduction band center. The shift for each type of orbital (c or f) depends on the average charge on the other orbital, as expected by hand-waving arguments concerning the electrostatic nature of this interaction.

Replacing the Falicov-Kimball term V_{FK} in Eq.3.1, it reads:

$$\mathcal{H}_{EPAM} = \sum_{\mathbf{k}\sigma}\widetilde{\varepsilon}_c(\mathbf{k})c^\dagger_{\mathbf{k}\sigma}c_{\mathbf{k}\sigma} + \widetilde{\varepsilon}_f\sum_{i\sigma}f^\dagger_{i\sigma}f_{i\sigma} + U\sum_{i\sigma}\hat{n}^f_{i\uparrow}\hat{n}^f_{i\downarrow} + V\sum_{i\sigma}\left(c^\dagger_{i\sigma}f_{i\sigma} + f^\dagger_{i\sigma}c_{i\sigma}\right) - NU_{fc}n_fn_c \tag{3.6}$$

The definitions of $\widetilde{\varepsilon}_c(\mathbf{k})$ and $\widetilde{\varepsilon}_f$ are:

$$\widetilde{\varepsilon}_c(\mathbf{k}) = \epsilon(\mathbf{k}) + U_{fc} n_f \tag{3.7}$$

$$\widetilde{\varepsilon}_f = E_f + U_{fc} n_c \tag{3.8}$$

The Hartree-Fock approximation for the Falicov-Kimball interaction in the context discussed here was employed before[45, 46]. Even at this level of approximation the valence change is strongly enhanced by U_{fc} and first-order valence transitions are possible[46]. In fact the role of U_{fc} in the valence transitions is qualitatively captured in this level of approximation, since it is an interaction with local origin[68]. Then it is appropriate to keep this level of approximation if one is not interested on the critical behavior of the model or features connected to fluctuations (as the valence fluctuation mechanism to superconductivity[68]).

3.3.2 U term: Hubbard-I approximation

The strong correlation effects due to the local Coulomb repulsion inside the f orbitals requires different treatment than the mean-field approximation that was carried out for the Falicov-Kimball term U_{fc}. The simpler and first approximation proposed to deal with it was made by Hubbard[69, 70] in the context of the Hubbard model, which is nowadays called Hubbard-I approximation.

The core of Hubbard-I approximation consist in substituting the self-energy term for the Coulomb interaction in the electronic propagator by the atomic self-energy of the problem[1] [71]. Since the Hilbert space of the atomic problem contains only four states, it is simple to write down the self-energy in this limit. So the starting point is to consider local 4f levels splitted in two well separated levels with energy E_f and $E_f + U$ [2], with the spectral weight correctly divided between those levels. After that we will take the infinite U limit only the lower sub-band survives and its integrated spectral weight is at most one, once the double occupation is forbidden in this limit. For this reason, the hybridization between conduction and f electrons is modified because conduction electrons cannot hybridized with f electrons from the upper subband.

The main reason to adopt the Hubbard-I scheme relies on its correct treatment of the spectral weight in the mixed-valence regime of EPAM. The spectral weight is a crucial quantity in valence transitions since it is precisely the *integrated spectral weight* that yields the occupation of f orbitals (the valence). The Hubbard-I approximation for the EPAM has an important limitation: it cannot describe the crossover from the mixed-valent to the Kondo lattice regime. The reason for that is the absence of the quasiparticle peak at the Fermi energy (see discussion in Section 1.2) within this approximation, which is inherent to all the physics of Kondo effect.

In the present subsection we will present the Hubbard-I approximation for EPAM in a pedagogical form, by following the steps described above. A second derivation, based on the equation of motions for the Green's functions, is presented in Appendix A.

[1] The atomic limit is formally obtained when the electronic bandwidth is taken to zero (for the Hubbard model).

[2] If the f electrons had dispersion, it would correspond to the center of the *lower* and *upper* Hubbard sub-bands or satellites.

Let us start by the f-electron "atomic" hamiltonian:

$$\mathcal{H}_f = \sum_{i\sigma} \widetilde{\varepsilon}_{f\sigma} f^\dagger_{i\sigma} f_{i\sigma} + U \sum_i f^\dagger_{i\uparrow} f_{i\uparrow} f^\dagger_{i\downarrow} f_{i\downarrow} \tag{3.9}$$

Here the one electron energy $\widetilde{\varepsilon}_{f\sigma}$ (Eq. 3.8) is modified to take into account a possible spin dependence of the atomic levels, what will be important when magnetism is present (Section 4.2).

The equation of motion for the Green's function[3] $g^{ff}_{ii,\sigma}(\omega) \equiv \ll f_{i\sigma}\,;\, f^\dagger_{i\sigma} \gg$ with respect to the hamiltonian $\mathcal{H}_{at}$ yields:

$$\omega \ll f_{i\sigma}\,;\, f^\dagger_{i\sigma} \gg = 1 + \widetilde{\varepsilon}_{f\sigma} \ll f_{i\sigma}\,;\, f^\dagger_{i\sigma} \gg + U \ll \hat{n}^f_{i\overline{\sigma}} f_{i\sigma}\,;\, f^\dagger_{i\sigma} \gg \tag{3.10}$$

On the right side of equation above it appears a higher-order Green's function $\ll \hat{n}^f_{i\overline{\sigma}} f_{i\sigma}; f^\dagger_{i\sigma} \gg$, which has an equation of motion given by:

$$\omega \ll \hat{n}^f_{i\overline{\sigma}} f_{i\sigma}\,;\, f^\dagger_{i\sigma} \gg = < \hat{n}^f_{i\overline{\sigma}} > + (\widetilde{\varepsilon}_{f\sigma} + U) \ll \hat{n}^f_{i\overline{\sigma}} f_{i\sigma}\,;\, f^\dagger_{i\sigma} \gg \tag{3.11}$$

This equation gives:

$$\ll \hat{n}^f_{i\overline{\sigma}} f_{i\sigma}\,;\, f^\dagger_{i\sigma} \gg = \frac{< \hat{n}^f_{i\overline{\sigma}} >}{\omega - \widetilde{\varepsilon}_{f\sigma} - U} \tag{3.12}$$

Plugging it on Equation 3.10 and performing some algebra, $g^{ff}_{ii,\sigma}(\omega)$ is obtained:

$$g^{ff}_\sigma(\omega) = \frac{1 - < \hat{n}^f_{i\overline{\sigma}} >}{\omega - \widetilde{\varepsilon}_{f\sigma}} + \frac{< \hat{n}^f_{i\overline{\sigma}} >}{\omega - \widetilde{\varepsilon}_{f\sigma} - U} \tag{3.13}$$

The interpretation of this expression is very simple. Basically it says that an electron with spin σ in a f orbital would have an energy $\widetilde{\varepsilon}_{f\sigma}$ if there is no other electron on site i, which has a probability $1 - < \hat{n}^f_{i\overline{\sigma}} >$ to happen. Otherwise it will interact with the other spin and its energy would be $\widetilde{\varepsilon}_{f\sigma} + U$. This local approach is exact for the hamiltonian in Eq. 3.9. In a lattice, the approximation is made when the local term $< \hat{n}^f_{i\sigma} >$ is replaced by its average over all the N lattice sites:

$$n_{f,\sigma} = \frac{1}{N} \sum_i < \hat{n}^f_{i\sigma} >$$

In this case translational invariance is imposed, as in Equation 3.5, in order to describe homogeneous intermediate valence states.

In Section 3.1 it was mentioned that the Coulomb interaction U is the largest energy of the problem ($\sim 10eV$). Therefore the energetic separation between the two poles of $\ll f_{i\sigma}\,;\, f^\dagger_{i\sigma} \gg$ is much larger than the bandwidth of conduction electrons and the doubly occupied state (associated to the pole $\widetilde{\varepsilon}_{f\sigma} + U$) is rarely reached. So, in a good approximation, one can neglect the second term in Eq.3.13 by taking the limit $U \to +\infty$.

[3] We use the Zubarev's notation[72] for Green's functions in the derivation present here and in the Appendix B.

In the limit $U \to \infty$, Eq. 3.13 is written as:

$$g_\sigma^{ff}(\omega) = \lim_{U\to+\infty} \ll f_{i\sigma}\,;f_{i\sigma}^\dagger \gg \equiv \frac{p_\sigma}{\omega - \widetilde{\varepsilon}_{f\sigma}}, \tag{3.14}$$

being

$$p_\sigma \equiv 1 - n_{f,\bar{\sigma}} \tag{3.15}$$

For the non-magnetic case $E_{f\sigma}$, p_σ and $g_\sigma^{ff}(\omega)$ are independent of spin. Then:

$$g^{ff}(\omega) = \frac{p}{\omega - \widetilde{\varepsilon}_f} \tag{3.16}$$

and

$$p \equiv p_\uparrow = p_\downarrow = 1 - \frac{n_f}{2}. \tag{3.17}$$

Summarizing the important results in this section: from the f-electron local hamiltonian in Eq.3.9, we computed the local Green's function $g_\sigma^{ff}(\omega)$ (Eq. 3.13), which has a two-pole structure. This function can be further simplified if we take the limit $U \to +\infty$ and assume a paramagnetic phase. In its final expression, $g_\sigma^{ff}(\omega)$ has a single pole in E_f and its spectral weight is p, which is reminiscent of the strong correlation from U and provides the constraint $n_f \leq 1$ for the f-level occupation.

3.3.3 Green's functions

Once explained the approximations for the interacting terms U_{fc} and U, the next step is to write the Green's function for the complete EPAM hamiltonian. We first note that the EPAM hamiltonian from Eq. 3.6 has the following form:

$$\mathcal{H}_{EPAM} = \mathcal{H}_f + \mathcal{H}_c + \mathcal{H}_V - U_{fc} n_c n_f$$

The f-electrons term $\mathcal{H}_f$ was treated in the Hubbard-I with $U \to \infty$ and its associated Green's function $g_\sigma^{ff}(\omega)$ is given in Eq. 3.14. The second term is the c-electron part of the hamiltonian:

$$\mathcal{H}_c = \sum_{\mathbf{k}\sigma} \widetilde{\varepsilon}_{c,\sigma}(\mathbf{k}) c_{\mathbf{k}\sigma}^\dagger c_{\mathbf{k}\sigma} \tag{3.18}$$

Defining $g_\sigma^{cc}(\mathbf{k},\omega)$ as the conduction electrons Green's function for the $\mathcal{H}_c$ term, we have:

$$g_\sigma^{cc}(\mathbf{k},\omega) = \frac{1}{\omega - \widetilde{\varepsilon}_c(\mathbf{k})} \tag{3.19}$$

The Green's functions $g_\sigma^{ff}(\omega)$ and $g_\sigma^{cc}(\mathbf{k},\omega)$ correspond to the GF in the absence of hybridization. In order to include the hybridization term $\mathcal{H}_V$, we proceed by writing two Dyson equations for the complete GF $G_\sigma^{cc}(\mathbf{k},\omega)$ and $G_\sigma^{ff}(\mathbf{k},\omega)$:

$$[G_\sigma^{cc}(\mathbf{k},\omega)]^{-1} = [g_\sigma^{cc}(\mathbf{k},\omega)]^{-1} - \Sigma_\sigma^c(\mathbf{k},\omega), \tag{3.20}$$

$$\left[G^{ff}_{\sigma}(\mathbf{k},\omega)\right]^{-1} = \left[g^{ff}_{\sigma}(\mathbf{k},\omega)\right]^{-1} - \Sigma^{f}_{\sigma}(\mathbf{k},\omega), \tag{3.21}$$

The self-energy $\Sigma^{c}_{\sigma}(\mathbf{k},\omega)$ denotes the process that an c-electron hops on and off the f-level (and vice-versa for $\Sigma^{f}_{\sigma}(\mathbf{k},\omega)$). The self-energies are given by:

$$\Sigma(\omega)^{c}_{\sigma} = g^{ff}_{\sigma}(\omega)V^2 \tag{3.22}$$

$$\Sigma(\omega)^{f}_{\sigma} = g^{cc}_{\sigma}(\omega)V^2 \tag{3.23}$$

Substituting Eqs.3.14,3.19,3.22 and 3.23 in Eqs. 3.20 and 3.21, one obtains:

$$G^{cc}_{\sigma}(\mathbf{k},\omega) = \frac{1}{\omega - \widetilde{\varepsilon}_{c}(\mathbf{k}) - \frac{p_{\sigma}V^2}{\omega - \widetilde{\varepsilon}_{f,\sigma}}} \tag{3.24}$$

$$G^{ff}_{\sigma}(\mathbf{k},\omega) = \frac{p_{\sigma}}{\omega - \widetilde{\varepsilon}_{f,\sigma} - \frac{p_{\sigma}V^2}{\omega - \widetilde{\varepsilon}_{c,\sigma}(\mathbf{k})}} \tag{3.25}$$

The parameters $\widetilde{\varepsilon}_{c}(\mathbf{k})$, $\widetilde{\varepsilon}_{f}$ and p are given by Eqs. 3.7, 3.8 and 3.17, respectively.

3.4 Properties of the model

The approximations presented in Section 3.3 enable us to write down the Green's functions for the present problem. In the current section we will show some results using a generic form for the conduction band. For the numerical calculations, it will be later simplified under the assumption of a constant density of states for the non-interacting conduction band.

Quasiparticles spectra

The excitation energies of quasiparticles correspond to the poles of the Green's functions (Eqs.3.24 and 3.25). These poles are the solutions of:

$$(\omega - \widetilde{\varepsilon}_{c}(\mathbf{k}))(\omega - \widetilde{\varepsilon}_{f}) - pV^2 = 0$$

We find two branches of poles:

$$\omega_{\alpha}(\mathbf{k}) = \frac{\widetilde{\varepsilon}_{c}(\mathbf{k}) + \widetilde{\varepsilon}_{f}}{2} + \alpha\sqrt{\left(\frac{\widetilde{\varepsilon}_{c}(\mathbf{k}) - \widetilde{\varepsilon}_{f}}{2}\right)^2 + pV^2}, \tag{3.26}$$

in which $\alpha = -1, +1$.

If $V = 0$, then the problem is completely separable in terms of conduction and f electrons and the quasiparticles' energies corresponds to $\widetilde{\varepsilon}_{c}(\mathbf{k})$ and $\widetilde{\varepsilon}_{f}$ (defined in Eqs.3.7 and 3.8), as expected. For finite V, the quasiparticles wave functions are linear combination of c and f electrons and the spectrum exhibit features of both types of electrons. In the region around the initial f-level $\widetilde{\varepsilon}_{f}$ an *hybridization gap* appears and the quasiparticles have a prevailing

local character. Far from the gap the quasiparticle bands are wider and close to the initial conduction band. This is a general feature of the Periodic Anderson model and it will reappear in the discussion of the Kondo Lattice model in Part 2.

The Green's functions in Eqs. 3.24 and 3.25 can be rewritten in terms of the two quasiparticle energy given in Eq.3.26. The decomposition of $G^{cc}_{\sigma}(\mathbf{k},\omega)$ and $G^{ff}_{\sigma}(\mathbf{k},\omega)$ in partial fractions immediately shows the spectral function of each quasiparticle branch:

$$G^{cc}_{\sigma}(\mathbf{k},\omega) = \frac{\left(\frac{\widetilde{\varepsilon}_f - \omega_-(\mathbf{k})}{\omega_+(\mathbf{k}) - \omega_-(\mathbf{k})}\right)}{\omega - \omega_-(\mathbf{k})} + \frac{\left(-\frac{\widetilde{\varepsilon}_f - \omega_+(\mathbf{k})}{\omega_+(\mathbf{k}) - \omega_-(\mathbf{k})}\right)}{\omega - \omega_+(\mathbf{k})} \tag{3.27}$$

$$G^{ff}_{\sigma}(\mathbf{k},\omega) = \frac{p\left(\frac{\widetilde{\varepsilon}_c(\mathbf{k}) - \omega_-(\mathbf{k})}{\omega_+(\mathbf{k}) - \omega_-(\mathbf{k})}\right)}{\omega - \omega_-(\mathbf{k})} + \frac{p\left(-\frac{\widetilde{\varepsilon}_c(\mathbf{k}) - \omega_+(\mathbf{k})}{\omega_+(\mathbf{k}) - \omega_-(\mathbf{k})}\right)}{\omega - \omega_+(\mathbf{k})} \tag{3.28}$$

The total spectral function is $A^{tot}_{\pm}(\mathbf{k})$ defined by

$$G^{cc}_{\sigma}(\mathbf{k},\omega) + G^{ff}_{\sigma}(\mathbf{k},\omega) \equiv \frac{A^{tot}_{-}(\mathbf{k})}{\omega - \omega_-(\mathbf{k})} + \frac{A^{tot}_{+}(\mathbf{k})}{\omega - \omega_+(\mathbf{k})}, \tag{3.29}$$

one obtain:

$$A^{tot}_{-}(\mathbf{k}) = \frac{p\left(\widetilde{\varepsilon}_c(\mathbf{k}) - \omega_-(\mathbf{k})\right) + \widetilde{\varepsilon}_f - \omega_-(\mathbf{k})}{\omega_+(\mathbf{k}) - \omega_-(\mathbf{k})} \tag{3.30}$$

$$A^{tot}_{+}(\mathbf{k}) = \frac{-p\left(\widetilde{\varepsilon}_c(\mathbf{k}) - \omega_+(\mathbf{k})\right) - \widetilde{\varepsilon}_f + \omega_+(\mathbf{k})}{\omega_+(\mathbf{k}) - \omega_-(\mathbf{k})} \tag{3.31}$$

Simplifying these expressions:

$$A^{tot}_{-}(\mathbf{k}) = \frac{(1+p)(\omega_+ - \widetilde{\varepsilon}_f) - (\widetilde{\varepsilon}_c(\mathbf{k}) - \widetilde{\varepsilon}_f)}{\omega_+(\mathbf{k}) - \omega_-(\mathbf{k})} \tag{3.32}$$

$$A^{tot}_{+}(\mathbf{k}) = \frac{(1+p)(\omega_+ - \widetilde{\varepsilon}_f) - p(\widetilde{\varepsilon}_c(\mathbf{k}) - \widetilde{\varepsilon}_f)}{\omega_+(\mathbf{k}) - \omega_-(\mathbf{k})} \tag{3.33}$$

Note that only the second term in the expression above is different by a factor p. It means that the total density of states is asymmetrical with respect to $\widetilde{\varepsilon}_f$. This results contrasts with the non-interacting case ($U=0$), since in the absence of the renormalization of V both spectral weights $A^{tot}_{\pm}(\mathbf{k})$ would be equal.

Density of states

Let us suppose that we know the non-interacting density of states for the conduction electrons. This quantity is defined as

$$\rho_0(\omega) = \frac{1}{N}\sum_{\mathbf{k}} \delta(\omega - \varepsilon_c(\mathbf{k})), \tag{3.34}$$

where N is the total number of sites and δ is the Dirac distribution. The function $\rho_0(\omega)$ is assumed to be compact, i.e. it is non-zero in a limited region of the real space ($\omega \in [-D; D]$,

D is the half bandwidth). This assumption is not restrictive, since physically the bandwidths must be in a finite interval of energies.

Thanks to the monotonicity of the quasiparticle spectra in Equation 3.26, it is possible to use the non-interacting density ρ_0 and the other parameters in the problem to write down the densities of states ρ_{cc} and ρ_{ff} associated to the Green's functions G^{cc} and G^{ff}, respectively. The trick[73] involves a change of variables that highlights all the generic properties of these functions without appealing to a specific form of ρ_0.

The expressions for ρ_{cc} and ρ_{ff} are:

$$\rho_{cc}(\omega) = \rho_0 \left(\omega - \frac{pV^2}{\omega - \widetilde{\varepsilon}_f} \right) \tag{3.35}$$

$$\rho_{ff}(\omega) = \left(\frac{pV}{\omega - \widetilde{\varepsilon}_f} \right)^2 \rho_0 \left(\omega - \frac{pV^2}{\omega - \widetilde{\varepsilon}_f} \right) \tag{3.36}$$

From the density of state it is possible to obtain the occupation numbers and the energy *per* site of the ground-state at zero temperature. The latter quantity is expressed as

$$\frac{E_{tot}}{N} = 2 \int_{-\infty}^{\mu} d\omega \omega \left(\rho_{cc}(\omega) + \rho_{ff}(\omega) \right) - U_{fc} n_c n_f, \tag{3.37}$$

where the second term comes from the mean-field approximation on the U_{fc} term(Eq. 3.5).

Particular case: constant $\rho_0(\omega)$

After the discussion of the general properties of the density of states, I want to focus on the approximations made in order to determine the core results that will appear in the next chapter. For that reason we will further simplify the expressions, using a constant density of states in the interval $\omega \in [-D; D]$ and normalized to 1:

$$\rho_0(\omega) = \begin{cases} \frac{1}{2D} & \text{if } |\omega| \leq D \\ 0 & otherwise \end{cases}$$

The advantage of considering such form lies on the simple expressions for $\rho_{cc}(\omega)$ and $\rho_{ff}(\omega)$ that it yields, leaving them easy to be integrated. The plots of $\rho_{cc}(\omega)$ and $\rho_{ff}(\omega)$ are schematically represented in Figure 3.1 for arbitrary values of parameter. These functions are

non-zero inside two disconnected energy regions defined by their extrema:

$$\omega_1 = \frac{\widetilde{\varepsilon}_c(-D) + \widetilde{\varepsilon}_f}{2} - \sqrt{\left(\frac{\widetilde{\varepsilon}_c(-D) - \widetilde{\varepsilon}_f}{2}\right)^2 + pV^2} \tag{3.38}$$

$$\omega_2 = \frac{\widetilde{\varepsilon}_c(+D) + \widetilde{\varepsilon}_f}{2} - \sqrt{\left(\frac{\widetilde{\varepsilon}_c(+D) - \widetilde{\varepsilon}_f}{2}\right)^2 + pV^2} \tag{3.39}$$

$$\omega_3 = \frac{\widetilde{\varepsilon}_c(-D) + \widetilde{\varepsilon}_f}{2} + \sqrt{\left(\frac{\widetilde{\varepsilon}_c(-D) - \widetilde{\varepsilon}_f}{2}\right)^2 + pV^2} \tag{3.40}$$

$$\omega_4 = \frac{\widetilde{\varepsilon}_c(+D) + \widetilde{\varepsilon}_f}{2} + \sqrt{\left(\frac{\widetilde{\varepsilon}_c(+D) - \widetilde{\varepsilon}_f}{2}\right)^2 + pV^2} \tag{3.41}$$

Here we have used $\widetilde{\varepsilon}_c(\pm D) = \pm D + U_{fc} n_f$.

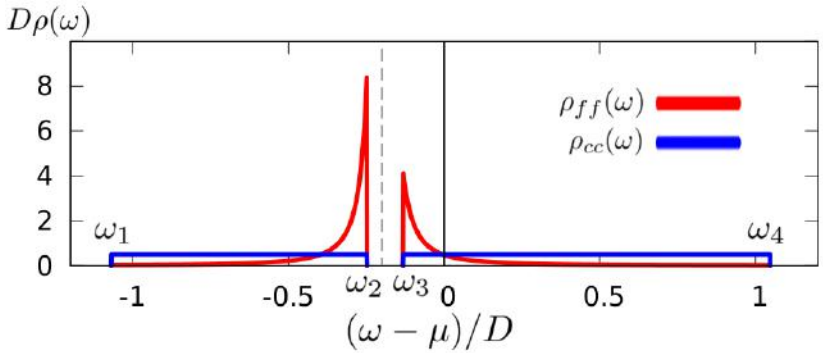

Figure 3.1: Schematic plot of partial densities of states $\rho_{ff}(\omega)$ (red) and $\rho_{cc}(\omega)$ (blue) in the constant ρ_0 approximation. The position of the f level $\widetilde{\varepsilon}_f$ is indicated in the dashed grey line and lies inside the hybdridization gap. Plot using arbitray parameters.

From now on, we will call the regions in the intervals $[\omega_1; \omega_2]$ and $[\omega_3; \omega_4]$ as the *lower* and *upper* energy bands, respectively. In Eqs. 3.38-3.41 the labels ω_i are defined to obey the relation:

$$\omega_1 < \omega_2 < \omega_3 < \omega_4$$

The two peaks appearing on the edges of the hybridization gap in $\rho_{ff}(\omega)$ are displayed in Figure 3.1. Their position with respect to the chemical potential is the crucial aspect of the valence transitions as we will see in the next chapter.

Chapter 4

Results

4.1 Results for non-magnetic phases

In this section some results obtained with the model developed in Chapter 3 will be presented. The interest here is to establish the valence dependence on the model parameters at zero and finite temperatures. The objective is to establish a theoretical background on the valence transition phenomenon that will be later applied to lanthanide compounds displaying such behavior.

4.1.1 Self-consistent solutions

All the results shown in this section were obtained through the solution of self-consistent equations. For the particular case of non-magnetic solutions, there are only two coupled equations involving the total number of electrons n_{tot} and the number of f electrons n_f in each site of the lattice. They are calculated from integrals over the density of states in Eqs.3.35 and 3.35,

Explicitly the self-consistent equations are:

$$n_{tot} = n_c + n_f = 2 \int_{-\infty}^{+\infty} d\omega f(\omega) \left(\rho_{ff}(\omega) + \rho_{cc}(\omega)\right) \tag{4.1}$$

and

$$n_f = 2 \int_{-\infty}^{+\infty} d\omega f(\omega) \rho_{ff}(\omega). \tag{4.2}$$

The integrals are weighted by the Fermi distribution

$$f(\omega) = \frac{1}{1 + e^{(\omega-\mu)/T}}, \tag{4.3}$$

where T is the temperature.

The densities of states to be integrated in the equations above depend themselves on the values of n_f and n_c in Eqs. 4.1 and 4.2 should be solved self-consistently. Their solutions are found using the bisection method for nonlinear equations[74]. The algorithm for numerical integration uses the Simpson rule with adaptive step and an absolute error of 10^{-7} is demanded for the integral.

4.1.2 Valence as a function of model parameters

The first result to be discussed is the phase diagram at zero temperature. As mentioned before, we are interested in the behavior of the valence by changing external parameters (as pressure, doping or temperature), so the relevant quantity for the moment will be the occupation number n_f.

Let us concentrate first on the case with constant concentration of electrons n_{tot} and hybridization V. In Figure 4.1 we have set $V = 0.1D$ and $n_{tot} = 1.5$ and we vary the f-level position E_f and interaction U_{fc}.

The generic form of this phase diagram can be divided in two regions with respect to U_{fc}. If U_{fc} is smaller than a critical value U^*_{fc}, the variation of n_f with respect to E_f occurs in a continuous form, from the complete occupation ($n_f = 1$) to the empty level($n_f = 0$). Then this particular region is named a *valence crossover* region. When U_{fc} is larger than U^*_{fc} the valence jumps abruptly from its largest ($n_f \approx 1$) to its smallest ($n_f \approx 0$) value by increasing E_f (see Fig. 4.4). This corresponds to a *first-order valence transition*.

The first-order valence transition line ends up in a quantum critical endpoint(QCEP) located at $E_f = -0.23D$ and $U_{fc} = 0.53D$. The position of the critical endpoint depends on the other parameters (V and n_{tot}), but the general shape of the phase diagram is rather universal.

In the crossover regime there are at least two important things to be observed. Firstly, U^*_{fc} is always finite and the case with zero Falicov-Kimball interaction, which corresponds to the "pure" Periodic Anderson model, is always a valence crossover. This interaction is responsible to turn the valence crossover to a discontinuously valence transition. Increasing U_{fc} from its zero value enhances the transition and narrows the parameter window where the valence changes.

The valence transition can be understood from the evolution of the total density of states $\rho_{tot}(\omega) = \rho_{ff}(\omega) + \rho_{cc}(\omega)$ with respect to E_f or U_{fc}. In Figure 4.2, ρ_{tot} is presented for three different points in the phase diagram of Fig.4.1, corresponding to the valence crossover region($U_{fc} = 0$). For the sake of comparison the energy axis is shifted by the chemical potential μ. The f peak in ρ_{tot}, located around $\widetilde{\varepsilon}_f = E_f + n_c U_{fc}$, gradually crosses the Fermi energy when E_f is increased. For $E_f = 0$ the peak coincides with the chemical potential, which characterizes the intermediate valence regime.

The physical interpretation of the U_{fc} effect is seen directly from the mean-field approximation employed for this term. Since the effective f-level is measured by $\widetilde{\varepsilon}_f = E_f + U_{fc} n_c$, its position depends on n_f for a non-zero U_{fc} interaction. So there is an additional feedback in the n_f variation proportional to U_{fc}. This feedback becomes critical for $U_{fc} = U^*_{fc}$ and above this point there is a discontinuity in $\widetilde{\varepsilon}_f$. From the point of view of the total density of states in Fig. 4.2, the discontinuity in $\widetilde{\varepsilon}_f$ represents a direct passage between the $n_f \approx 1$ (top) to

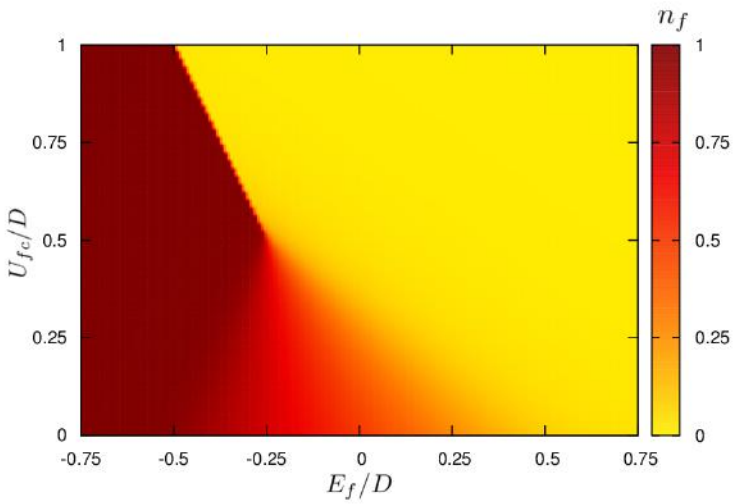

Figure 4.1: Zero temperature phase diagram of the EPAM model. The color map indicates the self-consistent valence n_f with respect to U_{fc} and E_f. Here $n_{tot} = 1.5$ and $V = 0.1D$. The critical endpoint is located at $U^*_{fc} = 0.53D$ and $E^*_f = -0.23D$ for the chosen parameters.

$n_f \approx 0$(bottom).

The enhancement of valence fluctuations observed in the phase diagram in Figure 4.1 that ends up in a first-order valence transition can be traced by another physical quantity: the charge susceptibility. It measures the system capacity in changing the valence of the f orbitals with an infinitesimal variation of an external parameter. The natural choice of parameter here is the position of the f levels E_f, which yields the following definition[1] for the charge susceptibility χ_{ch}:

$$\chi_{ch} = -\frac{\partial n_f}{\partial E_f} \tag{4.4}$$

In Figure 4.3 the charge susceptibility is plotted as a function of E_f and U_{fc} for the same parameters as in Figure 4.1. Some U_{fc}-constant curves are shown on Figure 4.4(bottom) to help the visualization. For small U_{fc} the charge susceptibility is a broad and flat function of E_f, characteristic of the crossover regime. Then it becomes narrower and higher [2] as U_{fc} approaches its critical value. For $U_{fc} \geq U^*_{fc}$, $\chi_{ch}(E_f)$ becomes a delta function peaked in a given E_f and its divergence signals the appearance of the first-order valence transition.

[1] In this definition all the other parameters (U_{fc}, V and n_{tot}) are implicitly kept constant.

[2] Note that the width and height of $\chi_{ch}(E_f)$ are inversely proportional quantities because the area under it is preserved:

$$\int_{-\infty}^{+\infty} dE_f \chi_{ch}(E_f) = n_f(-\infty) - n_f(+\infty) = 1$$

.

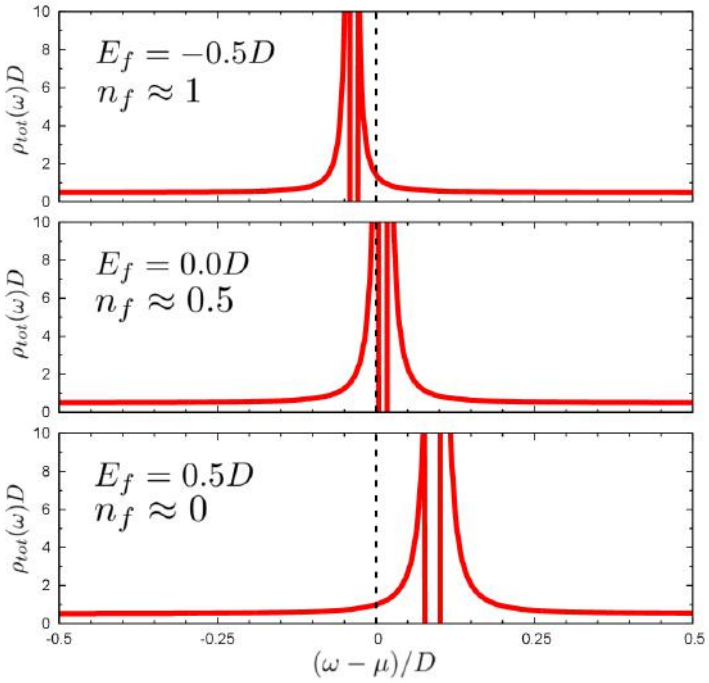

Figure 4.2: Total density of states $\rho_{tot}(\omega)$ for three points in the phase diagram ($U_{fc} = 0$): $E_f = -0.5D$ (top), $E_f = 0.0D$ (middle) and $E_f = 0.5D$ (bottom). The energy is measured with respect to the Fermi level, which is different in the three cases. The intermediate valence state correspond to the situation where the Fermi level is located in the peak of ρ_{tot}, as discussed in the text. Other parameters are $V = 0.1D$ and $n_{tot} = 1.5$.

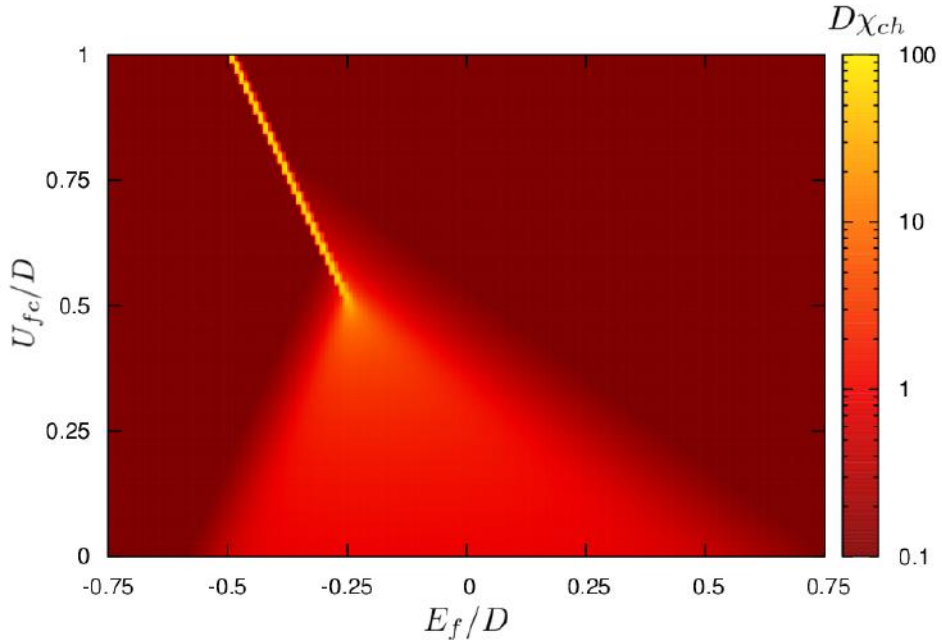

Figure 4.3: Charge susceptibility as a function of E_f and U_fc for $V = 0.1D$ and $n_{tot} = 1.5$. χ_{ch} is enhanced inside the crossover region close to the critical point. The divergence of this quantity marks the first-order valence transition.

Bands spectral weight and Fermi level position

The quasiparticle's spectral weight in Hubbard-I approximation was discussed in Section 3.4. By taking the infinite correlation limit, the double occupation of f-orbitals is completely excluded and, as consequence, the maximum number of electrons (per site) is 3, corresponding to $n_c = 2$ and $n_f = 1$. For this reason the total spectral weight for the lower and the upper part of the density of states (Eqs. 3.32 and 3.33) depend on $p = 1 - n_f/2$, which contrasts with the non-interacting case.

Given the non-trivial dependence on p and its consequences with respect to the sum rules, it is interesting to analyze it in more details. One important aspect is to compute the number states in each part (lower and upper) of the density of states, once it determines the chemical potential position and it allows us to pinpoint precisely if and when it crosses (or enters) the gap.

The number of states in the lower part is defined (for $T = 0$) as:

$$n_{lower} = 2\int_{\omega_1}^{\omega_2} d\omega \rho_{tot}(\omega) = \frac{\omega_2 - \omega_1}{D} - \frac{p^2V^2}{D(\omega_2 - \widetilde{\varepsilon}_f)} + \frac{p^2V^2}{D(\omega_1 - \widetilde{\varepsilon}_f)} \tag{4.5}$$

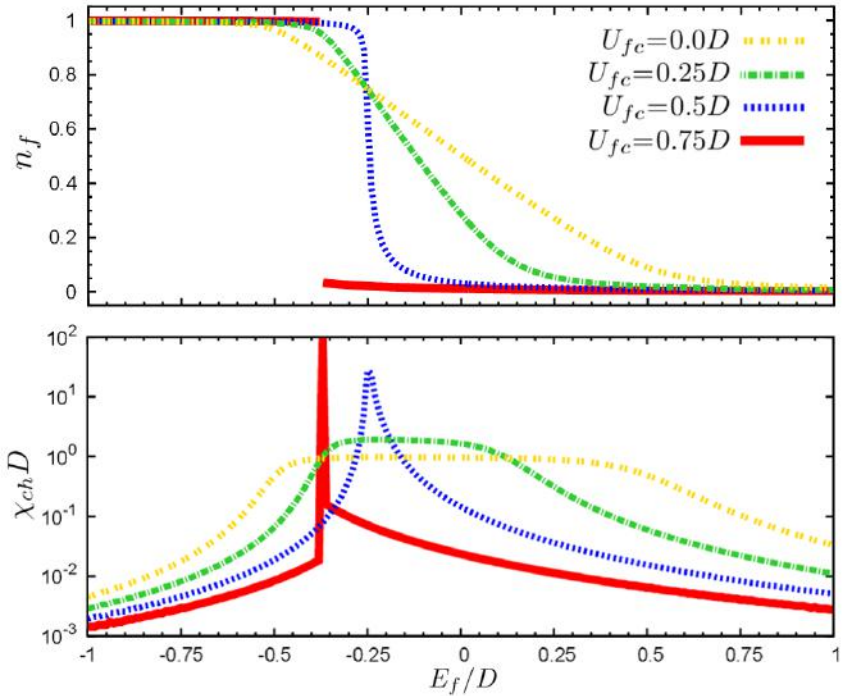

Figure 4.4: Valence n_f(top) and charge susceptibility χ_{ch} (bottom) as a function of E_f for four different values of U_{fc}.

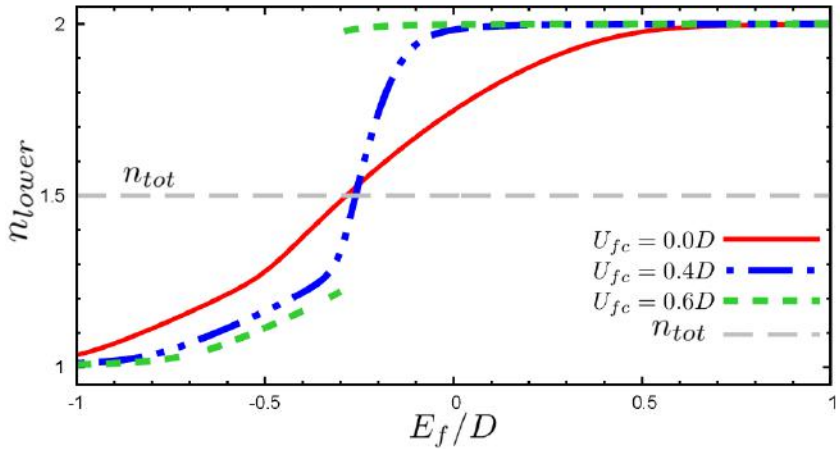

Figure 4.5: Total number of states $(c+f)$ in the lower sub-band n_{lower} as a function of E_f for three U_{fc} values: $U_{fc}=0$ (red solid), $U_{fc}=0.4D$ (blue dashed) and $U_{fc}=0.6D$ (green dot-dashed). For comparison n_{tot} is shown in the grey dashed line. The condition $n_{lower}=n_{tot}$ is satisfied only if $U_{fc}<U_{fc}^{*}$ and represents an insulating phase (see text). Other parameters are $V=0.1D$ and $n_{tot}=1.5$.

In Figure 4.5 n_{lower} (determined self-consistenly) is plotted as a function of E_f for three distinct values of U_{fc}. We consider $n_{tot}=1.5$ and $V=0.1D$, as in Figure 4.1. The grey dashed

line indicates the position of $n_{tot}=1.5$. We see that the relation $n_{lower}=n_{tot}$ is satisfied in one point only *if* the inter-orbital repulsion is smaller that its critical value U_{fc}^{*}. For these precise values of E_f the chemical potential lies in the hybridization gap and the system is an insulator. If $U_{fc} > U_{fc}^{*}$, then the position of the chemical potential jumps from the upper to the lower part of the density of states. Note that n_{lower} is bounded between 1 and 2 for *any* value of n_{tot}. It means that for $n_{tot} < 1$ and $n_{tot} > 2$ the chemical potential cannot move from one part of the DOS to the other , no matter what it the U_{fc} value. As a conclusion, the system behaves differently if n_{tot} is fixed between 1 and 2 (the case analysed so far) or if $n_{tot} < 1$ or $n_{tot} > 2$.

Electronic filling effects

Two different situations can happen in the EPAM with respect to the total electronic filling n_{tot}. If $1 < n_{tot} \leq 2$, then all the electrons in the system can be allocated in the conduction band (in the case of large E_f) and the occupation n_f varies between zero and one. This case was depicted in Figure 4.1.

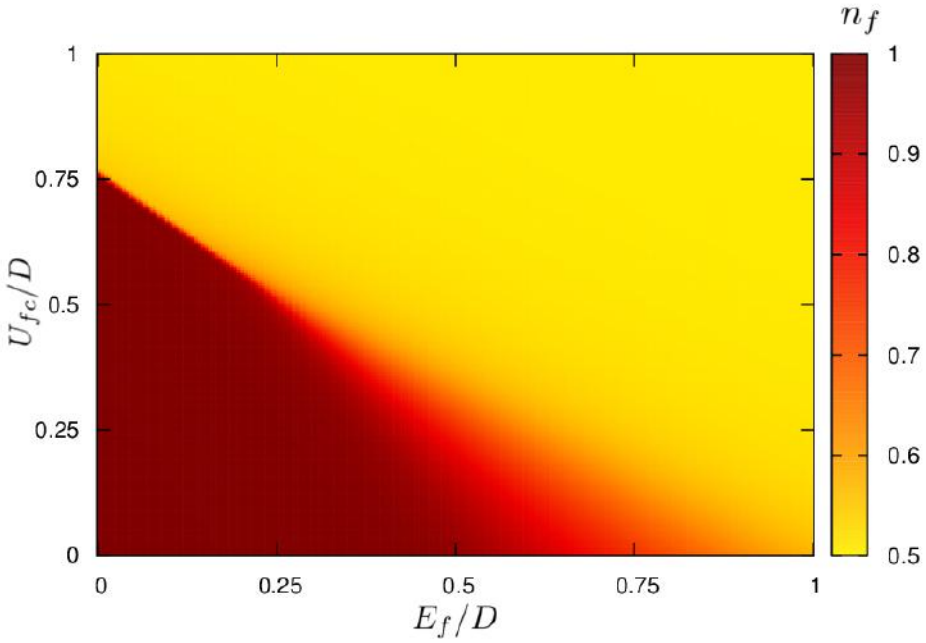

Figure 4.6: The same phase diagram as in Figure 4.1, but for a different electronic filling $n_{tot} = 2.5$. Note that the color map has a different scale and the lowest valence value is 0.5, indicated by the yellow region. The positions of the crossover region, the first-order transition line and the critical endpoint depend on n_{tot}. For these parameters, the critical endpoint is located at $U_{fc}^{*} = 0.55D$ and $E_f^{*} = 0.23D$.

The situation is modified if $n_{tot} > 2$. In this case the total number of electrons is larger than the maximal occupation of the conduction band (2 electrons per site). It means that it is impossible to get an empty f level, even if E_f is much higher in energy than the non-interacting conduction band ($E_f \gg D$), so the minimum value for n_f is $n_{tot}-2$. Moreover, the Fermi level does not cross the hybridization gap as discussed in the last subsubsection.

In Figure 4.6 the valence is shown for $n_{tot} = 2.5$ and $V = 0.1D$. The yellow region on the top right of the figure corresponds to the minimum value for $n_f(0.5)$. Note that the crossover region and the first-order critical line are now obtained for bigger values of E_f. Despite these differences, the generic shape of the phase diagram is the same as before.

In the region with $n_f = 0.5$, the chemical potential is pinned in the f peak of the density of states, as it happens in the intermediate valence region. However, since the conduction band is completely filled, the f peak and the hybridization gap are located close to the upper band edge.

Hybridization effects

Next, let us investigate the behavior of the E_f-U_{fc} phase diagram for different values of hybridization V. In Figure 4.7 the valence phase diagram is shown for $V = 0.01D$ (left) and $V = 0.5D$ (right) with a fixed $n_{tot} = 1.5$, in a comparison to the diagram presented in Fig. 4.1 ($V = 0.1D$). A bigger hybridization enlarges the width of the f peak, resulting in a smoother variation of valence. Consequently the position of the critical endpoint is pushed to a larger U_{fc} value and the valence crossover happens in a wider range of E_f values. The inverse situation is observed for smaller values of V (with respect to $V = 0.1D$), but the variations are less marked.

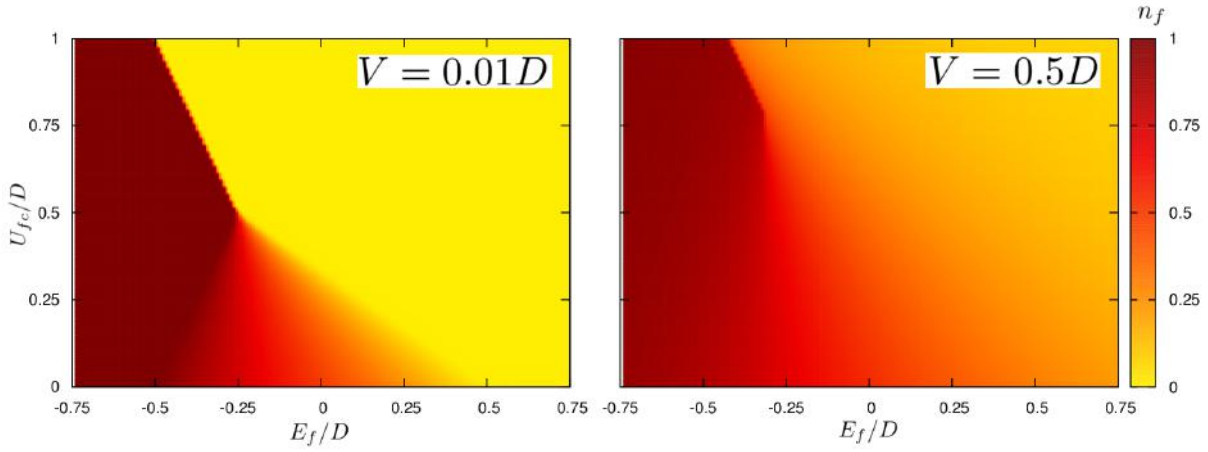

Figure 4.7: Valence phase diagram as in Fig. 4.1 for two distinct hybridizations: $V = 0.01D$ (left) and $V = 0.5D$ (right). The crossover region grows as V increases and the critical point moves to larger U_{fc} values.

Temperature effects

In the last sections we saw the behavior of the valence transitions at zero temperature. One important question is how the temperature changes the picture shown above. To investigate this point we carried out the same calculations at finite temperature. The electronic occupations now are no longer analytically integrable functions, since the temperature enters in the calculation through the Fermi distribution.

In Figure 4.8 the occupation n_f is plotted as a function of E_f for different temperatures and all the other parameters are kept fixed (see caption). The valence variation becomes smoother when the temperature is raised and the charge susceptibility (not shown) is reduced. A significant change occurs only for $T > 0.05D$, which implies that temperature does not play a major role in the valence transitions in our model. Considering the typical bandwidth of intermetallic lanthanides $D = 1eV$, the temperature scale at which thermal fluctuations modify the valence is roughly above room temperature.

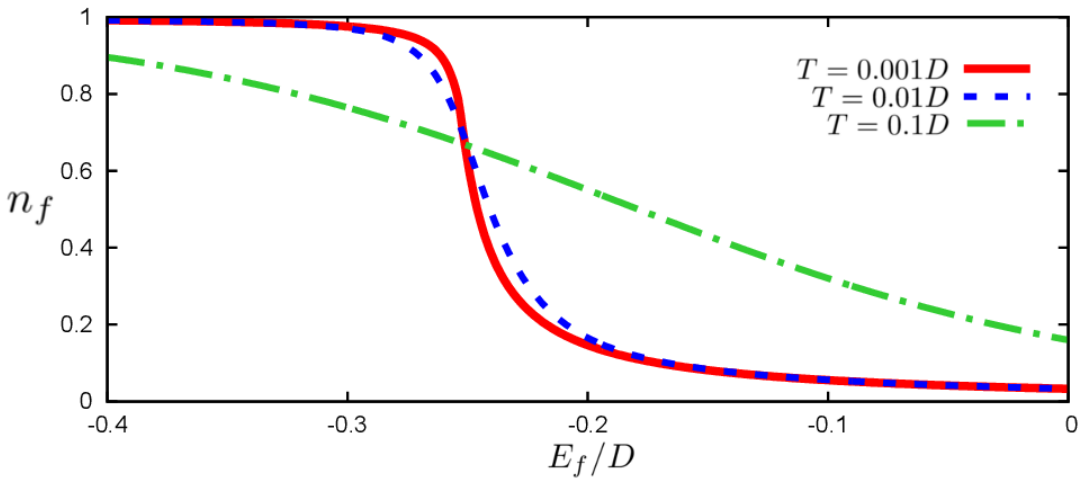

Figure 4.8: Valence variation as a function of E_f for three different temperatures: $T = 0.001D$ (red), $T = 0.01D$ (blue) and $T = 0.1D$ (green).The weak temperature dependence of the valence for $T < 0.05D$ excludes major temperature effects on the valence variations studied here. Other parameters are n_{tot}, $V = 0.1D$ and $U_{fc} = 0.5D$ and they are chosen to be close to the critical point from the crossover side of the phase diagram.

4.1.3 Summary

In this section the self-consistent equations for the Extended Periodic Anderson model within the approximations derived in Chapter 3, are solved numerically. The main result is contained in Figure 4.1, showing how the f level occupation n_f (the *valence*) depends on the model parameters at zero temperature. A finite Falicov-Kimball interaction U_{fc} is required to drive the valence transition discontinuous. The first-order valence transition line ends at a quantum critical point (for $U_{fc} = U^*_{fc}$) and it corresponds to a divergence in the charge susceptibility

$\chi_{ch} = -\partial n_f/\partial E_f$. For $U_{fc} < U^*_{fc}$ the valence variation is a continuous crossover, strongly enhanced close to the critical point.

4.2 Magnetic Phases

In Section 4.1 we analyzed the system in a nonmagnetic state where the pressure and the temperature are the only external parameters used to modify the valence in lanthanide ions. However the valence state $n_f = 1$ corresponds to a magnetic configurations with large effective magnetic moments (since $J = 7/2$ or $J = 5/2$), one would expect that the magnetic measurements in these systems could bring interesting information about the valence states.

In what follows the magnetic phases of the Extended Periodic Anderson model will be studied. The discussions start with the possibility of having intrinsic magnetism in the model, corresponding to spontaneous magnetization in the absence of magnetic field. Later we will discuss the magnetic solutions restricted to two different types of magnetic effects: the presence of an external magnetic field and ferromagnetism.

4.2.1 Intrinsic Magnetism

One relevant physical observable is the magnetic susceptibility at zero field. This quantity is formally defined as:

$$\chi_{mag} = \left.\frac{\partial m_f}{\partial h_{ext}}\right|_{h_{ext}\to 0^+} \tag{4.6}$$

Here m_f is the f-electron magnetization $m_f = n_{f,\uparrow} - n_{f,\downarrow}$ and h_{ext} is a small magnetic field applied to the system. As the charge susceptibility, χ_{mag} is here a function of all the parameters of the system.

We present below two ways to calculate χ_{mag} from the self-consistent equations. The first one is to include a infinitesimal magnetic field h_{ext} in the model through a Zeeman term,

$$\mathcal{H}_Z = -h_{ext} \sum_i g_f S^z_i, \tag{4.7}$$

and analytically expand m_f with respect to h_{ext}. It results directly in a formal expression for χ_{mag} in terms of the self-consistent parameters calculated before. For practical purposes, this calculation is shown in the Appendix B and only the main results will be presented here. In the second method the limit $h_{ext} \to 0$ is performed by numerical means using the calculations that will be presented in Section 4.2.2.

First Method

From the expansions carried on in Appendix B, it is seen that the generic form of the magnetic suscetibility (Eqs.B.10 and B.16) is given by:

$$\chi_0 = \frac{C_0}{1 - C_1} \tag{4.8}$$

The exact expressions for the coefficients C_0 and C_1 are shown in Appendix B. They are calculated, for a given set of model parameters, from the self-consistent solutions in the non-magnetic case discussed in Section 4.1.

A magnetic transition is expected when the magnetic susceptibility diverges. Since C_0 is a positive finite quantity, it implies that the condition to enter in a magnetic phase is $C_1 = 1$, which is a kind of Stoner criterion. An unphysical $\chi_0 < 0$ is obtained inside the ferromagnetic phase, when $C_1 > 1$, indicating that the ground state is ferromagnetic if $C_1 > 1$.

In Figure 4.9 we plot the value of $1 - C_1$ as a function of E_f for three different U_{fc} values: 0, $0.4D$ and $0.6D$ (keeping $V = 0.1D$ and $n_{tot} = 1.5$). The intrinsic ferromagnetism exists for the intervals in which $1 - C_1$ is negative. For $U_{fc} = 0$ it corresponds to $-0.3 < E_f < -0.17$. The magnetic region shrinks by increasing U_{fc} to $U_{fc} = 0.4D$, ranging from -0.27 to -0.25, and disappears when U_{fc} is larger than the critical value U^*_{fc}. So we conclude that the ferromagnetic instability occurs inside the crossover region of the valence transitions only.

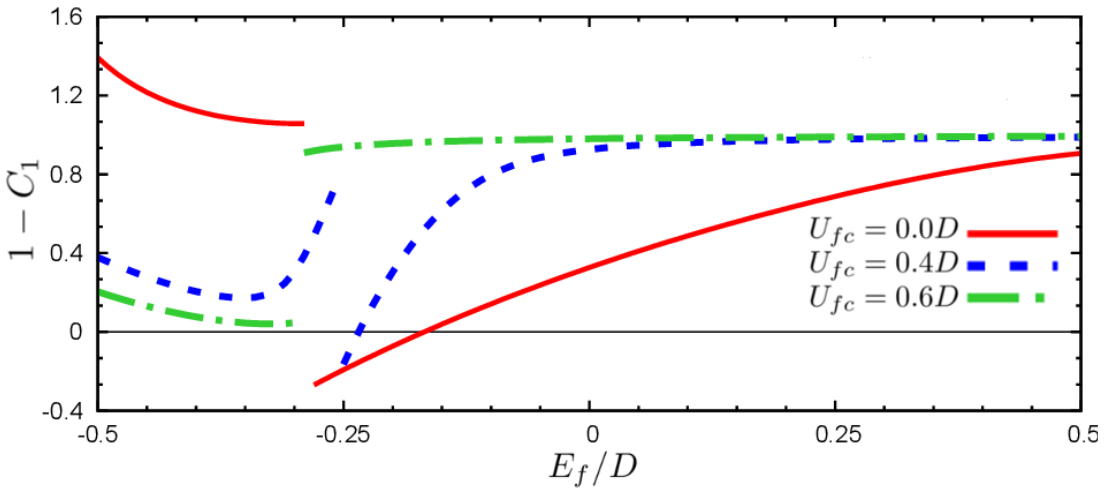

Figure 4.9: Value of $1 - C_1$ as a function of E_f for three different values of U_{fc}: 0,0.4 and 0.6. Other parameters are $V = 0.1D$ and $n_{tot} = 1.5$. The spontaneous ferromagnetism exists in the region where $1 - C_1 < 0$ as discussed in the text. The instability occurs only in the crossover regime ($U_{fc} < U^*_{fc}$) and its region size decreases with increasing U_{fc}. The jumps in the curves occur when the chemical potential jumps from one band to the other.

Another notable aspect of the intrinsic ferromagnetism is the dependence of its region size and position with respect to the occupation number n_{tot}. In Figure 4.10 the ferromagnetic region (its range in terms of E_f) is plotted for different values of n_{tot} between 1 and 2, having fixed $U_{fc} = 0$ and all the other parameters as in Figure 4.9. The ferromagnetic region exists only for $n_{tot} < 1.7$ and it becomes wider by decreasing n_{tot}. When $n_{tot} \to 1$ the region extends to a very large range of negative E_f values, which is visually indicated close to the horizontal axis.

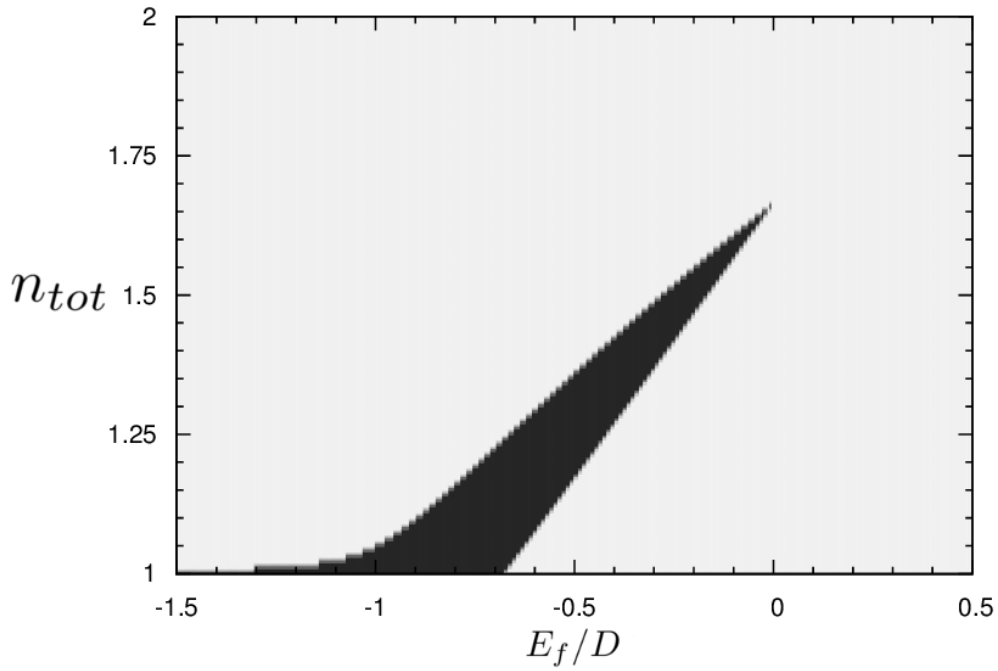

Figure 4.10: Ferromagnetic region (in black) as a function of E_f and n_{tot}. For n_{tot} values larger than 1.7 the magnetic instability does not exist. As n_{tot} approaches 1, the region broadens. Other parameters: $V=0.1D$ and $U_{fc}=0$.

Second Method

A second method to determine magnetic instabilities is to look for magnetic solutions in the self-consistent calculations in the absence of a magnetic field or coupling. In this case m_f is another self-consistent parameter that must be computed together with n_f and μ, which will be explained in details in the Subsection 4.2.2. Both methods are equivalent as long as $\chi_{mag}>0$, i.e. outside the ferromagnetic phase.

The zero field magnetic susceptibility at $T=0$ obtained by the numerical method is shown in Figure 4.11. In this map we see two regions where the magnetic susceptibility is very large. The biggest values are situated in the integer valence $n_f=1$ regime. In this region χ_{mag} is large because the f-level is easily polarizable if it lies well below the chemical potential. The numerical values obtained from the extrapolation of finite magnetic fields are larger than those calculated from expressions B.16, which might be a numerical error related to band edge effects. Nevertheless, it is important to recall that this region would be dominated by the Kondo physics and other magnetic instabilities (from RKKY interactions) which are expected in this region, but not described in our model.

The second region is less trivial. It is a narrow area inside the intermediate valence regime and it is directly connected to the valence transition. The magnetic susceptibility at low temperatures is proportional to the density of states at the Fermi level (Eq.B.13). For our model this quantity is large when the chemical potential is close to E_f, which corresponds

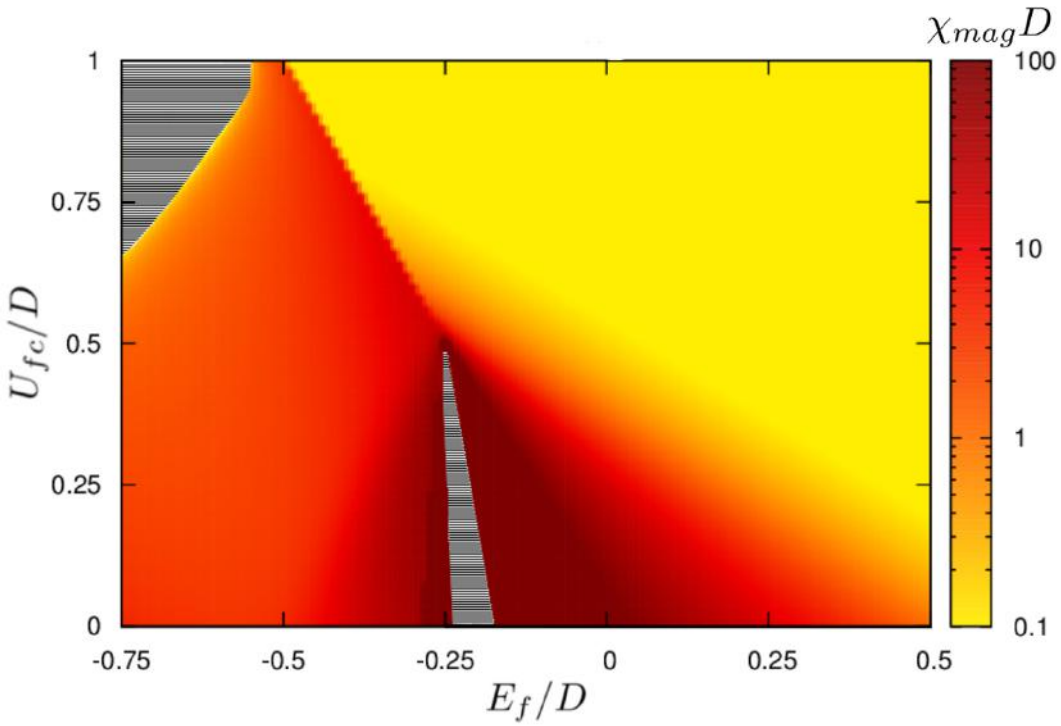

Figure 4.11: Magnetic susceptibility as a function of E_f and U_fc for $V=0.1D$ and $n_{tot}=1.5$. A ferromagnetic transition exists inside the intermediate valence region around $E_f=-0.25D$, corresponding to the situation in which the f part of the density of states is enhanced (close to the hybridization gap).

exactly to the situation with large valence variations in the crossover regime. The calculations shown in Appendix B yield negative values for χ_0 in this region, signaling a ferromagnetic instability, which was not obtained by the numerical method.

One interesting question is whether there is a ferromagnetic instability in this model at zero temperature. It is well-known for the Hubbard model that the ground state is not ferromagnetic in the zero bandwidth limit [69]. Moreover, Hubbard-I approximation *does not* lead to any ferromagnetic instability for a rectangular density of states[3]. Then the Coulomb repulsion by itself does not seem to be the driving mechanism leading to instabilities.

In Periodic Anderson model the situation is more complex. Apart from the possible ferromagnetic states in the localized limit due to RKKY interactions, instabilities are also observed in the intermediate valence regime. For instance, Reddy and collaborators [76] shown that ferromagnetism is expected in this regime, depending on the position of f level and the total number of electrons. Hybridization is the key mechanism for ferromagnetism, once it slightly delocalizes the f levels and it generates strongly asymmetric density of states. Remarkably they have found ferromagnetism around $E_f=-0.25D$ for the same parameters as in Figure 4.11, advocating in favor of a ferromagnetic instability inside the intermediate valence region of our

[3]For further details, check Section 8.5 of Ref. [75]

diagram.

4.2.2 Magnetism induced by an external magnetic field

Let us consider an additional static and homogeneous external magnetic field H_{ext} applied to the system described by the EPAM (Eq. 3.1). The magnetic field is assumed to be along the z axis, which is chosen as the quantization axis for the spin operators. It couples to the electrons through the Zeeman interaction[77]:

$$\mathcal{H}_Z = -h_{ext} \sum_i \left(g_f S_i^z + g_c s_i^z \right) \tag{4.9}$$

In Equation 4.9, the f and c electron spin operators are denoted by S_i^z and s_i^z, respectively. The constants g_f and g_c include their Bohr magneton and the Landé factors in a shorthand notation.

According to Table 2.1, the magnetic configurations of the lanthanides carry large magnetic moments as a consequence of Hund's rules. Furthermore, in the intermediate valence regime of EPAM the f and c contributions for the density of states obey the relation $\rho^{ff}(\mu) \gg \rho^{cc}(\mu)$. For those reasons, we will neglect from now on the conduction electrons magnetization by assuming $g_f \gg g_c$. Since we consider a non-degenerate f-level, we assume also $S_i = 1/2$. Using the fermionic representation of the spin operator S_i^z,

$$S_i^z = \frac{f_{i\uparrow}^\dagger f_{i\uparrow} - f_{i\downarrow}^\dagger f_{i\downarrow}}{2}, \tag{4.10}$$

we can write the EPAM hamiltonian in a presence of an external magnetic field:

$$\mathcal{H} = -\sum_{ij\sigma} t_{ij} c_{i\sigma}^\dagger c_{j\sigma} + E_f \sum_{i\sigma} f_{i\sigma}^\dagger f_{i\sigma} + \frac{U_{ff}}{2} \sum_{i\sigma} \hat{n}_{i\bar{\sigma}}^f \hat{n}_{i\sigma}^f + V \sum_{i\sigma} \left(c_{i\sigma}^\dagger f_{i\sigma} + f_{i\sigma}^\dagger c_{i\sigma} \right) + U_{fc} \sum_{i\sigma\sigma'} \hat{n}_{i\sigma}^f \hat{n}_{i\sigma'}^c - \frac{g_f}{2} h_{ext} \sum_{i\sigma} \sigma f_{i\sigma}^\dagger f_{i\sigma} \tag{4.11}$$

The mean-field approximation developed for the U_{fc} term in Section 3.3.1 is not affected by the presence of the new term in the hamiltonian. So, if this approximation is explicitly taken in the model hamiltonian, it yields:

$$\mathcal{H} = -\sum_{ij\sigma} t_{ij} c_{i\sigma}^\dagger c_{j\sigma} + U_{fc} n_f \sum_{i\sigma} \hat{n}_{i\sigma}^c + \sum_{i\sigma} \widetilde{\varepsilon}_{f,\sigma} f_{i\sigma}^\dagger f_{i\sigma} + \frac{U_{ff}}{2} \sum_{i\sigma} \hat{n}_{i\bar{\sigma}}^f \hat{n}_{i\sigma}^f + V \sum_{i\sigma} \left(c_{i\sigma}^\dagger f_{i\sigma} + f_{i\sigma}^\dagger c_{i\sigma} \right) \tag{4.12}$$

Here we have defined:

$$\widetilde{\varepsilon}_{f,\sigma} = E_f + U_{fc} n_c - \frac{g_f h_{ext} \sigma}{2} \tag{4.13}$$

The next step is to deal with the Couloumb repulsion U_{ff} employing again the Hubbard-I approximation. The equations presented in Section 3.3.3 must be modified because the magnetic field lifts the degeneracy of the two spin projections. In particular, the coefficient p involved in Eq. 3.14 is now spin-dependent. Here I recall its definition:

$$p_\sigma = 1 - n_{f\overline{\sigma}} \tag{4.14}$$

Following the same steps that lead to Equations 3.24 and 3.25, we can write the Green's functions for f and c electrons:

$$G^{cc}_\sigma(\mathbf{k},\omega) = \frac{1}{\omega - \widetilde{\varepsilon}_c(\mathbf{k}) - \frac{p_\sigma V^2}{\omega - \widetilde{\varepsilon}_{f\sigma}}} \tag{4.15}$$

$$G^{ff}_\sigma(\mathbf{k},\omega) = \frac{p_\sigma}{\omega - \widetilde{\varepsilon}_{f\sigma} - \frac{p_\sigma V^2}{\omega - \widetilde{\varepsilon}_c(\mathbf{k})}} \tag{4.16}$$

Each spin component will have its own quasiparticle spectrum and density of states, corresponding to different positions of the effective f level (Eq. 4.13) and different renormalizations (p_σ) of the hybridization parameter. The energy spectrum is now given by:

$$\omega_{\pm,\sigma} = \frac{\widetilde{\varepsilon}_c(\mathbf{k}) + \widetilde{\varepsilon}_{f\sigma}}{2} \pm \sqrt{\left(\frac{\widetilde{\varepsilon}_c(\mathbf{k}) - \widetilde{\varepsilon}_{f\sigma}}{2}\right)^2 + p_\sigma V^2} \tag{4.17}$$

Using a constant density of states for the non-interacting density of states $\rho_0(\omega)$, one can obtain the partial density of states $\rho^{cc}_\sigma(\omega)$ and $\rho^{ff}_\sigma(\omega)$ by the transformation applied in Section 3.4. These functions are nonzero for two disconnected regions separated by an hybridization gap, being the edges also spin-dependent.

The expressions for the partial density of states for the c and f electrons are:

$$\rho^{cc}_\sigma(\omega) = \frac{1}{2D} \tag{4.18}$$

and

$$\rho^{ff}_\sigma(\omega) = \frac{1}{2D}\frac{p^2_\sigma V^2}{(\omega - \widetilde{\varepsilon}_{f\sigma})^2}, \tag{4.19}$$

both defined in the energy regions corresponding to Eq.4.17 evaluated in the band edges, in analogy to Eqs.3.38-3.41.

A schematic representation (for arbitrary parameters) of the total density of states $\rho^{tot}_\sigma(\omega) = \rho^{cc}_\sigma(\omega) + \rho^{ff}_\sigma(\omega)$ is depicted in Figure 4.12. The Zeeman interaction modifies the position of edges and the renormalization of the spectral weight of the f peak. The spin dependence of the hybridization gap width reflects the fact that the parameter V^2 is renormalized by p_σ in our approximation and it is larger for the majority spin orientation.

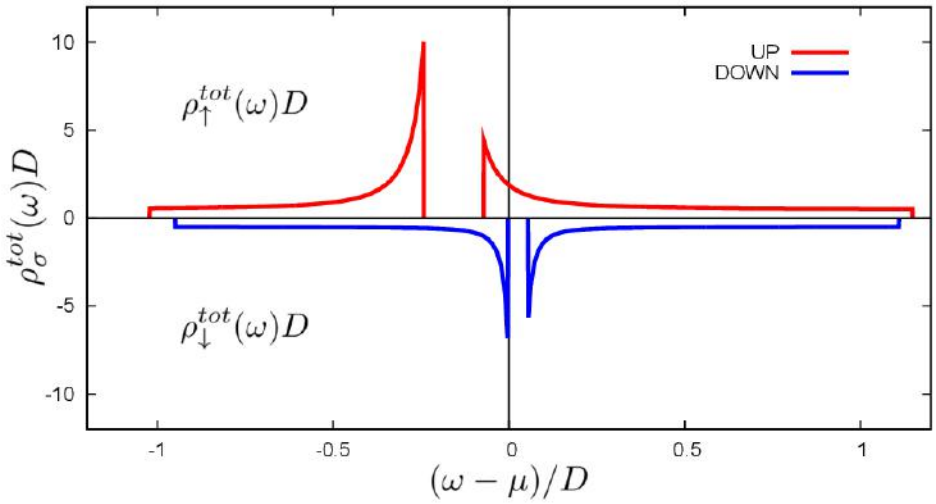

Figure 4.12: Total density of states $\rho_{\sigma}^{tot}(\omega) = \rho_{\sigma}^{cc}(\omega) + \rho_{\sigma}^{ff}(\omega)$ for each spin direction. Note that all the features in $\rho_{\sigma}^{tot}(\omega)$ are spin-dependent: the with of hybridization gap, the band edges and the height of the f peak. The parameters are chosen to exaggerate the difference between the spin bands.

Results

The self-consistent equations for the magnetization, valence and chemical potential are solved numerically using the same method as in Section 4.1. For simplicity, we define $g_f = 2$ as the numerical value for the g-factor.

In Figure 4.13 we show the valence and the magnetization of the f electrons as a function of h_{ext}. Three points in the E_f-U_{fc} phase diagram are considered: $E_f = -0.15D; U_{fc} = 0.4D$ (Point A, solid red line), $E_f = -0.2D; U_{fc} = 0.5D$ (point B, blue dashed line) and $E_f = -0.25D; U_{fc} = 0.6D$ (point C, green dot-dashed line). The other parameters are kept fixed: $V = 0.1D$ and $n_{tot} = 1.5$. Their positions in the E_f-U_{fc} phase diagram (for $h_{ext} = 0$) are shown on the inset. The magnetic field leads always to an increase of both valence and magnetization, or in other words, it always drives the system towards a more localized behavior.

When the system is in the crossover region (curves A and B), both parameters n_f and m_f vary continuously with the external field. For an U_{fc} larger than the critical value, a first-order valence transition appears by the effect of the external field and it is accompanied by a magnetization jump in a critical field (curve C). Above the transition the magnetization is close to its saturated value, in which $m_f/n_f = 1$. The critical field h_{ext}^* reflects the distance (in terms of E_f) from the valence critical line. For instance, when $U_{fc} = 0.6D$ and $E_f = -0.25D$ (curve C) the critical field is $h_{ext}^* = 0.05D$, which is exactly the difference between E_f and the critical $E_f = -0.3D$ for $U_{fc} = 0.6D$.

The increase of valence with a magnetic field can be understood conceptually from simple arguments. The external magnetic field acts in detriment of the spin degeneracy of the f-level, which acquires a polarization energy proportional to h_{ext} (see the band splitting in Figure 4.12).

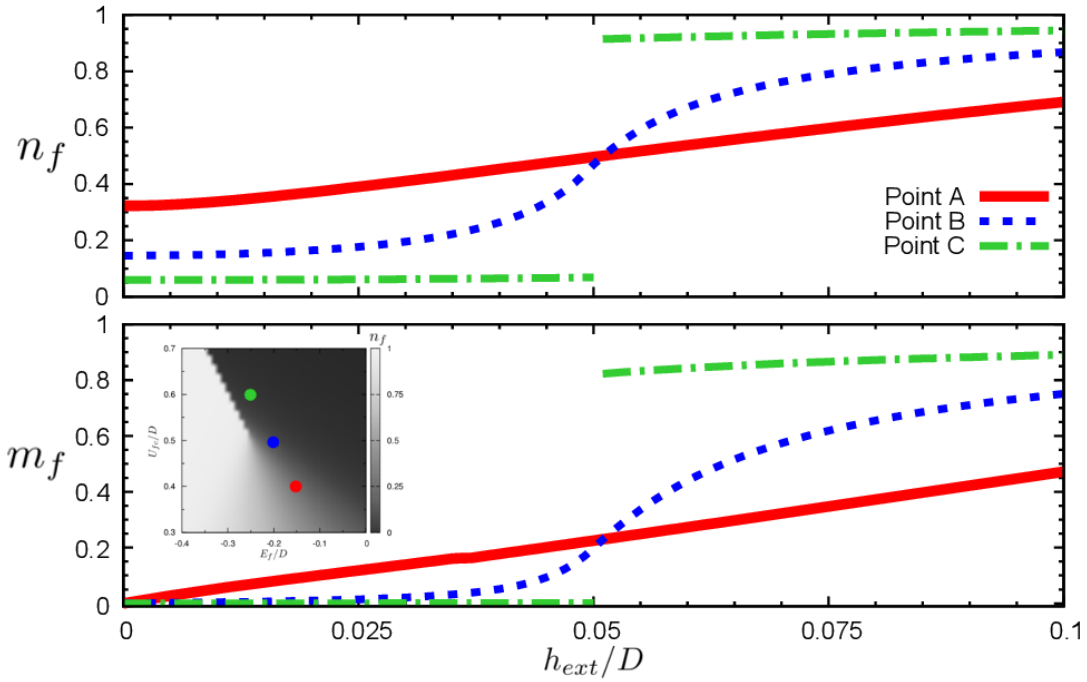

Figure 4.13: Valence n_f (top) and f-electron magnetization m_f(bottom) as a function of the external magnetic field h_{ext} for three points in the E_f-U_{fc} phase diagram: $E_f=-0.15D; U_{fc}=0.4D$(point A), $E_f=-0.2D; U_{fc}=0.5D$ (point B) and $E_f=-0.25D; U_{fc}=0.6D$ (point C). Other parameters are $V=0.1D$ and $n_{tot}=1.5$. **Inset:** position of the three set of parameters with respect to the E_f-U_{fc} phase diagram (Fig. 4.1).

Then one of the spin components (here the positive $S_z=+1/2$) has an effective f-level position that decreases progressively with respect to E_f (Eq. 4.13), while for the other component it increases. This separation is associated to a larger occupation of the up-spin component, increasing the f-electron magnetization and the valence.

Next let us see how the magnetic field affects the dependence of n_f and m_f on the position of the f-level E_f in the crossover and the first-order valence transition regions. This will be important for discussions on the pressure dependence of mixed-valence compounds under a magnetic field. This dependence is shown in Figure 4.14 in the crossover(left) and first-order (right) regions for three values of h_{ext}: $h_{ext}=0.01D$ (red solid line), $h_{ext}=0.1D$ (blue dashed line) and $h_{ext}=0.5D$ (green dot-dashed line). In both cases the external magnetic field leads the valence variation region towards larger values of E_f. The displacement with respect to the case without external field is given by h_{ext} itself, in agreement with the arguments given in the last paragraph. We remark, based on these results, that the external field is unable to change the nature of the valence transition, i.e. it does not transform the valence crossover into a discontinuous transition. The magnetization curves in Figure 4.14 for $h_{ext}=0.1D$ and $h_{ext}=0.5D$ present some kinks as a function of E_f, which are caused by the chemical potential crossing the hybridization gap for one or both spin orientations (see Figure 4.12).

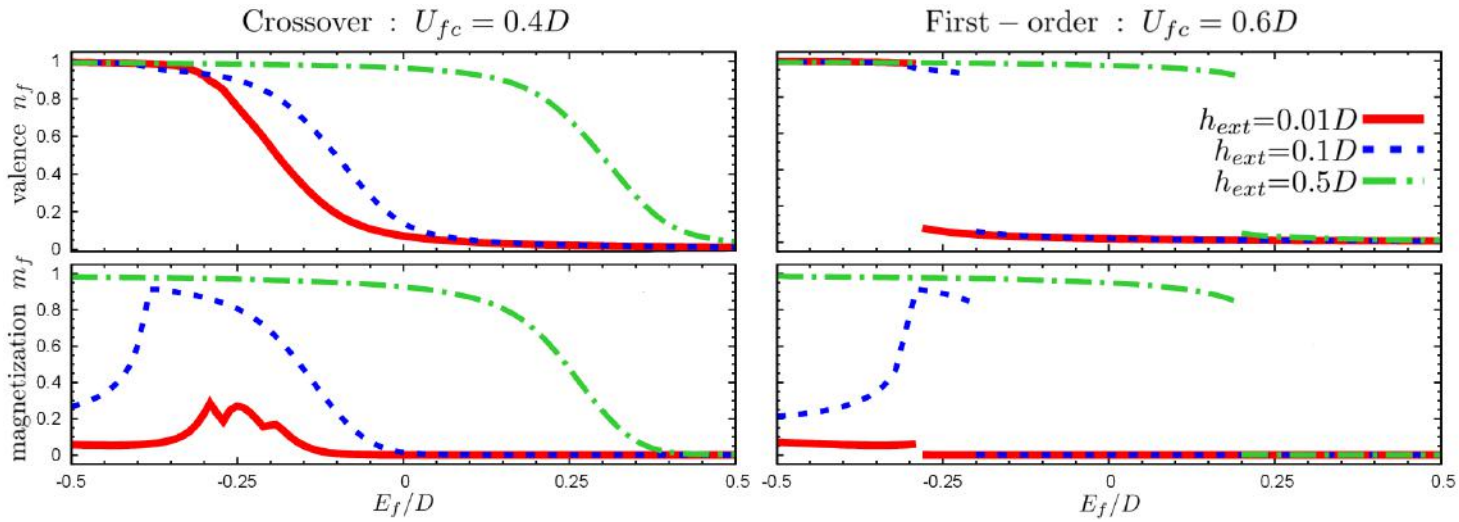

Figure 4.14: Valence n_f (top) and f-electron magnetization m_f(bottom) as a function of E_f in the crossover region $U_{fc} = 0.4$. Three values of h_{ext} are considered: $h_{ext} = 0.01D$ (red solid line), $h_{ext} = 0.1D$ (blue dashed line) and $h_{ext} = 0.5D$ (green dot-dashed line). Other parameters are $V = 0.1$ and $n_{tot} = 1.5$. The external field pushes the valence transition region to larger E_f values and the displacement is roughly given by h_{ext}, but it *does not change* the transition character. The magnetization at small field is large only close to the unstable region discussed in Figure 4.9, but it spreads out when the field increases.

Conclusion

In Section 4.2.2 we have shown the effect of an external magnetic field h_{ext} in the EPAM through the addition of a Zeeman interaction in the f electrons. Such interaction lifts the model spin-degeneracy, which leads to different densities of states for the two spin components (Figure 4.12). In summary, the application of h_{ext} always increases the valence n_f and the magnetization m_f, but the type of variation (i.e. whether it is continuous or not) depends on the value of U_{fc}. For $U_{fc} > U^*_{fc}$ the field-induced valence transition is discontinuous, being U^*_{fc} the same critical value as in the non-magnetic case (Section 4.1).

4.2.3 Ferromagnetism induced by f-f exchange

In the preceding sections we have not considered the presence of RKKY interaction in the system. In this section such f-f exchange interaction will be added to the EPAM, considering the exchange interaction J_{ij} as a parameter.

Ferromagnetic Interactions and Mean-Field approximation

Here we will restrict ourselves to the analysis of nearest neighbor ferromagnetic interactions, described by the following hamiltonian:

$$\mathcal{H}_J = -J \sum_{<i,j>} \mathbf{S}_i \cdot \mathbf{S}_j \tag{4.20}$$

In this hamiltonian $< i, j >$ represents the sum over all pairs of neighboring sites in the lattice and J is the strength of magnetic interaction ($J > 0$ for ferromagnetism). This term will be treated in mean-field approximation. The spin operators are replaced by their average values plus fluctuations, that are kept to first order only. If the magnetization is along the z axis, then:

$$S_i^z S_j^z \approx \langle S_i^z \rangle S_j^z + \langle S_j^z \rangle S_i^z - \langle S_i^z \rangle \langle S_j^z \rangle \tag{4.21}$$

In the ferromagnetic state the system is homogeneous and the average value $\langle S_i^z \rangle$ is the same for all lattice sites. Using this invariance explicitly in the mean-field approximation, the hamiltonian in Eq. 4.20 yields:

$$\mathcal{H}_J = -Jm_f \sum_{i\sigma} \sigma f_{i\sigma}^\dagger f_{i\sigma} + Jm_f^2 N \tag{4.22}$$

Here the spin operator is rewritten in terms of fermionic operators $S_i^z = 1/2(f_{i\uparrow}^\dagger f_{i\uparrow} - f_{i\downarrow}^\dagger f_{i\downarrow})$, we used the definition $m_f = 2 < S^z >$ and N is the number of lattice sites. The prefactor in the sum (Jm_f) is named Weiss molecular field once it acts in the same way as an external magnetic field (as in Eq. 4.9), apart from the constant $Jm_f^2 N$. For this reason, we can use the same equations as in Section 4.2.2 to calculate n_f and m_f, but now m_f must be computed self-consistently since it is proportional to the Weiss field. Moreover, the trivial solution $m_f = 0$ is always present in this case, so it is crucial to compare its energy to other self-consistent solutions. The expression for the total energy in the presence of the f-f magnetic exchange is:

$$\frac{E_{tot}}{N} = \sum_\sigma \int_{-\infty}^{\mu} d\omega \omega \left(\rho_\sigma^{cc}(\omega) + \rho_\sigma^{ff}(\omega) \right) - U_{fc} n_c n_f + Jm_f^2, \tag{4.23}$$

Results

Let us present the numerical results that we have obtained in the presence of a ferromagnetic exchange. The bisection method was employed again and the good solution is chosen among the self-consistent results by energy comparison. The valence and magnetization dependence on the exchange parameter J is shown in the Figure 4.15 for three different points in the E_f-U_{fc} phase diagram: $E_f = -0.15D; U_{fc} = 0.4D$ (point A), $E_f = -0.2D; U_{fc} = 0.5D$ (point B) and $E_f = -0.25D; U_{fc} = 0.6D$ (point C). These points are chosen to be close to the critical point (see Figure 4.1) and are the same of Fig. 4.13. Differently from the case of an external magnetic field (Figure 4.13), the increase of J always leads to a discontinuity in the valence and the magnetization, irrespective to the value of U_{fc}. For the points A and B the magnetization

jumps are smaller than in point C and m_f does not reach its maximum value after it. For the point C the magnetization jump happens at $J=0.31D$ and m_f is close to the saturation for $J>0.31D$ (where the three curves superimpose).

Next we analyze the variations of n_f and m_f as a function of E_f in Figure 4.16, following the same lines as in Section 4.2.2. The results are shown for $U_{fc}=0.4D$ (left) and $U_{fc}=0.6D$ (right), which are also classified as crossover and first-order scenarios in terms of the critical U_{fc} value for the paramagnetic phase diagram in Figure 4.1. Here the results are presented for two exchange values: $J=0.1D$ and $J=0.5$. For $U_{fc}=0.4D$, the magnetization is finite in the interval between $E_f=-0.4D$ and $E_f=-0.15D$ when $J=0.1D$. This region is placed around $E_f=-0.25D$, that corresponds to the ferromagnetic instability in the paramagnetic case (see Fig.4.9), widened by the additional exchange interaction. The $m_f\neq 0$ region can be further widened by increasing J or decreasing U_{fc}.

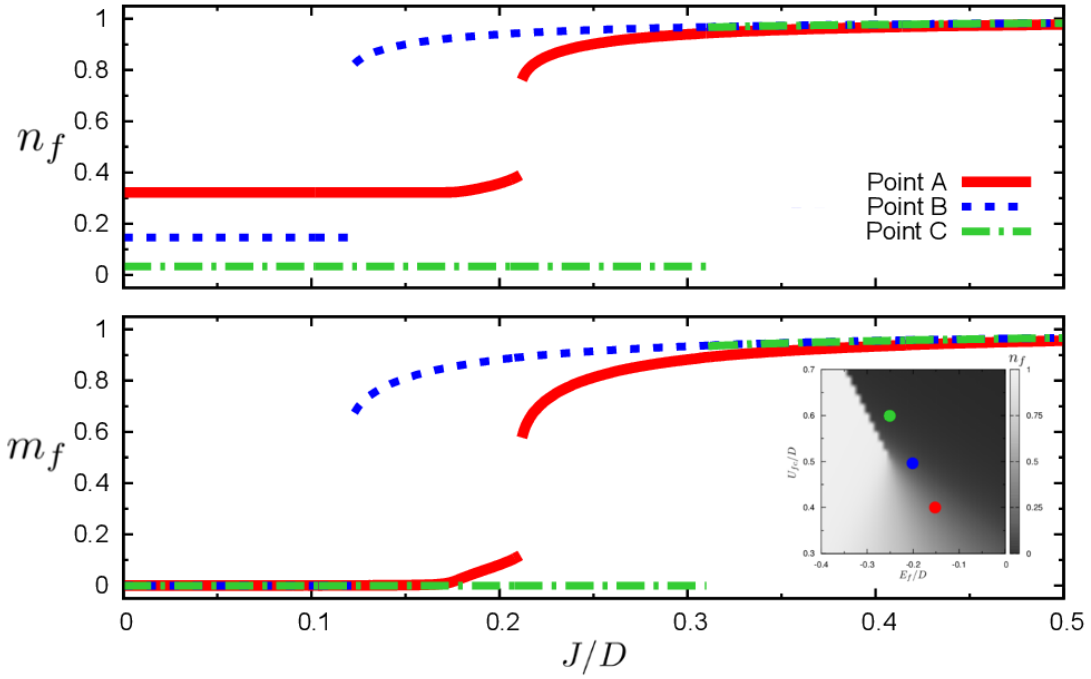

Figure 4.15: Valence n_f(top) and f-electron magnetization m_f(bottom) as a function of the exchange parameter J for three points in the E_f-U_{fc} phase diagram: $E_f=-0.15D; U_{fc}=0.4D$(point A), $E_f=-0.2D; U_{fc}=0.5D$ (point B) and $E_f=-0.25D; U_{fc}=0.6D$ (point C). Other parameters are $V=0.1D$ and $n_{tot}=1.5$. **Inset:** position of the three set of parameters with respect to the E_f-U_{fc} phase diagram (Fig. 4.1).

Conclusion

In Section 4.2.3 we considered the addition of a ferromagnetic exchange interaction between the f-electrons in the EPAM. Such interaction was treated in mean-field approximation, which yields the same equations as in Section 4.2.2 but in the presence of a self-consistent (Weiss)

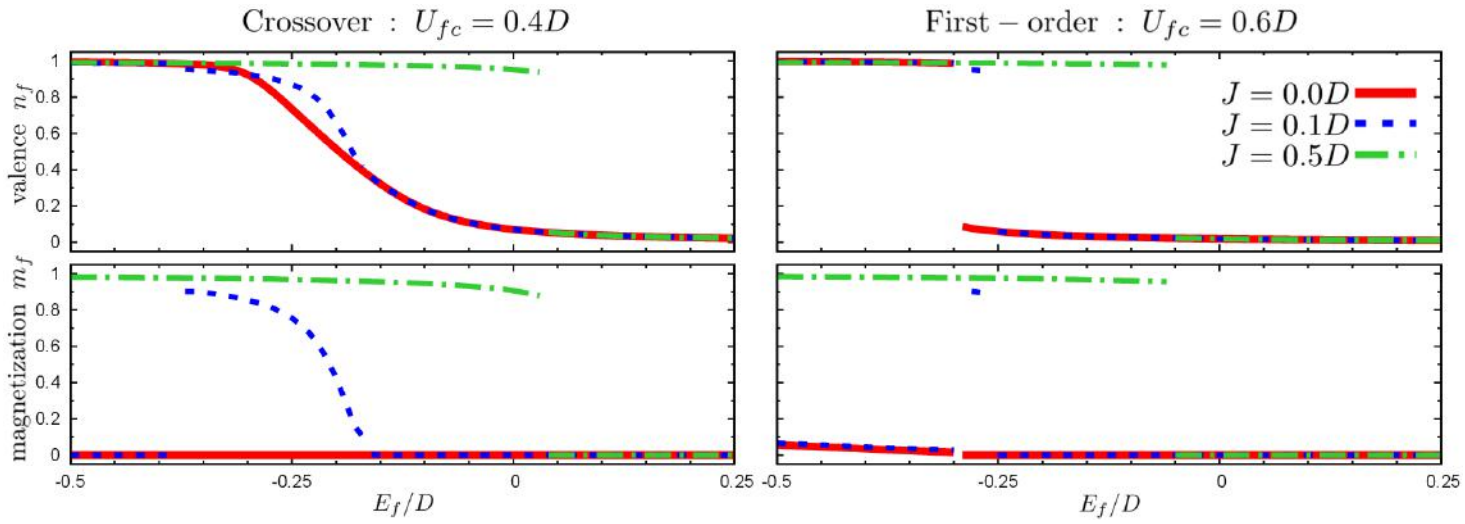

Figure 4.16: Valence n_f (**top**) and f-electron magnetization m_f(**bottom**) as a function of E_f in the crossover region $U_{fc} = 0.4$ (left) and in the first-order transition region $U_{fc} = 0.6$. Three values of J are considered:$J = 0$ (red solid line), $J = 0.1D$ (blue dashed line) and $J = 0.5D$ (green dot-dashed line). Other parameters are $V = 0.1$ and $n_{tot} = 1.5$.

magnetic field. The results are shown in Figures 4.15 and 4.16, representing the valence and magnetization as a function of J (for a fixed point in the E_f-U_{fc} phase diagram) and as a function of E_f (for fixed J and U_{fc}), respectively. As a general result, we have seen that the valence dependence on J is always a discontinuous curve, independent of the U_{fc} value. This is in contrast to the valence dependence on h_{ext} observed in last section, so we argue that ferromagnetism may enhance the valence transition. The discontinuities might also be an artifact of the mean-field approximation. In Figure 4.16 it is observed how the ferromagnetic unstable region presented in Section 4.2.1 is increased in the presence of the additional exchange interaction, as one should expect. These results will be revisited when the ferromagnetic transition of $YbCu_2Si_2$ will be discussed (Section 4.3.2).

4.2.4 Summary

In this section the role of magnetism in valence transitions was discussed through three different scenarios: the intrinsic magnetism provided by a ferromagnetic instability of the system, the magnetism induced by an external magnetic field and the magnetism provided by f-f exchange interactions. In the first case it was shown that a ferromagnetic instability exists in a small part of the intermediate valence region (Figure 4.11) as long as the electronic filling n_{tot} does not exceed a critical value, as indicated in Figure 4.10. The self-consistent magnetization obtained in the absence of fields can be as high as $m_f \approx 0.35$ inside this region. This instability can be explained by the means of the Stoner criterion, which predicts an instability when density of states in the Fermi level is sufficiently high, that happens in our model precisely when the

Fermi level crosses the hybridization gap.

In the second scenario an external magnetic field was included in the system by addition of a Zeeman interaction on the f-electrons. Since this interaction breaks the spin-symmetry, the self-consistent equations were modified to take it into account. The major result is the field dependence of the valence n_f and magnetization m_f: they both increase with an increasing h_{ext}, but the nature of these transitions (continuous or not) depends on the value of U_{fc} as in the non-magnetic case. A discontinuous valence transition is seen only if U_{fc} is larger than its critical value in the absence of fields (defined as U_{fc}^*). As a conclusion, the application of an external field could be a god tool to control experimentally valence variations, since it allows us to identify quantitatively the U_{fc} interaction for a given system.

In the last scenario we studied the effect of a ferromagnetic exchange interaction between f electrons in neighboring sites. The interaction was included in the mean-field level. The results show that the first-order transition is *enhanced* by the exchange interaction, since it drives the valence transition discontinuous for any value of U_{fc} interaction. Whether it is a consequence of the mean-field or not is still an open question, nevertheless the existence of intermetallic lanthanides that display first-order ferromagnetic transitions (for example $\mathrm{YbCu_2Si_2}$, discussed in the next section) may advocate in favor of it.

4.3 Connection with experiments

In this chapter we will establish some connections between the theory developed for the EPAM and some selected materials showing valence transitions. The choice of compounds is far from being exhaustive, still they were chosen carefully to make a point in every aspect discussed in the theoretical part: application of pressure and magnetic fields, ferromagnetism and the nature of the valence variations (crossover or first-order transition).

4.3.1 Pressure effects

Pressure reduces the system size, increasing the overlap between the wave-functions of conduction electrons and the 4f orbitals. In the case of Ce-based compounds the negative ions are pushed in the direction of the tails in the 4f wave-function, which produces an increase of E_f in our model[68]. The hybridization V and the inter-orbital repulsion U_{fc} also increase due to the larger overlap. As a consequence, pressure tends to favor the nonmagnetic valence configuration of cerium (Ce^{4+}, corresponding to $4f^0$) with respect to the magnetic configuration (Ce^{3+} or $4f^1$)

Ytterbium compounds are often seen as the "hole" analogous to cerium, once it has a $4f^{13}$ (one hole) configuration in its valence state Yb^{3+} in competition with the $Yb^{2+}(4f^{14})$ state. In this case pressure favours the magnetic state Yb^{3+}, which amounts to decreasing E_f and V in the Periodic Anderson model. The particle-hole analogy is useful to compare similar compounds (as in $\mathrm{CeCu_2Si_2}$ and $\mathrm{YbCu_2Si_2}$), although important differences exists between Ce-based and Yb-based materials[78].

As a practical rule, pressure favours larger valencies in lanthanides. For Ce and Yb it

corresponds to Ce^{4+} (nonmagnetic) and Yb^{3+} (magnetic). For europium, for which some examples will be discussed in this section, pressure *a priori* induces a transition from the magnetic divalent state (Eu^{2+}) to the nonmagnetic $J=0$ trivalent state (Eu^{3+}).

Recalling that volume effects are not explicitly considered in the model and the pressure is not a parameter in the model, it is clear that pressure effects must be encoded in terms of the other model parameters, such as E_f and V. For this purpose, some hypothesis on the relation between pressure and parameters are done.

First we assume that the pressure can be translated as a continuous and monotonic variation of the model parameters E_f, U_{fc} and V. In this case, we choose E_f as the control parameter and use its variation $\Delta E_f = E_f - E_f^0$ (with respect to the initial value E_f^0) to write the variation of U_{fc} and V:

$$U_{fc} = U_{fc}^0 + \alpha \Delta E_f \tag{4.24}$$

$$V = V^0 + \beta \Delta E_f \tag{4.25}$$

For comparison purposes, two different scenarios for the parameter variations are proposed. In both scenarios U_{fc} varies weakly with ΔE_f and we fix $\alpha = 0.1$. The difference comes from the hybridization dependence: in *scenario A* the hybridization is kept fixed at $V^0 = 0.1D$ ($\beta = 0$), while in **scenario B** V has a weak dependence on ΔE_f and $\beta = 0.1$. We consider two different values of U_{fc}^0 for each scenario, $U_{fc}^0 = 0.4D$ and $U_{fc}^0 = 0.6D$, in order to describe the crossover and the first-order valence transition regions, respectively.

In Figure 4.17 the valence dependence on pressure is schematically shown for the two scenarios proposed above. For both scenarios the crossover and the first-order valence transitions are shown in the red and blue curves, respectively, and corresponds to different values of U_{fc}^0 as indicated. The inset of Fig.4.17 presents schematically the parametrized curves with respect to the phase diagram in Figure 4.1(with a fixed $V = 0.1$).

The situation described by scenario A is qualitatively the same as in Figure 4.1.On the other hand, if the hybridization dependence on pressure is included (bottom figure), the valence variation is strongly reduced. In this case a discontinuous transition still exists, however the valence jumps is smaller than for a fixed V. This picture is more consistent with the experimental results showing that valence variations are small (on the order of 0.1) even if the transition is discontinuous.

4.3.2 $YbCu_2Si_2$

The first Yb-based compound of interest is $YbCu_2Si_2$[38, 79]. It has a tetragonal crystal structure with lattice parameters $a = 3.92$ Åand $c = 9.99$ Å. The Sommerfeld parameter around $\gamma \approx 150 mJ/mol.K^2$ evidences a moderate heavy-fermion character established below 40K.

This material was meticulously studied in Ref. [38], where a substantial set of experimental results under extreme conditions and their respective analysis were performed. Some of these results will be summarized and their connection with the theory developed in this part of the thesis will be debated.

Figure 4.18 shows the P-T phase diagram of $YbCu_2Si_2$ with emphasis on the valence values. The highlighted feature of this diagram is a ferromagnetic transition at $p = 8GPa$ with ordering

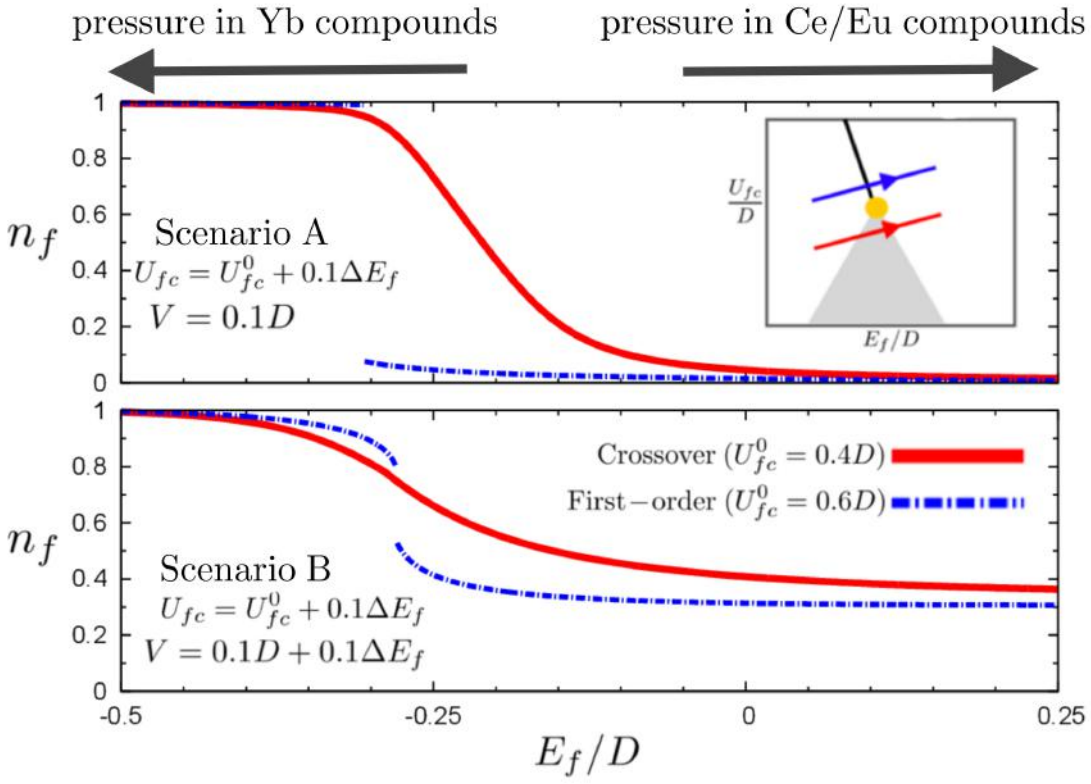

Figure 4.17: Pressure effects on the valence when passing through the crossover (red) or the first order transition line (blue), as indicated on the inset. On the top the hybridization is kept fixed with the increasing pressure (*scenario A*), while on the bottom V increases linearly with it (*scenario B*).

temperature $T_M = 8K$[79] and it is believed to have a first-order nature, which contrast to the second-order antiferromagnetic critical point from the Doniach diagram (Fig.1.2) and often seen in Ce compounds. For the temperature of 7K (below T_M), the Yb valence varies linearly with the pressure, from 2.75 at ambient pressure to 2.92 at $p = 15GPa$[80].

The appearance of a pressure-induced ferromagnetic transition with an increasing valence is also observed in our model. $\mathrm{YbCu_2Si_2}$ does not show any evidence of discontinuous valence transitions, then it should be placed in the crossover region of the phase diagram in Figure 4.1. It has an intermediate valence $Yb^{2.75+}$ at room pressure that goes towards the magnetic configuration Yb^{3+} under pressure, as expected for Yb compounds (see Figure 4.17). What is remarkable is the existence of magnetic transitions for a very small exchange interaction J in this particular region of parameters, which includes also the maximum in the zero-field magnetic susceptibility presented in Figure 4.11.

Other interesting feature of this compound is its comparison to $\mathrm{YbCu_2Ge_2}$[81, 82]. Germanium has a larger atomic radius than silicon, having similar electronic configurations. Then Ge substitution acts as a negative pressure, dilating the crystal structure without any other significant modification. In $\mathrm{YbCu_2Ge_2}$ at low temperatures, the ytterbium valence is close to

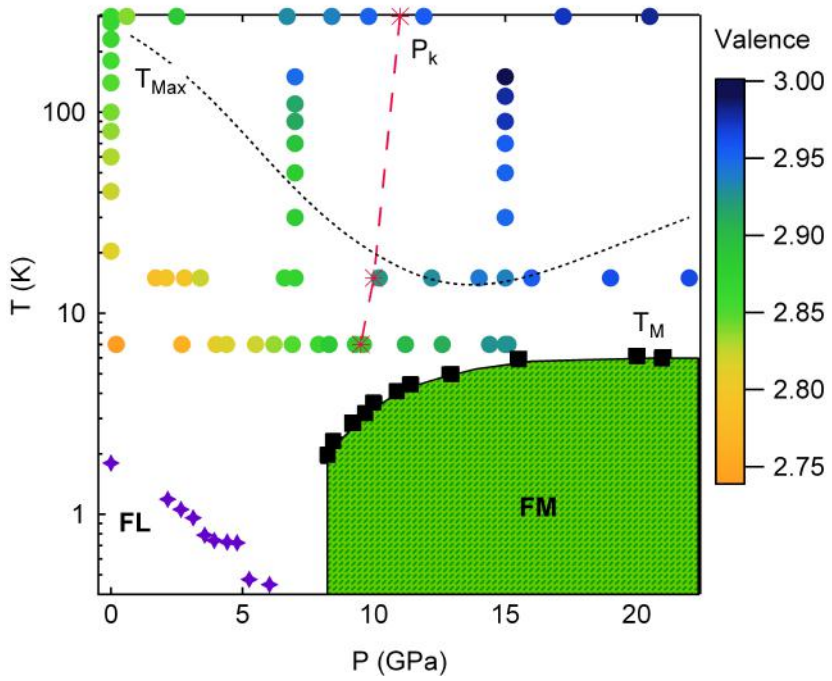

Figure 4.18: Phase diagram of $\mathrm{YbCu_2Si_2}$ under pressure. A ferromagnetic transition is seen at $8GPa$ with a Curie temperature on the order of 10K. The ytterbium valence is *continuous* for the whole phase diagram and increases with the pressure, as expected for Yb-based materials. Extracted from Ref.[38].

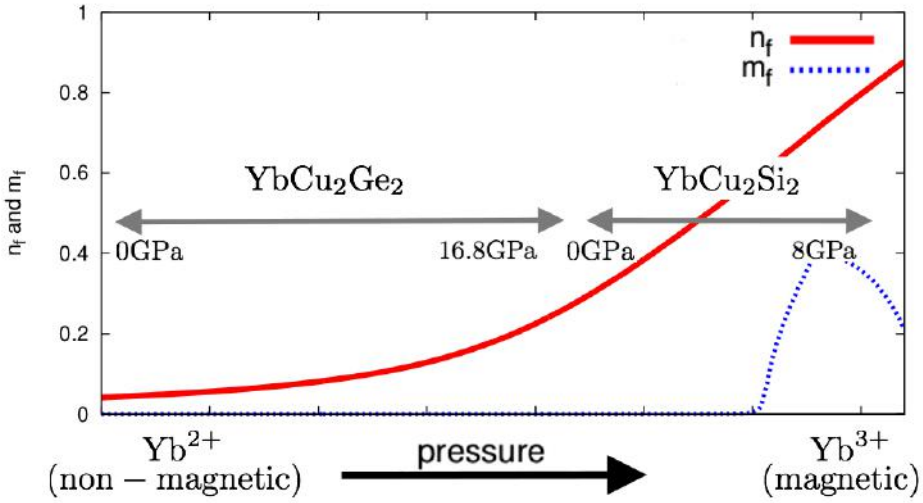

Figure 4.19: Schematic comparison between the EPAM and $\mathrm{YbCu_2(Si/Ge)_2}$ compounds. The pressure dependence of the valence (red solid line) and f-electron magnetization (blue dashed line) follows from the discussion in Section 4.3.1 (using scenario A) and the experimental values are extracted from Refs. [81] and [80]. Theoretical parameters: $V=0.1D$,$n_{tot}=1.2$, $U_{fc}=0.4D$,$J=0.01D$ and E_f varying from $E_f=-0.1D$ to $E_f=-0.5D$.

2 ($4f^{14}$ configuration) and the system behaves as a common metal with small effective mass ($\gamma \approx 10 mJ/mol.K^2$) and Pauli paramagnetism[81]. Under pressure the valence increases and heavy quasiparticles are formed ($\gamma \approx 80 mJ/mol.K^2$ at $p = 16.8 GPa$). It is expected that this system recovers all the features of the Si-based material in a higher pressure range, but it is experimentally unachievable.

The behavior of $\mathrm{YbCu_2(Si/Ge)_2}$ at low temperatures seems to follow the theory presented in Section 4.2.3. At low pressures Yb is almost divalent. Increasing the pressure the f-level energy decreases and approaches the Fermi level, which leads to increasing valence fluctuations. The enhancement of $4f^{13}$ configuration produces a ferromagnetic transition with a quite high effective moment. Since there is no sign of discontinuities in valence or in the volume under the applied pressure, we can conclude that U_{fc} plays a minor role in the valence variations.

To illustrate this specific point, we compare in Figure 4.19 the experimental data to results obtained from EPAM suitable for this particular compound. The pressure dependence on the model parameters follows the scenario A in Figure 4.17 and the calculation is done at zero temperature. Since the valence variation is continuous in $\mathrm{YbCu_2(Si/Ge)_2}$, we placed the compound in the crossover region. For $\mathrm{YbCu_2Ge_2}$ the corresponding valence is close to $2+$ and increases with pressure, while in $\mathrm{YbCu_2Si_2}$ the valence is already in an intermediate value (2.75) at zero pressure and a finite spontaneous magnetization is seen in the model and experimentally when the valence tends to 3.

The EPAM, treated with the approximations described in Section 3.3, misses a relevant phenomenon in the Yb^{3+} state: the Kondo effect. It would originate a large quasiparticle peak in the electronic density of states at the Fermi energy, what tends to increase the magnetic susceptibility close to the $n_f = 1$ region. Nevertheless, it is interesting to see that in any case the valence variation with the pressure cannot be explained only by the delocalization of f electrons from Kondo effect. If it was the case, the heavy fermion behavior would persist even when Yb valence is close to 2, which is in disagreement with the small Sommerfeld coefficient ($\gamma \approx 10 mJ/mol.K^2$) of $\mathrm{YbCu_2Ge_2}$.

4.3.3 $\mathrm{YbMn_6Ge_{6-x}Sn_x}$

The next compound to be analyzed in terms of our theory is $\mathrm{YbMn_6Ge_{6-x}Sn_x}$. It crystallizes in a hexagonal ($P6/mmm$) structure with a minor disorder from $x = 0$ to $x = 6$. The larger atomic radius of Sn implies that there is a negative pressure effect by doping with this atom. Then it is expected a valence drop (towards Yb^{2+} configuration) when the concentration of Sn is increased.

$\mathrm{YbMn_6Ge_{6-x}Sn_x}$ is a rare example of lanthanide intermetallics containing also magnetic transition metals. The presence of manganese in the crystal structure affects the Yb valence in nontrivial ways, as it was studied in Reference [83, 84]. Contrary to many examples of Yb-based compounds, for instance $\mathrm{YbCu_2(Si/Ge)_2}$ discussed in Section 4.3.2, the Yb valence decreases with the temperature for $\mathrm{YbMn_6Ge_{1.6}Sn_{4.4}}$. For the same composition, the Yb is magnetically ordered up to 90K (which is unusual), while Mn is ordered up to room temperature. The existence of highly polarized Mn states acts as a very strong magnetic field (close to 100T) on the Yb sites.

In Section 4.2.2 it was predicted that the action of an external magnetic field would favor the magnetic valence configuration and a large polarization of the f orbital. It is precisely what happens in this compound, apart from the fact that the Yb valence is slightly smaller than $3+$. This cannot be due to Kondo effect because the Kondo singlet is broken for such large fields.

Another point discussed by the authors in Ref.[83] is the considerably large valence variation in function of Sn concentration from $x = 4.2$ to $x = 4.4$ for a given temperature (see Figure 4.20) . For a lattice expansion of only 1.43%, the variation $\Delta v \approx 0.05$ seems quite large. One possibility is that U_{fc} is relevant in this compound, since the large exchange interaction between d states of Mn can intervene in a non-standard fashion. For that, a more systematic study of valence in this concentration region is desirable, supplemented by partial density of states measurements (via resonant photoemission spectroscopy).

In order to compare the experimental results presented in Figure 4.20 to the theory of EPAM, we include the basic aspects of $\mathrm{YbMn_6Ge_{6-x}Sn_x}$ in our model. First, we remind that from the experimental data in Fig. 4.20 it is possible to extract the Yb valence and the Yb and Mn magnetizations as a function of the temperature. The Mn magnetization $M_{\mathrm{Mn}}(T)$ is assumed to have the following temperature dependence, considering that ordering of Mn is mainly due to Mn-Mn interaction:

$$M_{\mathrm{Mn}}(T) = M_{\mathrm{Mn}}(0) \tanh\left(\frac{J_{\mathrm{Mn-Mn}} M_{\mathrm{Mn}}(0)}{T}\right) \tag{4.26}$$

Here $M_{\mathrm{Mn}}(0)$ is the magnetization at zero temperature and $J_{\mathrm{Mn-Mn}}$ is the exchange interaction among Mn atoms. This magnetization acts as an effective magnetic field $h_{eff}(T)$ in the Yb sites, which is given by:

$$h_{eff}(T) = J_{\mathrm{Yb-Mn}} M_{\mathrm{Mn}}(T) \tag{4.27}$$

$J_{\mathrm{Yb-Mn}}$ is the exchange interaction between Yb and Mn atoms. The Yb valence and magnetization will have an strong dependence on this field, which decreases when the temperature increases. These two quantities are given by the expressions:

$$n_f = n_f\left(h_{eff}(T), T\right) \tag{4.28}$$

$$m_f = m_f\left(h_{eff}(T), T\right) \tag{4.29}$$

The quantities above can be calculated from the EPAM model. Since we have shown that the temperature dependence of n_f is very small for $T \lesssim 0.05D$ in absence of magnetic fields (Section 4.1.2), we neglect the explicit temperature dependence in Eqs. 4.28 and 4.29. So the temperature dependence of n_f and m_f comes implicitly from the effective magnetic field $h_{eff}(T)$.

Figure 4.21 presents the valence (top) and the magnetization (bottom) dependence on T for three E_f values: $E_f = -0.4D$, $E_f = -0.2D$ and $E_f = -0.4D$ (the other parameters are indicated in the caption). These values are chosen to represent the increase of Sn concentration, which increases the primitive cell volume (Fig. 4.20). For $E_f = -0.4D$ (red curve), the f-level valence is nearly integral for any value of T and the magnetization decreases progressively from the $T = 0$ value $m_f \approx 0.6$. The f-level valence is in an intermediate value for $E_f = -0.2D$

(blue curve) and slightly decreases with T. Note that m_f decreases in a similar way as for $E_f = -0.4D$, but its value is always larger when $E_f = -0.2D$. Finally, if the valence is close to zero ($E_f = -0.0D$, green curve), than the f-level magnetization vanishes.

The results presented above qualitatively agree with the temperature dependence on the valence and the magnetization of $\mathrm{YbMn_6Ge_{6-x}Sn_x}$ (Figure 4.20, right). For $x = 3.8$ the Yb valence is nearly integral and the Yb magnetization decreases and vanishes at $T \approx 50K$. For $x = 4.2$ and $x = 4.4$ the valence is closer to an intermediate value and the Yb sites has a vanishing magnetization only at $T \approx 100K$. The difference between the total magnetization close to $T = 0$ and at $T = 100K$ for $x = 4.2$ is almost three times larger that for $x = 3.8$, which indicates that Yb magnetization is larger in the former case. Comparing to the results in 4.21, we see that the Yb in its intermediate valence regime has a larger magnetization than for the nearly integral valence state. For $x = 5.5$ the Yb has zero magnetization, even if the Mn is polarized up to $300K$, which can be explained by the fact that the Yb valence is smaller in this alloy.

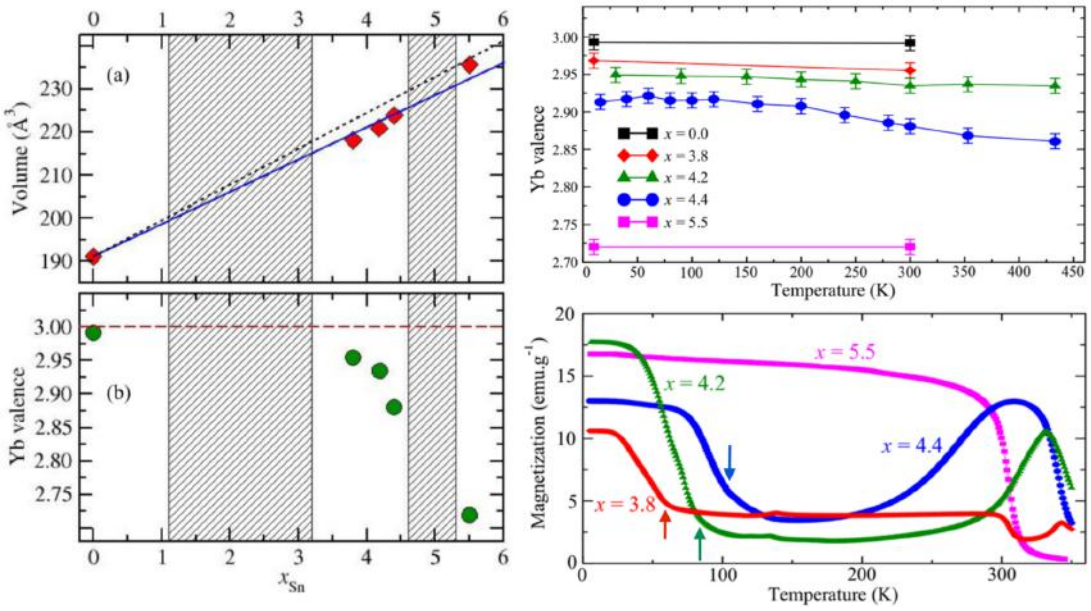

Figure 4.20: **Left:** Volume and Yb valence dependence on the concentration of Sn in $\mathrm{YbMn_6Ge_{6-x}Sn_x}$ at room temperature. The valence decreases with increasing volume, as expected for Yb-based systems. **Right:** Yb valence (top) and total magnetization of $\mathrm{YbMn_6Ge_{6-x}Sn_x}$ as a function of temperature for selected Sn concentrations x_{Sn}. Extracted from Ref. [84]).

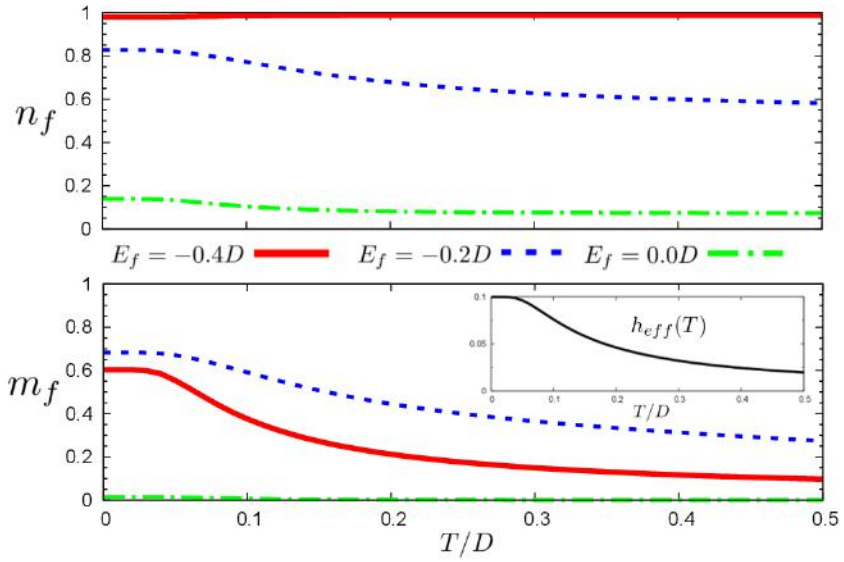

Figure 4.21: Theoretical results using our model to describe the Yb valence and magnetic behavior in $\mathrm{YbMn_6Ge_{6-x}Sn_x}$ as a function of temperature T (see text) . The results are shown for three values of E_f:$E_f = -0.4D$(red solid line),$E_f = -0.2D$(blue dashed line) and $E_f = 0.0D$(green dot-dashed line), representing an increasing Sn concentration. The parameters chosen were $U_{fc} = 0.4D$,$V = 0.1D$ and $n_{tot} = 1.5$ and we have used $J_{\mathrm{Mn-Mn}}M_{\mathrm{Mn}}(0) = J_{\mathrm{Yb-Mn}}M_{\mathrm{Mn}}(0) = 0.1D$ for simplicity. Here the temperature affects only the effective magnetic field on Yb atoms (Eq. 4.27 due to the magnetization of Mn ions (see text).

4.3.4 $\mathrm{Eu(Rh_{1-x}Ir_x)_2Si_2}$

Europium-based intermetallics are not studied as much as the Ce- and Yb-based materials, but they present a very interesting behavior with respect to valence. Contrary to Ce and Yb materials, the importance of Kondo effect in Eu systems is not so evident and the low temperature behavior very often deviates from the predictions based on the Doniach's diagram.

In intermetallic compounds, Eu possesses two valence configurations. The magnetic one is $Eu^{2+}(4f^7)$, which has a purely spin angular momentum $J = 7/2$, according to the Hund's rules. By giving one electron to the conduction band, the Eu ion becomes trivalent and its angular momentum cancels out exactly($J=0$). This situation does not happen for lanthanides situated in the beginning and the end of the series and one should wonder if it leads to different behavior than Ce and Yb.

Experimental evidences suggest that the valence transitions are enhanced in several Eu-based compounds[85, 86, 87]. One of these compounds is $\mathrm{Eu(Rh_{1-x}Ir_x)_2Si_2}$, which crystalizes in a tetragonal ($I4/mmm$) structure[88]. The unit cell volume goes from 171Å^3 at $x=0$ to 169.5Å^3 at $x=1$, corresponding to a volume reduction close to 1.5%.

The x-T phase diagram of $\mathrm{Eu(Rh_{1-x}Ir_x)_2Si_2}$ is presented in Figure 4.22. At low iridium concentrations the divalent configuration is stable and antiferromagnetic order takes place below $T_N \approx 25K$. For $x \approx 0.3$ the AF order disappears abruptly and the low temperature valence increases. At $T=T_v$, a first-order valence transition happens and the system is again divalent at higher temperatures. The first-order transition is unambiguously seen by the big hysteresis in thermodynamic quantities (for instance, the magnetic susceptibility)[88]. For $x \geq 0.75$ the valence transition becomes a crossover.

The most impressive feature of the phase diagram discussed above is the existence of a critical endpoint that separates the first-order from the crossover valence transition. To our knowledge, apart from the "historical" metallic Ce and SmS, it is the only compound that shows such point on its phase diagram. Note that these two other examples have substantial volume variations through the first-order line, which does not seem to be the case in this example, since the volume variation is close to 1%[88].

In order to establish the connection between the experimental phase diagrams and the EPAM, we plot in Figure 4.23 the valence dependence on the pressure and temperature close to the critical point. Here we have considered that the applied pressure (or the Ir doping) on $\mathrm{EuRh_2Si_2}$ is translated in an increasing E_f in the model. U_{fc} is chosen to be slightly above the zero-temperature critical endpoint, i.e. $U_{fc} > U^*_{fc}$ [4]. In this case, at very low temperature the valence transition is first-order, but by temperature effects (as discussed in Section 4.1.2) the transition is softened and becomes a crossover. The valence jump in the first-order line is overestimated in our approach using mean-field theory, being five times larger than what is seen experimentally ($\Delta v \approx 0.19$ [89]).

The real system presents an antiferromagnetic phase at low pressure with $T_N \approx 20K$, which disappears close to $p = 1GPa$ ($x_{\mathrm{Ir}} \approx 0.25$), when an intermediate valence state is stabilized. In the present work the question of antiferromagnetic order was not addressed, but from the

[4] We remind that the critical value for U_{fc} for $V=0.1D$ and $n_{tot}=1.5$ is $U^*_{fc}=0.53D$ (see Figure 4.1 and Section 4.1.2 for details.

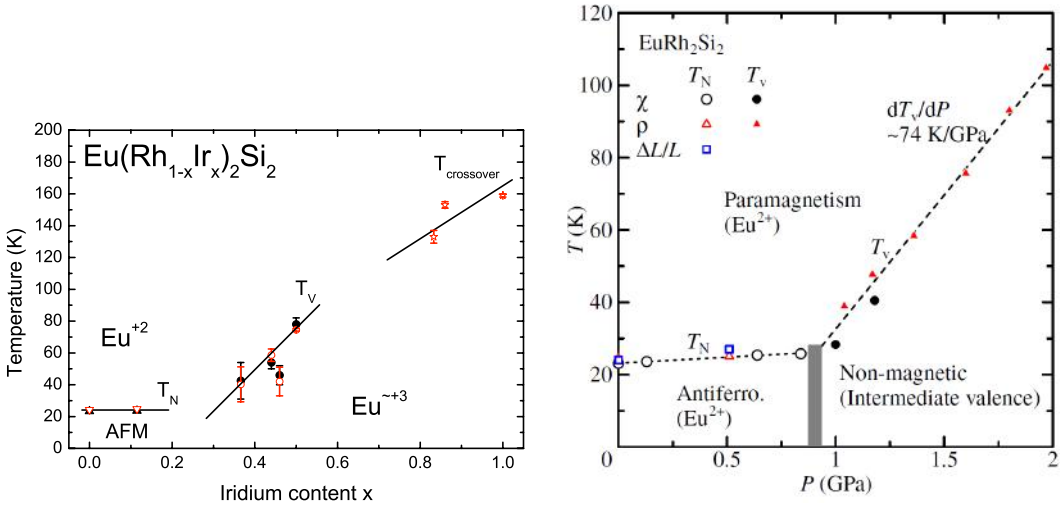

Figure 4.22: **Left:** x-T phase diagram for $\mathrm{Eu(Rh_{1-x}Ir_x)_2Si_2}$ from Ref.[88]. The passage from a first-order valence transition to a crossover happens at $x \approx 0.75$ (not specifically shown). **Right:** p-T phase diagram for $\mathrm{EuRh_2Si_2}$ from Ref.[89].

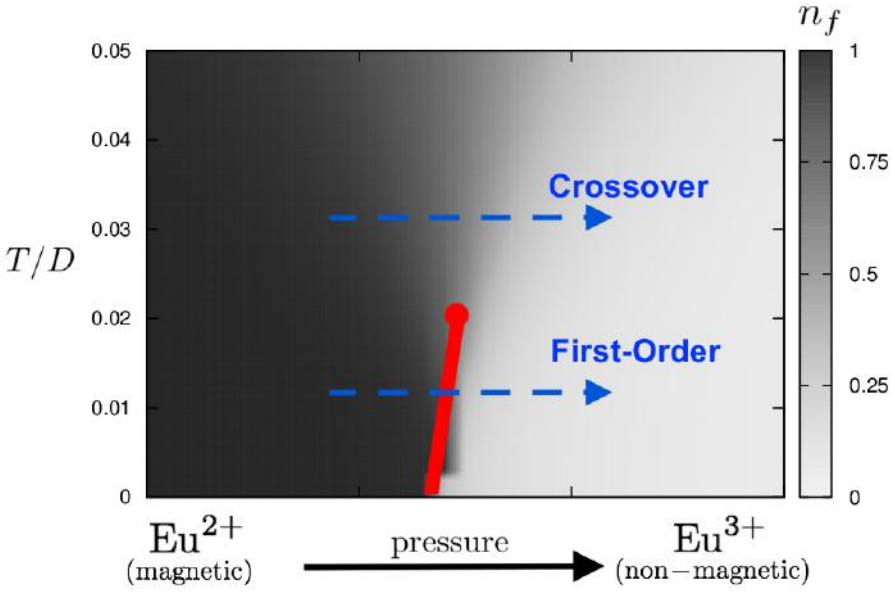

Figure 4.23: Valence phase diagram for $\mathrm{EuRh_2Si_2}$ under pressure (or Ir doping) using the EPAM model. Parameters are chosen to enforce the proximity to the zero temperature quantum critical point (see text). Parameters in the model: $V = 0.1D$, $n_{tot} = 1.5$, $U_{fc} = 0.55D$, E_f ranging from $E_f = -0.6D$ to $E_f = 0.2D$. The temperature range is indicated in the vertical axis.

points discussed in what concerns ferromagnetism (Section 4.2.3) it can be sustained that magnetic order is very sensitive to first-order valence transitions. Then it is expected that the first-order transition lines on Fig. 4.22 (represented by T_V) coincide with the antiferromagnetic transition line.

The existence of a critical point as in Figure 4.1 raises a natural question: how important is U_{fc} in Eu-based materials? If valence transitions are enhanced and eventually first-order in Eu intermetallics, one would expect a large U_{fc} interaction, especially if volume effects are not appreciable. On the other hand, Ce and Yb materials in a similar structure do not show this remarkable changing in the transition behavior, even that the electronic structure should be *a priori* similar.

The answer for the puzzle above is still open. It is most likely related to the energetic differences between the magnetic Eu^{2+} and the nonmagnetic Eu^{3+} configurations[90]. The large spin polarization energy (close to $1eV$) between these states would favor a first-order transition, which does not happen in $\mathrm{Ce(Yb)}$ transitions since it involves states with zero and one electron (hole). Obviously it is a multiorbital effect not described by the single orbital hamiltonian considered in this work, so U_{fc} acts here as an effective parameter that models this interaction.

Further analysis of this compound are highly desirable. For instance, spectroscopic measurements like RIXS could determine with precision the valence states through the transitions and clearly identify the location of the critical point in the phase diagram of Figure 4.22. Experiments under pressure and external magnetic field as those realized for $\mathrm{YbCu_2Si_2}$ could also help to understand the discrepancies between Eu and $\mathrm{Ce/Yb}$-based intermetallics.

4.3.5 Summary

In Section 4.3 the comparison between the results obtained for EPAM in Sections 4.1 and 4.2 and some compounds is made. The first compound is $\mathrm{YbCu_2Si_2}$[79], which presents a ferrromagnetic transition at $p = 8GPa$ for $T < 10K$. The Yb valence increases continuously with the applied pressure even inside the ferromagnetic phase. We propose that the ferromagnetic transition of $\mathrm{YbCu_2Si_2}$ under pressure can be accounted in the EPAM, which possesses a ferromagnetic instability in the intermediate valence region (see Section 4.2.1). For the second compound, $\mathrm{YbMn_6Ge_{6-x}Sn_x}$, we have used the EPAM model in the presence of a magnetic field developed in Section 4.2.2, given that the manganese magnetization acts as a large external field in the Yb site. For that reason, we have proposed a temperature-dependent magnetic field (Figure 4.21) that describes well the valence variations with temperature for different Sn concentrations. Lastly, we have discussed the case of Eu-based compounds, that usually present larger valence variations in comparison to Ce and Yb materials. The experimental phase diagram of $\mathrm{EuRh_2Si_2}$ as a function of Ir doping (in Rh sites) or pressure shows the existence of a first-order valence transition line that terminates in a critical point, which is also present in the EPAM phase diagram.

Chapter 5

Conclusions and perspectives

In Part I we have covered the topic of valence transitions in intermetallic lanthanide systems from a theoretical perspective. The description of valence transitions was made using an extended version of the Periodic Anderson model (Eq.3.1) that includes the repulsion between conduction and localized (f) electrons, represented by U_{fc}. This interaction is responsible for changing the character of valence variations from continuous (if U_{fc} is small) to discontinuous, if U_{fc} is large. The Extended Periodic Anderson model was treated by a combination of mean-field approximation for the U_{fc} term and infinite-U Hubbard-I approximation. These approximations yield a simple self-consistent calculation of the valence at zero and finite temperatures and it allows us to study additional effects, as the inclusion of an external magnetic field (Section 4.2.2) and ferromagnetic exchange interactions (Section 4.2.3).

The first important result obtained in Part I is the zero-temperature E_f-U_{fc} phase diagram in Figure 4.1: it shows how the valence crossover is transformed in a first-order valence transition line by U_{fc} interaction. This result is in agreement with other works on the EPAM using more sophisticated methods, which means that the mean-field approximation is a good choice of treatment. A second interesting result is the ferromagnetic instability predicted inside the intermediate valence region (Figure 4.11), which is explained by the large density of states at the Fermi level. Obviously such instability is reinforced in the presence of ferromagnetic interactions (see results of Section 4.2.3), which we have suggested as an explanation of the ferromagnetic transition in $\mathrm{YbCu_2Si_2}$ (Section 4.3.2). An open question is to know if antiferromagnetic instabilities exist in the EPAM, but for this particular point we need to provide a specific lattice structure (for example, a cubic lattice). Besides, we have investigated how the valence is affected by the application of an external magnetic field (Section 4.2.2). As expected, the magnetic field always favors the magnetic valence state ($n_f = 1$ in the EPAM), however it does not change the nature of the valence variation. Then it provides an experimental tool to investigate intermediate valence states and valence transitions.

Apart from the antiferromagnetic instabilities, some open questions deserves to be addressed and are perspectives for future works. One of them concerns the inclusion (or maintenance) of Kondo physics in the problem of valence transitions, allowing to go from the intermediate valence phase (studied here) to the Kondo limit by decreasing the f level energy E_f. The

Kondo limit is a particular case of the PAM (see Section 1.2) and is initially included in the EPAM, however the choice of Hubbard-I approximation "killed" the Kondo effect since it does not describe the quasiparticle peak that emerges at the Fermi level. This is particularly evident from the Hubbard model: the Hubbard-I approximation describes the lower and upper Hubbard sub-bands only and it is appropriate for the insulating phase. The inclusion of the Kondo peak in the density of states is granted in more sophisticated approximations, as the Dynamical Mean-Field Theory.

A second point that may be promising in the context of the EPAM is the inclusion of orbital effects. The motivation is based on the discrepancies between the valence phase diagrams of Ce/Yb and Eu materials, highlighted in Refs. [87, 88]. The "competing" valence configurations in Ce ($4f^0$ and $4f^1$) and Yb ($4f^{13}$ and $4f^{14}$) are composed of a completely empty (or full $4f$ orbital) and a one electron (one hole) state, being the non-magnetic configuration completely trivial. In europium the valence configurations are more "exotic": the magnetic state $4f^7$ is fully polarized ($J=S=7/2$) and has a large magnetic moment, while the non-magnetic state has $L=S=3$, but the third Hund's rule yields $J=0$. In order to study the quantitiative difference between Ce/Yb and Eu compounds via orbital effects, one can study an improved version of the EPAM with three local orbitals, which is a simplification of the seven $4f$ orbitals, but provides non-trivial configurations in which $J=0$.

Part II

Disorder in Kondo systems

Chapter 6

Introduction

In the second part of this thesis we will address the problem of disorder in Kondo systems from a theoretical perspective, more specifically the effect of magnetic-nonmagnetic substitutions in lanthanide (or actinide) metallic systems. Before entering in the details of our calculations, we will discuss some introductory aspects of the problem: the evolution from the Kondo impurity to the Kondo lattice, the effect of disorder in Kondo systems and some experimental results that motivate our work.

6.1 Kondo effect: from the impurity to the lattice

In Chapter 1 some aspects of the Kondo impurity (Eq.1.6) and the Kondo lattice (Eq.1.10) models were introduced. They correspond to particular cases of the single impurity and periodic Anderson models, respectively, in which the localized levels are occupied by one electron and the charge degrees of freedom are quenched. The passage from the Anderson to Kondo models is done through the Schrieffer-Wolff transformation [6], in which the f electrons retain only their magnetic degrees of freedom.

Kondo model describes the antiferromagnetic interaction between local moments and conduction electrons. Local moments are screened by conduction electrons below the Kondo temperature:

$$T_K = De^{-\frac{1}{J_K \rho^c(\mu)}}, \tag{6.1}$$

that depends exponentially on the Kondo coupling J_K and the conduction electrons density of states at the Fermi level $\rho^c(\mu)$.

The Kondo screening is indirectly observed through a logarithmic dependence of the electrical resistivity at $T \gtrsim T_K$ that appears both in the impurity and in the concentrated regimes. For lower temperatures, impurity and lattice have a different resistivity behavior: in the impurity regime, the scattering of conduction electrons by impurities is incoherent and it approaches the unitary limit, then the resistivity saturates as $T \to 0$. For the lattice the scattering becomes progressively elastic as the temperature is reduced [91] and the system achieves a *coherent state* below the coherence temperature T_{coh}. Then, for $T < T_{coh}$, the resistivity is given in

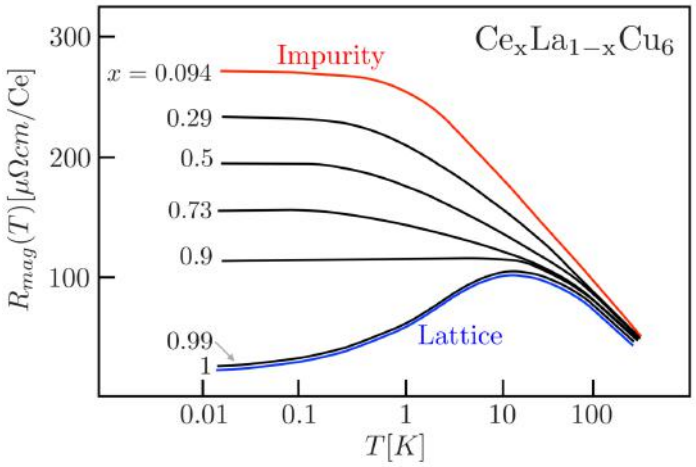

Figure 6.1: Magnetic contribution to the resistivity (normalized by the number of Ce atoms) of $\mathrm{Ce_xLa_{1-x}Cu_6}$ [92] as a function of temperature for different Ce concentrations. The curves corresponding to the single impurity and the lattice regime are highlighted in red and blue, respectively. Adapted from Ref.[92].

terms of the Fermi liquid expression $R(T) = R_0 + AT^2$, in which R_0 is the residual resistivity and A (the coefficient of electron-electron scattering contribution) is extremely large compared to common metals.

The development of coherence is clearly seen in the alloy $\mathrm{Ce_xLa_{1-x}Cu_6}$[92, 93]. The magnetic resistivity measurements from room temperature up to $T = 0.01K$ (Figure 6.1) show the difference between the impurity and the lattice regimes as the concentration of Ce is tuned. At high temperatures $T > 10K$ there is a clear logarithmic dependence on the temperature that is almost independent of concentration, signaling the Kondo effect. For $T < 10K$ the behavior depends on the concentration: in the diluted regime ($x < 0.5$), resistivity increases by decreasing temperature until saturation to a residual resistivity at $T \approx 1K$, which corresponds to the unitary limit of scattering. For the concentrated regime ($x > 0.5$), resistivity has a maximum around 10K and *decreases* at lower temperatures, until it achieves the residual resistivity.

6.1.1 Local versus Coherent Fermi Liquid

It was mentioned in Chapter 1 that the Kondo impurity and lattice models (Eqs. 1.6 and 1.10) have Fermi liquid (FL) fixed points at zero temperature. While in the impurity the FL behavior is universal, in the lattice other ground states are possible and the low temperature behavior depends on specific details of each system. In many dense systems, the FL ground state of the lattice is in competition with antiferromagnetic order, which is described by the Doniach diagram (Fig. 1.2).

The FL description of the single impurity Kondo problem was developed by Nozières[94] and it is known as Local Fermi Liquid (LFL). The starting point of Nozières theory is that

$J_K \to \infty$ at low temperatures, as shown by scaling arguments by Anderson[9]. In this limit, the magnetic impurity moment forms a rigid singlet state with one conduction electron spin and an infinite energy is required to break it. The impurity acts as a non-magnetic scattering site with infinite repulsion. Including the virtual excitations of the singlet, he has shown that additional interactions are irrelevant in a $1/J_K$ expansion.

The Fermi liquid regime of the Kondo lattice, sometimes denote Coherent Fermi Liquid (CFL), corresponds to the heavy fermion behavior introduced in Section 1.2. The striking property of the CFL is the extremely high effective mass of its quasiparticles, which can be explained by the two (s-f) band picture given by mean-field theory: the Kondo Lattice model is transformed in a model with two hybridized bands, representing the conduction and the (dispersionless) f electrons (see Section 7.2).

The "exhaustion" problem

In order to achieve a non-magnetic ground (CFL) state in the Kondo lattice, conduction electrons must quench the spin degrees of freedom of an outnumbered local moments. Considering that the effective number of conduction electrons participating in the screening are located in a energy window of $T_K (T_K \ll D)$, then the magnetic moments largely outnumber it and the picture of individual Kondo cloud must be reconsidered. This "exhaustion problem" was first proposed by Nozières [95, 96], who used an entropy argument to estimate that the coherence temperature $T_{coh} \sim \rho^c T_K^2$.

Nozières estimation was proven to be wrong by mean-field calculations[97, 98, 99]: the ratio T_{coh}/T_K depends only on band structure details, but not on T_K (or J_K) [97, 98]. The physical argument to explain it is the following: in a Kondo Lattice, the "true" quasiparticles at low temperature are a combination of the conduction and the localized electrons, so the f electrons are (in some sense) "screening themselves"[14].

6.1.2 Strong-coupling picture of Kondo impurity and lattice models

The strong-coupling limit $J_K \to \infty$ of the Kondo impurity and lattice models is a simple way to understand their low temperature behavior and Fermi liquid properties. According to Renormalization Group calculations[10], $J_K \to \infty$ is the low temperature fixed-point of the impurity problem. In the lattice, the ground state is expected to be magnetic for large J_K. Here, we are interested in non-magnetic states of the Kondo lattice in the limit $J_K \to \infty$, since it yields an interesting physical picture that can help to understand the CFL for lower J_K.

The $J_K \to \infty$ picture for the Kondo impurity model is represented in Figure 6.2. The magnetic impurity forms a rigid singlet state with one conduction electron and an infinite energy is required to break it. Consequently, the impurity site is forbidden for the remaining conduction electrons. The $N_c - 1$ (N_c is the total number of conduction electrons) remaining conduction electrons are the system quasiparticles, moving in a lattice depleted by one site.

In this picture [100, 96], the $N_c = n_c N$ conduction electrons form local singlet states with a fraction of the N local moments in the lattice (assuming that $N_c < N$), while $N - N_c$ moments

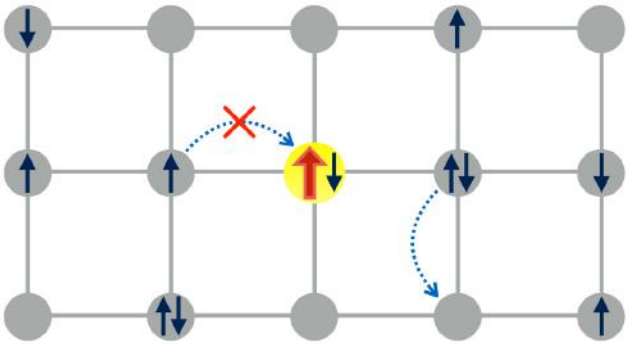

Figure 6.2: Strong coupling picture of single impurity Kondo problem. The impurity and the conduction electron spins are represented by the red thick and the blue thin arrows, respectively. The impurity local moment forms a singlet state (represented in yellow) with one conduction electron. The impurity site is "forbidden" for the other conduction electrons, since it requires infinite energy to break the singlet. The remaining conduction electrons move freely in the depleted lattice.

are unscreened (the bachelor spins). Thanks to the electronic mobility, conduction electrons will hop to bachelors spins and the CFL ground state is assured to be non-magnetic by this dynamical effect. Effectively the bachelor spins behave as *holes* of a lattice containing a singlet per site (a Kondo insulator), having an infinite repulsion between them since two holes cannot occupy the same lattice site. This situation is depicted in Figure 6.3.

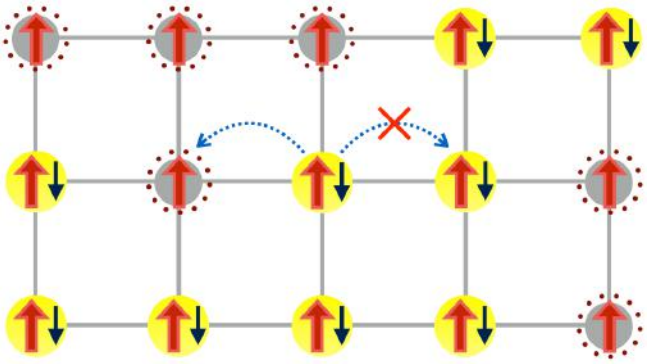

Figure 6.3: Strong coupling picture of Kondo lattice problem. Every conduction electron in the lattice forms a local singlet (in yellow) with a local moment, while the remaining moments (represented by the thick red arrows surrounded by red dots) stay unscreened. Hopping processes of conduction electrons are possible *only* toward sites with unscreened spins. One can equally think that the charge carriers in the system are *holes* in unscreened spin sites, having an effective repulsive interaction (see text).

It is possible to check two important results from the analysis above. First, the number

of quasiparticles in the system is $2N-(N-N_c)=N+N_c$, since holes are moving in the lattice. This verifies the *Luttinger's theorem*[2] for the Kondo lattice[101], which states that conduction electrons and local moments contribute to the Fermi surface.

The second result is the formal equivalence between the $J_K \to \infty$ Kondo lattice with N_c electrons and the $U \to \infty$ Hubbard model with $N-N_c$ electrons[100, 96]. We can compare it to the LFL for the impurity (Fig. 6.2), where the effective quasiparticles interaction is zero and the only modification with respect to the "clean" system is the depletion of the impurity site. So, from the $J_K \to \infty$ point of view, the Local and the Coherent Fermi Liquids have different "types" of quasiparticles: non-interacting electrons in LFL and "hard-core" interacting holes in CFL.

The strong-coupling picture presented in this section can be generalized for a system with an arbitrary numbers of local moments (Kondo Alloys). Such generalization will be discussed in Section 7.1.2.

6.2 Substitutional disorder in Kondo systems

In this section we briefly review some aspects of substitutional disorder in Kondo systems in a global perspective. From the stoichiometric point of view there are two non-equivalent forms of substitution in heavy fermion families of materials[1], depending on the atom that is replaced. For a f *site substitution*, the magnetic rare-earth atom is replaced by a non-magnetic one, as in $\mathrm{Ce_xLa_{1-x}Cu_6}$ [92, 93] or $\mathrm{U_xTh_{1-x}Pd_2Al_3}$ [102, 103]. Distinctively, a *ligand substitution* occurs when atoms other than the rare-earth (ligand atoms) are replaced, as in $\mathrm{CeCu_{6-x}Au_x}$ [19] or $\mathrm{UCu_{5-x}Pd_x}$ [104]. Here we are going to focus on the f site substitution.

6.2.1 Non-Fermi liquid behavior from disorder

A frequent consequence of substitution in heavy fermions systems is the appearance of Non-Fermi Liquid (NFL) behavior[18], characterized by a violation of Fermi Liquid theory with respect to the temperature dependence of physical quantities. Many scenarios for Non-Fermi liquid behavior in heavy fermions have been proposed[105, 106], including the proximity of the quantum critical point of the Doniach's diagram[107] or a quantum critical point associated to valence transitions[68], models for multichannel Kondo effect [108, 109] and theories on disorder effects[110, 111, 112]. The pertinence of these theories relies on the specific details of the compounds that are meant to be described.

Here we will focus on theories in which disorder is considered to be the driving force of Non-Fermi liquid behavior. The common aspect of these theories [113, 110, 111] is that disorder induces different local environments for the magnetic moments and, consequently, a distribution of Kondo temperatures $p(T_K)$. Because T_K has an exponential dependence on the local energy scale, $p(T_K)$ is a skewed distribution.

[1] By heavy fermion family we mean compounds that possess heavy fermion behavior in a given composition. For a known example, $\mathrm{Ce_xLa_{1-x}Cu_6}$ enters in this classification, since it is a heavy fermion for $x=1$.

Following the analysis of Refs.[110, 114], we can estimate the thermodynamic behavior of a system displaying such distribution $p(T_K)$. For example, the average magnetic susceptibility can be calculated. For a single Kondo impurity expression, we adopt the form from Wilson[1]:

$$\chi(T, T_K) = \frac{A}{T + bT_K} \tag{6.2}$$

Here A and b are constants. The average susceptibility with respect to $p(T_K)$ is given by:

$$\overline{\chi(T)} \simeq \int_0^{+\infty} dT_K p(T_K) \frac{A}{T + bT_K} \tag{6.3}$$

The upper limit of the integral above does not contribute, since $p(T_K)$ does not extend entirely to infinite, so the interest is in the low-T_K limit. Let us first suppose that $p(T_K)$ is a finite quantity as $T_K \to 0$. Then, using the leading term from the Taylor expansion $p(T_K) = p_0$ and introducing a cutoff Γ, we have:

$$\overline{\chi(T)} \simeq \int_0^{\Gamma} dT_K p_0 \frac{A}{T + bT_K} \sim \frac{p_0 A}{b} \log\left(\frac{\Gamma}{T}\right) \tag{6.4}$$

So a logarithm divergence appears in the low temperature behavior of the magnetic susceptibility, in a clear contrast to the Fermi liquid behavior $\chi = \chi_0 + AT^2$. As a conclusion, if there is a finite distribution of moments having $T_K \to 0$, it leads immediately to Non-Fermi Liquid behavior. The divergence is stronger in the case of a singularity in $p(T_K)$. In the case of a power-law distribution[115, 114] for $p(T_K) \sim T_K^{\alpha-1}$, we have:

$$\overline{\chi(T)} \simeq \int_0^{\Gamma} dT_K (T_K)^{\alpha-1} \frac{A}{T + bT_K} \sim \begin{cases} \chi_0 \ , \text{ if } \alpha > 1 \\ T^{\alpha-1} \ , \text{ if } \alpha < 1 \end{cases} \tag{6.5}$$

For $\alpha > 1$, the distribution $p(T_K)$ does not diverge as $T_K \to 0$ and $\overline{\chi(T)}$ remains finite when $T \to 0$, as in a Fermi liquid. On the other hand, Non-Fermi liquid behavior is observed in $\overline{\chi(T)}$ if $\alpha < 1$. In a similar way, NFL behavior of the specific heat coefficient $\gamma = C/T$ can be deduced from a distribution of T_K. Further details on these calculations, for instance the disorder dependence of α in Kondo systems, the References [114, 115, 116] are recommended.

6.2.2 Kondo Alloys: experimental motivation

Kondo alloys are systems where the concentration of local moments is tuned by the amount of the magnetic ion. The typical example is the substitution of lanthanum (in La^{3+} valence state) by cerium (Ce^{3+} valence state), but there are examples with other atoms involved. One issue of this type of substitution is the multiple effects that can appear when it is performed. For instance, there are volume effects inherent to different ionic radius ($R_{La^{3+}} = 103.2pm$ and

$R_{Ce^{3+}} = 101.0pm$ [22]). Furthermore, the substitution affects not only the electrical properties (as the resistivity), but also the magnetic properties (susceptibility).

A first example of Kondo alloy is $\mathrm{Ce_xLa_{1-x}Cu_6}$ shown in Figure 6.1. The low T behavior of its resistivity was discussed in the context of coherence formation and the evolution from the impurity to lattice regimes. Other examples are $\mathrm{Ce_xLa_{1-x}CoIn_5}$ [117, 118], $\mathrm{Ce_xLa_{1-x}Pd_3}$[119], $\mathrm{Ce_{1-x}La_xPtGa}$[120], $\mathrm{Ce_xLa_{1-x}B_6}$[121], $\mathrm{Ce_{1-x}La_xCu_2Ge_2}$[122], $\mathrm{(Ce_xLa_{1-x})_7Ni_3}$ [123] or $\mathrm{U_{1-x}Th_xPd_2Al_3}$[102, 103].

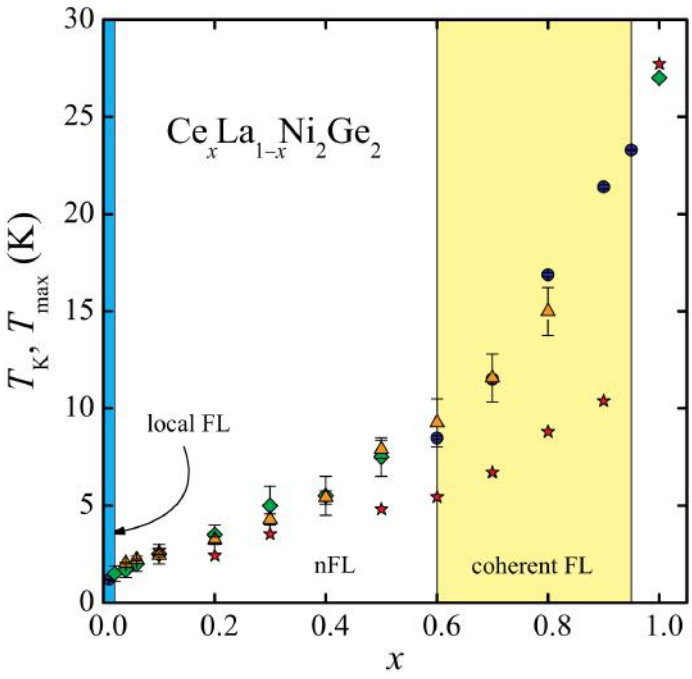

Figure 6.4: Experimental phase diagram of $\mathrm{Ce_xLa_{1-x}Ni_2Ge_2}$ as a function of Ce concentration x.The two Fermi Liquids regions indicated in blue (Local FL) and yellow (Coherent FL) are determine by specific heat, resistivity and thermopower measurements and the points characterize different system energy scales, namely the Kondo and the coherence temperatures. The Fermi Liquid regions are separated by a Non-Fermi Liquid region that spans a large range of intermediate concentrations. Figure adapted from Ref. [124].

Let us focus on a particular example of compound: $\mathrm{Ce_xLa_{1-x}Ni_2Ge_2}$ [124]. It is a heavy fermion system in the Ce-rich phase ($\mathrm{CeNi_2Ge_2}$) with a large Sommerfeld coefficient $\gamma \approx 350\mathrm{mJ/K^2mol}$ [125, 126]. Anomalous behavior of the specific heat of $\mathrm{CeNi_2Ge_2}$ in mK scales suggests that it is very close to a magnetic quantum critical point. While the magnetic transition is observed via the $\mathrm{Ni\text{-}Pd}$ or $\mathrm{Ge\text{-}Cu}$ substitution, the same is not seen when Ce is replaced by La. Instead, a coherent Fermi Liquid regime is obtained in the range $0.95 < x < 0.6$. For $0.5 < x < 0.02$ Non-Fermi liquid behavior is reported, while the system is again a Fermi liquid (local FL) for $x < 0.02$ (Figure 6.4).

The compound $\mathrm{Ce_xLa_{1-x}Ni_2Ge_2}$ is non-magnetic in the whole range of substitution and it has two different Fermi Liquid phases well separated by a large region of Non-Fermi Liquid

behavior. Moreover, the results in Refs. [124, 127] indicate that the Kondo temperature is independent of x. The interpretation of these results leads us to propose that the Non-Fermi Liquid behavior in the range $0.5 < x < 0.02$ is induced by disorder, in a possible association with the loss of coherence by La doping.

In the next chapter we will propose a model to describe non-magnetic phases of Kondo Alloys as $\mathrm{Ce_xLa_{1-x}Cu_6}$ or $\mathrm{Ce_xLa_{1-x}Ni_2Ge_2}$ using a method suitable to treat the combined effects of coherence and disorder.

Chapter 7

Model and method

In this chapter we will introduce the model hamiltonian that describes the physics of alloys containing randomly displaced magnetic moments and the numerical method used to solve it. We start from the presentation of the model and its relation with the compounds discussed in Section 6.2.2. Then the approximations employed in this work are shown in details: the mean-field approximation for the Kondo problem (Section 7.2) and the statistical DMFT for disorder effects (Section 7.3).

7.1 The Kondo Alloy model

Our goal is to describe rare-earth systems in which the concentration of magnetic moments can be tuned by substitution. One example is the La-Ce substitution, supposing that the cerium configuration is magnetic. The model hamitonian is the Kondo Alloy model (KAM):

$$\mathcal{H} = -\sum_{ij\sigma}(t_{ij} + \mu\delta_{ij})c^{\dagger}_{i\sigma}c_{j\sigma} + J_K \sum_{i \in \mathcal{K}} \mathbf{S}_i \cdot \mathbf{s}_i \tag{7.1}$$

The first term describes the kinetic energy of conduction electrons given by the hopping integral t_{ij}. The number of conduction electrons per lattice site is fixed by the chemical potential μ. The second term is the Kondo interaction, i.e. a local antiferromagnetic coupling between the local moment, described by the spin operator $\mathbf{S}_i$, and the spin of conduction electrons ($\mathbf{s}_i$). The Kondo interaction takes place only in a subset $\mathcal{K}$ of the N lattice sites, which is composed by the sites containing local moments that are randomly distributed along the lattice (quenched disorder). The interaction strength J_K is the same for all the Kondo sites and it is a positive quantity. We have supposed that the hopping integral t_{ij} does not depend on the nature of the sites i and j.

Apart from the lattice geometry (given by t_{ij}) and the Kondo interaction J_K, there are two other controlled parameters: the concentration of magnetic moments x, ranging from $x=0$ to $x=1$, and the concentration of conduction electrons n_c, from $n_c=0$ to $n_c=2$. In the absence of magnetic moments ($x=0$), the system behaves as a normal metal with a single electronic band. In the presence of one magnetic impurity ($xN=1$), the KAM corresponds to the single

impurity Kondo model, discussed in Section 1.1.2. Otherwise, if the number of local moments is maximum ($x=1$), i.e. every lattice has a local moment, the KAM is equivalent to the Kondo Lattice model (Eq. 1.10).

We assume that the only variation occurring in the system under the substitution is the presence/absence of a local moment and the Kondo interaction. In reality, this type of substitutions produces disorder in the conduction electrons energy and lattice distortions, since the electronic levels and ionic volumes are different from one rare-earth atom to other. Here we neglect these effects for simplicity. We are also considering a $S=1/2$ spin for the local moment and only one conduction electron band.

7.1.1 State-of-art

The Kondo Alloy model was previously studied by several authors. Early works of Kurata[128, 129] using the Coherent Potential Approximation (CPA) were focused on the analytical calculations for the density of states and the resistivity within this approximation.

More recently, Burdin and Fulde [130] have employed a matrix form of CPA, showing that it is equivalent to a matrix dynamical mean-field theory, and mean-field interaction for the Kondo interaction. They have focused the analysis of the relation between the Fermi liquid and the Kondo temperatures, T_0 and T_K, for different concentration x of magnetic moments. In particular, the ratio T_0/T_K exhibits a different behavior when $x<n_c$ and $x>n_c$.

Kaul and Vojta[131] combined the mean-field approximation for the Kondo interaction with exact diagonalization in a 20×20 square lattice to investigate the same model. This approach allows to study the spatial distribution of local quantities for a disorder realization. In particular, they have shown that the mean-field energy scale T^*, defined from the averaged value of the mean-field parameter r^2 (see Section 7.2), has a sharp change around the point $x=n_c$, as it is shown in Figure 7.1. A similar change was found by Watanabe and Ogata[62] using Variational Monte Carlo calculations. Besides, many studies using a disordered version of the Periodic Anderson model were made in a similar context[132, 133, 134, 135], most of them employing CPA.

7.1.2 The $J_K \to \infty$ limit

The $J_K \to \infty$ limit of the Kondo Alloy model was recently studied by Burdin and Lacroix[136]. In this work, the existence of a "Lifshitz-like" transition separating the Local and the Coherent Fermi liquids at $x = n_c$. In Section 6.1.2 the physical picture of the strong coupling limit was presented for the impurity and the lattice cases. If we generalize this picture for any concentration x of local moments, we have the following situations:

- Situation I ($x < n_c$): The $N_s = xN$ magnetic moments form rigid singlets with the same number of conduction electrons and an infinite energy is required to break any of these singlets. The remaining electrons ($(n_c-x)N$) are free carriers in a lattice depleted by xN sites, assuming that the former percolates[1]. The number of quasiparticles is

[1]The issue of percolation will be discussed in more details in Section 8.4

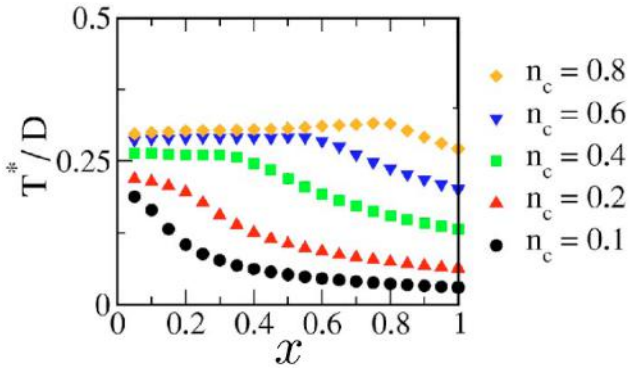

Figure 7.1: Dependence of the coherent temperature T^* on the concentration of magnetic impurities for the KAM. The point $x=n_c$ marks the crossover from the diluted ($x<n_c$) to the concentrated ($x>n_c$) regime. Figure adapted from Ref.[131].

$$N_{qp}=N_c-N_s=(n_c-x)N.$$

- Situation II($x>n_c$): The $N_c=n_cN$ conduction electrons in the lattice form singlet states with local moments, leaving $(x-n_c)N$ unscreened moments (the bachelor spins). The electronic hopping occurs only between Kondo sites (as in Fig. 6.3), what can be seen as the movement of bachelor spins in a lattice depleted by $(1-x)N$ Non-Kondo sites. The number of quasiparticles in this regime is $N_{qp}=N_s+N_c=(n_c+x)N$, given the holelike character or the carriers. The electronic correlation comes not only from the lattice depletion, but also by an infinite repulsion that prevents the double occupation of holes (following Ref.[100]).

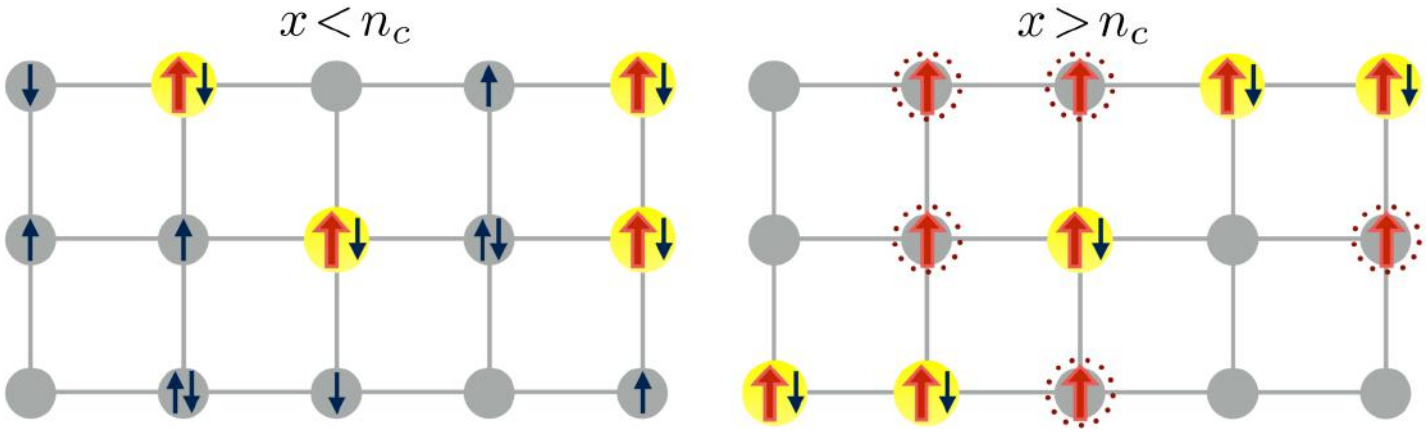

Figure 7.2: Strong coupling picture of the Kondo Alloy model for $x<n_c$ (left) and $x>n_c$ (right).

By increasing the concentration x, one should expect to pass from the former to the latter situation when $x=n_c$. In this point there is a discontinuity in the number of quasiparticles (from $(n_c-x)N$ to $(n_c+x)N$), in the effective number of lattice sites (from $N-N_s$ to N_s)

and in the effective Hubbard repulsion (from zero to infinity). According to Ref. [136] this singularity is related to a singular change of the Fermi surface (a Lifshitz transition[137]), and not to a symmetry breaking.

7.2 Mean-field approximation for the Kondo problem

The mean-field approximation here employed follows Reference [53] and it is equivalent to the slave boson mean-field theory[138, 139, 140].

We use the relation:

$$\mathbf{S}_i \cdot \mathbf{s}_i = S_i^z s_i^z + \frac{1}{2}\left(S_i^+ s_i^- + S_i^- s_i^+\right) \tag{7.2}$$

and write the spin operators in their fermionic representation:

$$S_i^z = \frac{1}{2}\sum_\sigma \sigma f_{i\sigma}^\dagger f_{i\sigma} \; ; \; S_i^+ = f_{i\uparrow}^\dagger f_{i\downarrow} \; ; \; S_i^- = f_{i\downarrow}^\dagger f_{i\uparrow} \tag{7.3}$$

$$s_i^z = \frac{1}{2}\sum_\sigma \sigma c_{i\sigma}^\dagger c_{i\sigma} \; ; \; s_i^+ = c_{i\uparrow}^\dagger c_{i\downarrow} \; ; \; s_i^- = c_{i\downarrow}^\dagger c_{i\uparrow} \tag{7.4}$$

The hamiltonian in Eq. 7.1 then becomes ($\overline{\sigma} \equiv -\sigma$):

$$\mathcal{H} = -\sum_{ij\sigma} t_{ij} c_{i\sigma}^\dagger c_{j\sigma} + J_K \sum_{i\,\in\,\mathcal{K}} \left[S_i^z \sigma_i^z + \frac{1}{2}\sum_\sigma f_{i\sigma}^\dagger f_{i\overline{\sigma}} c_{i\overline{\sigma}}^\dagger c_{i\sigma} \right] \tag{7.5}$$

The mean-field approximation consists in approximating the terms with four operators in Eq. 7.5 by:

$$S_i^z \sigma_i^z = \langle S_i^z \rangle \, \sigma_i^z + \langle \sigma_i^z \rangle \, S_i^z - \langle S_i^z \rangle \, \langle \sigma_i^z \rangle \tag{7.6}$$

and

$$\sum_\sigma f_{i\sigma}^\dagger f_{i\overline{\sigma}} c_{i\overline{\sigma}}^\dagger c_{i\sigma} = -\sum_\sigma \left(\left\langle f_{i\sigma}^\dagger c_{i\sigma} \right\rangle c_{i\overline{\sigma}}^\dagger f_{i\overline{\sigma}} + \left\langle c_{i\overline{\sigma}}^\dagger f_{i\overline{\sigma}} \right\rangle f_{i\sigma}^\dagger c_{i\sigma} - \left\langle f_{i\sigma}^\dagger c_{i\sigma} \right\rangle \left\langle c_{i\overline{\sigma}}^\dagger f_{i\overline{\sigma}} \right\rangle \right) \tag{7.7}$$

By replacing the local spin operators S_i^z for fermions, one must assure local charge conservation:

$$\sum_\sigma f_{i\sigma}^\dagger f_{i\sigma} = 1 \; , \; \forall \; i \in \mathcal{K} \tag{7.8}$$

This is done by the inclusion of a local Lagrange multiplier λ_i, that might be different at each Kondo site.

The mean-field approximation introduces average values[141]: $\langle S_i^z \rangle$, $\langle s_i^z \rangle$ and $< f_{i\sigma}^\dagger c_{i\sigma} >$. The first two averages measure the local polarization of f and c electrons, respectively, and are nonzero in magnetic phases only. The third average, $< f_{i\sigma}^\dagger c_{i\sigma} >$, measures the local degree of hybridization between conduction and f electrons and it is related to the local singlet formation

by Kondo effect.We assume from now on that the system is in a non-magnetic state. Then the second term in Eq. 7.5 will not be considered. The third term in Eq. 7.5 simplifies since the averages $< f^{\dagger}_{i\sigma} c_{i\sigma} >$ are spin-independent under this assumption. Defining:

$$r_i \equiv -J_K \left\langle f^{\dagger}_{i\sigma} c_{i\sigma} \right\rangle , \tag{7.9}$$

and considering r_i as a real quantity, the hamiltonian reads:

$$\mathcal{H} = -\sum_{ij\sigma} t_{ij} c^{\dagger}_{i\sigma} c_{j\sigma} - \mu \sum_{i\sigma} \left(c^{\dagger}_{i\sigma} c_{i\sigma} - \frac{n_c}{2} \right) + \sum_{i \in \mathcal{K}} \sum_{\sigma} r_i \left(c^{\dagger}_{i\sigma} f_{i\sigma} + f^{\dagger}_{i\sigma} c_{i\sigma} \right) - \sum_{i \in \mathcal{K}} \sum_{\sigma} \lambda_i \left(f^{\dagger}_{i\sigma} f_{i\sigma} - \frac{1}{2} \right) + \sum_{i \in \mathcal{K}} \frac{2 r_i^2}{J_K} \tag{7.10}$$

In Eq. 7.10, two Lagrange multipliers were included. The first one is the chemical potential μ that fixes the average number of conduction electrons n_c in the lattice (a *global* constraint). The second is a *local* multiplier λ_i, which constraint the number of f electrons to one in each Kondo site.

The hamiltonian in Eq. 7.10 describes hybridized s and f bands. The hybridization r_i is a local quantity, as well as the position of the f-level λ_i, reflecting the disorder. Both r_i and λ_i are self-consistent parameters determined by Eqs. 7.8 and 7.9.

The determination of the mean-field parameters λ_i and r_i comes from the solution of local self-consistent equations. Introducing the finite temperature Green's functions in site representation[3, 2],

$$G^{cc}_{i\sigma,j\sigma'}(\tau) \equiv -\left\langle T_\tau c_{i\sigma}(\tau) c^{\dagger}_{j\sigma'}(0) \right\rangle , \tag{7.11}$$

$$G^{ff}_{i\sigma,j\sigma'}(\tau) \equiv -\left\langle T_\tau f_{i\sigma}(\tau) f^{\dagger}_{j\sigma'}(0) \right\rangle , \tag{7.12}$$

$$G^{cf}_{i\sigma,j\sigma'}(\tau) \equiv -\left\langle T_\tau c_{i\sigma}(\tau) f^{\dagger}_{j\sigma'}(0) \right\rangle , \tag{7.13}$$

$$\tag{7.14}$$

defined for the imaginary time τ (T_τ is the imaginary-time ordering operator). Thermal averages as $\left\langle f^{\dagger}_i c_i \right\rangle$ and $\left\langle f^{\dagger}_i f_i \right\rangle$ are computed[2] in the limit $\tau \to 0^-$,

$$\left\langle f^{\dagger}_i c_i \right\rangle = G^{cf}_{i,i}(\tau = 0^-)$$
$$\left\langle f^{\dagger}_i f_i \right\rangle = G^{ff}_{i,i}(\tau = 0^-),$$

leading to the following equations for r_i and λ_i (if $i \in \mathcal{K}$):

$$\frac{1}{2} = G^{ff}_{ii}(\tau = 0^-) \tag{7.15}$$

$$r_i = -J_K G^{cf}_{ii}(\tau = 0^-) \tag{7.16}$$

[2]From now on spin indices are dropped for shortness.

The evaluation of $G_{ii}^{ff}(\tau = 0^-)$ and $G_{ii}^{cf}(\tau = 0^-)$ are done via a sum over fermionic Matsubara's frequencies, which are presented in details in Appendix D. At $T = 0$, we have from Equations D.7 and D.9:

$$G_{ii}^{ff}(\tau = 0^-) = \frac{1}{\pi} \int_0^{+\infty} d\omega \mathrm{Re}\left(G_{ii}^{ff}(\omega)\right) + \frac{1}{2} \tag{7.17}$$

$$G_{ii}^{cf}(\tau = 0^-) = \frac{1}{\pi} \int_0^{+\infty} d\omega \mathrm{Re}\left(G_{ii}^{cf}(\omega)\right) \tag{7.18}$$

7.2.1 Green's functions

The hamiltonian in Eq. 7.10 can be rewritten as:

$$\mathcal{H} = -\sum_{ij\sigma} t_{ij} c_{i\sigma}^\dagger c_{j\sigma} + \sum_i \mathcal{H}_i^0 + \mathrm{cts.} \tag{7.19}$$

This expression contains only one non-local term: the kinetic energy of conduction electrons. It corresponds to conduction electrons hopping in and out of a particular site. The local part contains the chemical potential for the conduction electrons, equal in all the sites, and the f-operators contribution, present if i is a Kondo site. For Non-Kondo sites $r_i = 0$ and we artificially introduce an f energy level $\lambda_i = -E_0$ that will be considered as infinite in order to enforce the local constraint $n_{f,i} = 0$ if $i \notin \mathcal{K}$. This procedure is equivalent to introduce projection operators for the two different type of sites, as it was performed in Ref. [130]. It allows to describe $\mathcal{H}_i^0$ equally for Kondo and Non-Kondo sites with the same matrix form:

$$\mathcal{H}_i^0 = \sum_\sigma \begin{pmatrix} c_{i\sigma}^\dagger & f_{i\sigma}^\dagger \end{pmatrix} \begin{pmatrix} -\mu & r_i \\ r_i & -\lambda_i \end{pmatrix} \begin{pmatrix} c_{i\sigma} \\ f_{i\sigma} \end{pmatrix} \tag{7.20}$$

Here:

$$\begin{matrix} r_i = 0 \\ \lambda_i = -E_0 \end{matrix} \text{ , if } i \notin \mathcal{K}. \tag{7.21}$$

In the following we study only non-magnetic phases. We can thus consider an effective spin-less problem and the index σ is dropped in the remaining of this chapter.

Defining $\mathbf{g}_{ii}(i\omega_n)$ as the matrix Green's function for the local term $\mathcal{H}_i^0$, we have:

$$\mathbf{g}_{ii}(i\omega_n) = \begin{pmatrix} g_{ii}^{cc}(i\omega_n) & g_{ii}^{cf}(i\omega_n) \\ g_{ii}^{fc}(i\omega_n) & g_{ii}^{ff}(i\omega_n) \end{pmatrix} = \left[i\omega_n \mathbf{I} - \mathcal{H}_i^0\right]^{-1} \tag{7.22}$$

Here $\mathbf{I}$ is the 2×2 identity matrix. The matrix inversion leads to the explicit form of $\mathbf{g}_{ii}(i\omega_n)$:

$$\mathbf{g}_{ii}(i\omega_n) = \begin{pmatrix} \frac{1}{i\omega_n + \mu - \frac{r_i^2}{i\omega_n + \lambda_i}} & \frac{r_i}{(i\omega_n+\mu)(i\omega_n+\lambda_i) - r_i^2} \\ \frac{r_i}{(i\omega_n+\mu)(i\omega_n+\lambda_i) - r_i^2} & \frac{1}{i\omega_n + \lambda_i - \frac{r_i^2}{i\omega_n+\mu}} \end{pmatrix} \tag{7.23}$$

7.2.2 Hopping expansion

We perform an infinite expansion of the hybridization function (sometimes called *self-energy*[3]) associated with the electronic hopping[143]. The suitable expansion is given by the Feenberg's perturbation theory[144] largely discussed in the context of Anderson localization[145, 146].

The hybridization function $\Delta_i(i\omega_n)$ describes processes where a conduction electron hops out the initial site i, move through a given path in the lattice and returns to the initial site in the end. For convenience, we define it in the matrix form

$$\mathbf{\Delta}_i(i\omega_n) = \begin{pmatrix} \Delta_i(i\omega_n) & 0 \\ 0 & 0 \end{pmatrix}, \tag{7.24}$$

so that we can write the full Green's functions $\mathbf{G}_{ii}(i\omega_n)$ (also in a matrix form) as:

$$\mathbf{G}_{ii}(i\omega_n) = \left[(\mathbf{g}_{ii}(i\omega_n))^{-1} - \mathbf{\Delta}_i(i\omega_n)\right]^{-1} \tag{7.25}$$

Explicitly:

$$\mathbf{G}_{ii}(i\omega_n) = \begin{pmatrix} \frac{1}{i\omega_n+\mu-\frac{r_i^2}{i\omega_n+\lambda_i}-\Delta_i(i\omega_n)} & \frac{r_i}{(i\omega_n+\mu-\Delta_i(i\omega_n))(i\omega_n+\lambda_i)-r_i^2} \\ \frac{r_i}{(i\omega_n+\mu-\Delta_i(i\omega_n))(i\omega_n+\lambda_i)-r_i^2} & \frac{1}{i\omega_n+\lambda_i-\frac{r_i^2}{i\omega_n+\mu-\Delta_i(i\omega_n)}} \end{pmatrix} \tag{7.26}$$

The expansion of $\Delta_i(i\omega_n)$ for an arbitrary lattice is presented in Appendix F. Here we restrict ourselves to the results obtained for a Bethe lattice. A Bethe lattice [4] is a loop-free network characterized only by its coordination number Z, as shown in Figure 7.3. We also consider that all the nearest-neighbors hoppings are equal ($t_{ij} = t$, for all pair of neighbors i, j), disregarding the type of sites (Kondo or non-Kondo).

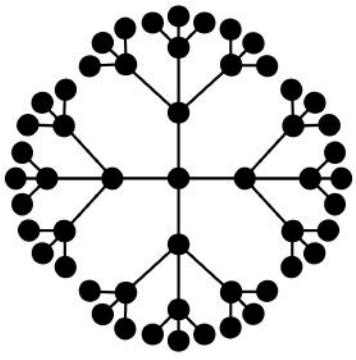

Figure 7.3: Finite representation of a $Z = 4$ Bethe lattice.

[3]We adopt the former denomination to link it to Dynamical Mean-Field Theory[142], where *hybridization function* is used for the same quantity.

[4]We refer to Appendix C for additional results on the Bethe lattice, including the analytical expression of the non-interacting density of states.

Given that loops are absent, there is only one path connecting two different sites in this lattice and the expansion in Equation F.7 contains only the first term. The equation obtained for $\Delta_i(i\omega_n)$ is (Eq. F.11):

$$\Delta_i(i\omega_n) = t^2 \sum_{j \neq i}^{Z} G_{jj}^{cc\,(i)}(i\omega_n), \tag{7.27}$$

The sum extends over the Z neighbors of i (Z is the lattice coordination number). $G_{jj}^{cc\,(i)}(i\omega_n)$ is the Green's function in the site j *with the site* i *removed*, or a *cavity Green's function*, having a similar form as $G_{ii}^{cc}(i\omega_n)$:

$$G_{jj}^{cc\,(i)}(i\omega_n) = \frac{1}{i\omega_n + \mu - \frac{r_j^2}{\omega + \lambda_j} - \Delta_{jj}^{(i)}(i\omega_n)} \tag{7.28}$$

The hybridization function $\Delta_j^{(i)}(i\omega_n)$ for the cavity Green's function $G_{jj}^{cc\,(i)}(i\omega_n)$ (given by Eq. 7.28) has a similar structure (see Figure 7.4):

$$\Delta_j^{(i)}(i\omega_n) = t^2 \sum_{k \neq j,i}^{Z-1} G_{kk}^{cc\,(j)}(i\omega_n), \tag{7.29}$$

although the sum extends over $Z-1$ terms only. Note that in the Bethe lattice all the "higher-orders" cavity Green's functions and their hybridization functions have exactly the same form as $G_{jj}^{cc\,(i)}(i\omega_n)$ and $\Delta_j^{(i)}(i\omega_n)$.

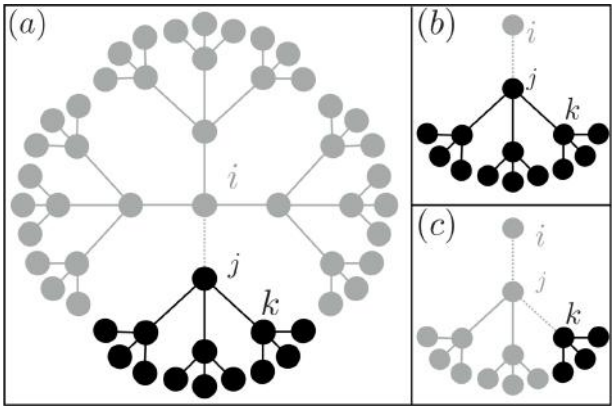

Figure 7.4: Schematic diagram of the hopping expansion in a $Z = 4$ Bethe lattice. **(a)** Starting from the central site i, the hybridization function $\Delta_i(i\omega_n)$ is written in terms of the Green's functions of its Z neighbouring sites with the central site excluded (the cavity Green's functions). In this procedure, the branch labeled by its first site j (highlighted in **(b)**) is separated from the others.**(c)** The cavity hybridization function $\Delta_j^{(i)}(i\omega_n)$ is obtained in the same manner, except that it is a sum over $Z-1$ sub-branches, labeled by k.

7.3 Statistical DMFT

The statistical DMFT is a variation of Dynamical Mean-Field Theory adapted to treat disordered problems. The idea is to map an interacting fermionic problem in a disordered lattice to an *ensemble* of single impurity problems embedded in their own self-consistent baths. The self-consistency is taken in the statistical distribution of baths, which is obtained from an algorithm that generates it iteratively. This method was introduced by Dobrosavljevic and Kotliar [147, 148, 149] for the Hubbard model with a disordered local energy in the context of the Mott-Anderson metal-insulator transition.

In all following, the Bethe lattice will be considered. Let us take some results from the last section to explain the method. Supposing that the site i is a Kondo site. Its Green's function is given by the matrix Eq.7.26 and

$$G_{ii}^{cc}(i\omega_n) = \frac{1}{i\omega_n + \mu - \frac{r_i^2}{\omega+\lambda_i} - t^2 \sum_{j\neq i}^{Z} G_{jj}^{cc\,(i)}(i\omega_n)}, \tag{7.30}$$

where the sum over j is taken on the Z nearest neighbors of site i.Here we have written explicitly the hybridization function $\Delta_i(i\omega_n)$ from Eq.7.27. The cavity Green's function $G_{jj}^{cc\,(i)}(i\omega_n)$ are given by (using Eq.7.28 and 7.29)

$$G_{jj}^{cc\,(i)}(i\omega_n) = \frac{1}{i\omega_n + \mu - \frac{r_j^2}{\omega+\lambda_j} - t^2 \sum_{k\neq j,i}^{Z-1} G_{kk}^{cc\,(j)}(i\omega_n)}, \tag{7.31}$$

where the sum over k is taken on the $Z-1$ nearest neighbors of j, having excluded site i (see Figure 7.4).

Since we are dealing with a disordered problem, we expect that local quantities as $G_{ii}^{cc}(i\omega_n)$ will follow some distribution (unknown, in principle) and our goal is to determine them. This is done in the statistical DMFT by considering Eq. 7.31 above as a *self-consistent equation for the distribution of cavity Green's functions*. This idea was first considered by Abou-Chacra, Anderson and Thouless [146] for non-interacting electrons in their self-consistent treatment of disorder, discussed in the context of Anderson localization. The statistical DMFT then is a generalization of their approach for interacting problems.

We remind that the method presented here is *exact* for a Bethe lattice of any coordination number Z. Approximations in this work are performed in two different levels. The first one is the solution of the local Kondo problem[5] in a mean-field approximation. The second one takes place when we sample the distribution of cavity Green's functions by a numerical procedure, which introduces statistical errors.

In the next section we will show a numerical procedure to implement a stochastic method that achieves the convergence from the self-consistent relation in Eq.7.30 for finite Z.

[5]The solution of the single impurity Anderson model is required in the general case.

Numerical procedure

Let us concentrate now on the numerical procedure that implements the statistical DMFT. The key point lies in the iterative procedure to generate new cavity hybridization functions (or *cavity baths*) from the cavity Green's functions in the last step of iteration, as it is mathematically described in Eq. 7.31.

For clarity purposes, we discuss separately the parts containing the self-consistent calculation for the Fermi level and how the statistics are made. The numerical implementation core is the following[6]:

1. Enter an initial guess for the cavity baths $\Delta_i^{(0)}(i\omega_n)$. A good approach to speed up convergence is to use an ansatz that interpolates between its value on the lattice ($x = 1$) and the impurity ($x \to 0$):

$$\Delta_i^{(0)}(i\omega_n) = x\Delta_{i,\mathrm{Lattice}}^{(0)}(i\omega_n) + (1-x)\Delta_{i,\mathrm{Impurity}}^{(0)}(i\omega_n).$$

   These quantities are easily computed for a given J_K and Z. For instance, $\Delta_{i,\mathrm{Impurity}}^{(0)}(i\omega_n)$ is the same as in the non-interacting problem and its expression is given in Eq. C.7.

2. Solve xN_{site} mean-field equations numerically for every Kondo site of the ensemble using the baths $\Delta_i^{(0)}(i\omega_n)$. The mean-field equations for r_i and λ_i (Eqs. 7.15 and 7.16) can be written as:

$$\frac{2}{\pi}\int_0^{+\infty} d\omega \mathrm{Re}\left[\frac{1}{\omega + \lambda_i - \frac{r_i^2}{\omega+\mu-\Delta_i^{(0)}(\omega)}}\right] = 0 \tag{7.32}$$

$$-\frac{1}{\pi}\int_0^{+\infty} d\omega \mathrm{Re}\left[\frac{1}{(\omega+\mu-\Delta_i^{(0)}(\omega))(\omega+\lambda_i) - r_i^2}\right] = 1 \tag{7.33}$$

   After that, update the cavity Green's functions with the mean-field parameters and the cavity baths.

3. Generate new cavity baths from the previous ones from the following procedure:

   (a) Creates $Z-1$ copies of each cavity Green's function from the previous step $G_{ii}^{(0)}$. The system will have $(Z-1)N_{sites}$ sites after this step.

   (b) For a given site $j(=1,...,N_{sites})$, pick up randomly $Z-1$ functions $G_{jj}^{(0)}$ and compute the new cavity baths as:

$$\Delta_i^{(0)}(\omega) = t^2 \sum_j^{Z-1} G_{jj}^{(0)}(\omega) \tag{7.34}$$

[6] In this subsection we employ the notation from Appendix C for the cavity Green's function ($G_{ii}^{cc\,(0)}$) and hybridization function ($\Delta_i^{(0)}(\omega)$), instead of $G_{jj}^{cc\,(i)}$ and $\Delta_j^{(i)}$. The reason is to avoid misleading idea that the sampling procedure is performed in a real lattice for a fixed disorder realization.

4. Go back to step 2 using $\Delta_i^{(0)}(\omega)$ as baths. Proceed by iteration until you achieve the statistical convergence of $\Delta_i^{(0)}(\omega)$.

5. *After the convergence:* The last step is to get $\Delta_j(\omega)$ from $\Delta_j^{(0)}(\omega)$. It corresponds in our construction to Eq. 7.30. It is done by the step 3 above, but now copying Z times each function and combining Z functions to construct $\Delta_j(\omega)$.

6. Store all the local quantities whose statistics will be analyzed.

In Figure 7.5 we illustrate the statistical DMFT procedure, in particular, the generation of random cavity baths is described in the diagram on the bottom.

The determination of the Fermi level is based on the requirement that the average number of conduction electrons *per site* is fixed at a given value n_c, which is calculated using Eq.D.8:

$$n_c = 2\sum_i < c_i^\dagger c_i >= 2\sum_i G_{ii}^{cc}(\tau = 0^-) \tag{7.35}$$

Since it is a disordered system, in principle each site has a different occupation and the average value varies at each iteration, due to statistical fluctuations inherent to the method. Then the criterion to achieve a self-consistent value for the Fermi energy must be loose enough to account for these fluctuations. In all the results in the next chapter we have taken as numerical error 0.01 and the chemical potential is determined for a n_c fixed to a given value ± 0.01.

The numerical procedure to perform reliable statistical analysis is based on an artifact to increase the sample size. The number of sites N_{site} increases the computational time in two ways: the number of impurity problems to be solved at each iteration is proportional to N_{site}, as it is the size of arrays that store the local quantities numerically[7]. Then the following trick is proposed: instead of using a large array and compute the statistics at the end of the final iteration, we gather data in N_{stat} iterations counted after the convergence is achieved. So we effectively sample $N_{site} \times N_{stat}$ different sites.

[7] In practice we are constrained to use $N_{site} = 10^4 - 10^5$ in a serial implementation on a PC.

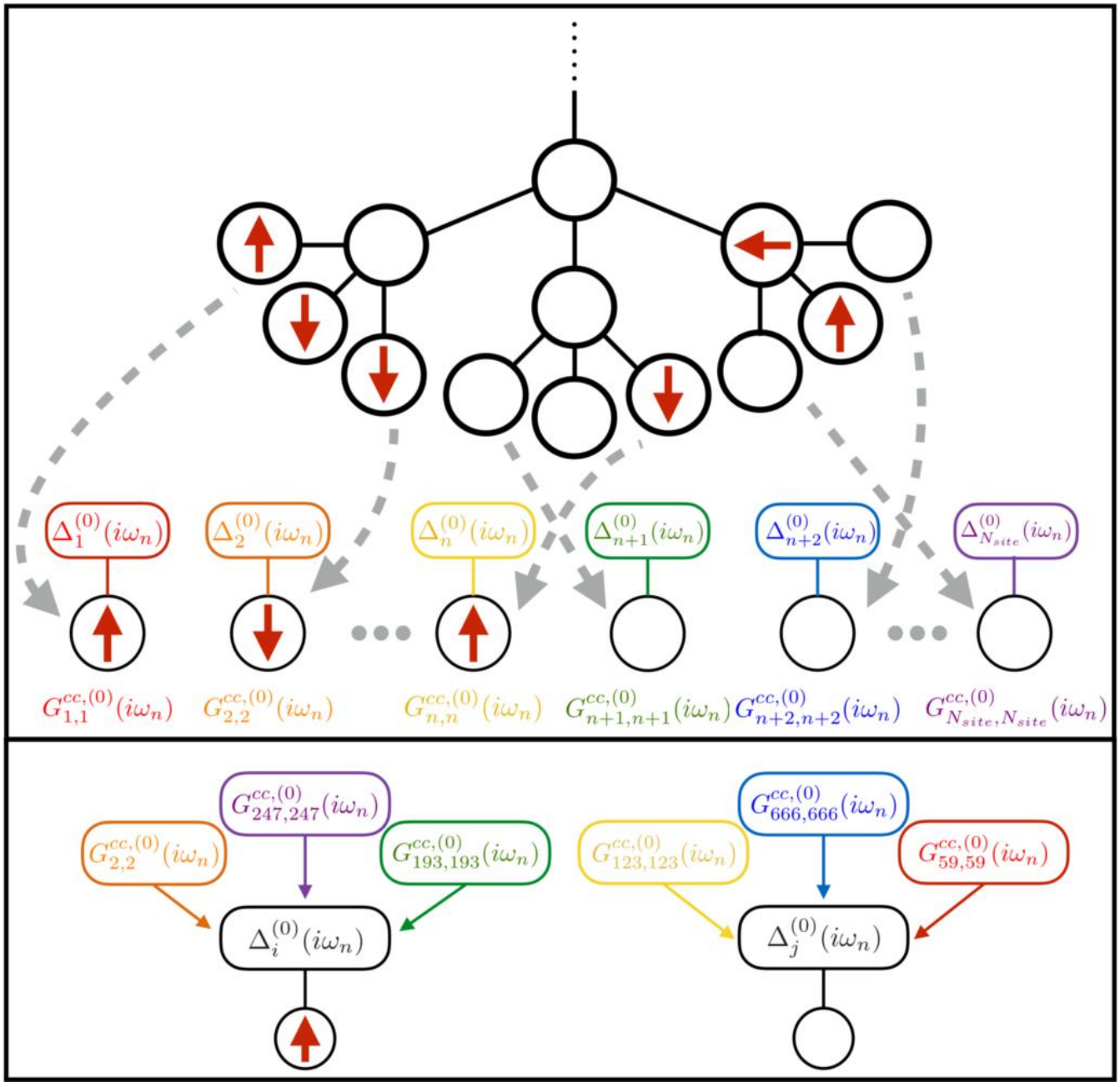

Figure 7.5: Illustration of Statistical DMFT procedure for $Z = 4$ Bethe lattice. **Top:** The disordered interacting problem in the lattice (represented by a single branch) is replaced by an ensemble of single site problems in which the local environment is encoded by the bath functions $\Delta_i^{(0)}(i\omega_n)$. The cavity Green's functions $G_{ii}^{cc,(0)}(i\omega_n)$ are obtained after the solution of xN impurity problems. **Bottom:** New bath functions are constructed from the random combination of Z–1 cavity Green's functions. The iteration stops when convergence is achieved for the $G_{ii}^{cc,(0)}(i\omega_n)$ probability distribution.

7.4 Summary

In Chapter 7 we have introduced the Kondo Alloy model (KAM) hamiltonian (Eq. 7.1). The formalism employed to study this model is the Statistical DMFT described in Section 7.3, which is a generalization of the standard DMFT procedure designed for disordered problems. The core of Statistical DMFT is to map an interacting problem in a disordered lattice in a large ensemble of Anderson Impurity (Section 1.1.1) problems with different hybridization functions, whose probability distribution through the lattice sites is obtained self-consistently. The self-consistent procedure is implemented numerically, as discussed in Section 7.3. In the next chapter some results obtained for the KAM using statistical DMFT will be presented.

Chapter 8

Results

In this chapter we will present some results for the Kondo Alloy model obtained from the statistical DMFT calculations described in the last chapter. The statistical feature of the method implies that *distributions* of local quantities are the central results. This chapter is organized as follows. In Section 8.1 we present the relevant quantities to be used in the discussion of our results. Section 8.2 contains an analysis of the system behavior as a function of x in the strong and weak coupling regimes. Finally, in Sections 8.3 and 8.4 we discuss the influence of different local environments and we address the issues of low dimensionality, respectively.

8.1 Important quantities and their distributions

Let us start by presenting some local quantities whose distributions will be analyzed in this chapter. I start by the two local mean-field parameters r_i^2 and λ_i. The first parameter measures the degree of hybridization between c and f electrons (Equation 7.9) and is related to the Kondo coupling J_K. The second parameter is the position of the f level with respect to the Fermi energy, computed self-consistently from the local constraint (Equation 7.8).

Both parameters come from the solution of the mean-field equations (the "impurity solver") in every Kondo site of the problem. Its implementation is explained in Section 7.2. For the numerical calculations we have used standard subroutines to solve non-linear equations (by the bisectional method) and numerical integration. Energy scales are all normalized to the half-bandwidth D of the non-interacting electrons in a Bethe lattice with fixed Z, given by $D = 2\sqrt{Z-1}t$.

In Figure 8.1 the distributions of r_i^2 and λ_i are shown as examples. In these plots we have fixed the local moments concentration to $x = 0.1$, the electronic filling to $n_c = 0.5$ and the Kondo interaction to $J_K = D$ and the calculation was performed using a $Z = 5$ Bethe lattice. The first notable feature of these distributions is that they are often multi-modal, as it can be seen for the distribution of λ_i. Due to this complex form, we cannot characterize these distributions by invoking only their first statistical moments (average and standard deviation). As it will be shown in the following, this multipeaked structure results from the different

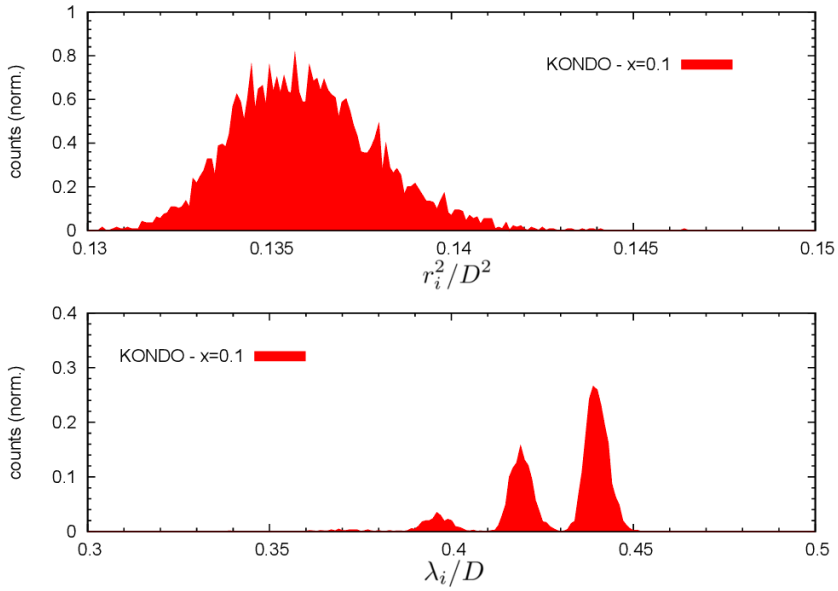

Figure 8.1: Distribution of the mean-field parameters r_i^2(top) and λ_i(bottom) in the Kondo sites with concentration $x = 0.1$. Other parameters are $J_K = D$, $n_c = 0.5$ and $Z = 5$.

environments that the local moments may have in the disordered system (this will be discussed in Section 8.3).

The next group of quantities of interest are the local densities of states, or more specifically, their values at the Fermi level. The local density of states (LDOS) is defined as:

$$\rho_i^{\alpha}(\omega) = -\frac{1}{\pi}\mathrm{Im}G_{ii}^{\alpha\alpha}(i\omega_n = \omega + i0^+) \tag{8.1}$$

An analytical continuation must be performed in the right hand side of the equation above, in order to obtain the retarded Green's function. The index α holds for the two types of electronic Green's functions (c and f). If i is a Non-Kondo site, the f-part of the LDOS is zero by definition. Apart from the partial LDOS $\rho_i^c(\omega)$ and $\rho_i^f(\omega)$, it is desirable in what follows to consider the *total* LDOS $\rho_i^{tot}(\omega) = \rho_i^c(\omega) + \rho_i^f(\omega)$. Instead of analyzing the distributions of the density of states for different frequencies, we will restrict ourselves to values at the Fermi energy ($\omega = 0$) through this chapter. In order to avoid the analytical continuation, we approximate $\rho_i^{\alpha}(0)$ by using the lowest Matsubara's (imaginary) frequency taken in our problem, which is $0.001D$. This procedure is correct as long as the Kondo temperature satisfies $T_K > 0.001D$, which is the case for the J_K values used in this work (for further details on T_K, see Section 8.2).

In Figure 8.2 the distribution of density of states $\rho_i^c(0)$(top), $\rho_i^f(0)$ (center) and $\rho_i^{tot}(0)$ (bottom) at the Fermi level are shown for the same parameters as in Figure 8.1. The distributions of ρ_i for Kondo and Non-Kondo sites are represented separately by solid and hatched patterns, respectively, and the horizontal axis scale is given in terms of the half bandwidth of non-interacting conduction electrons.

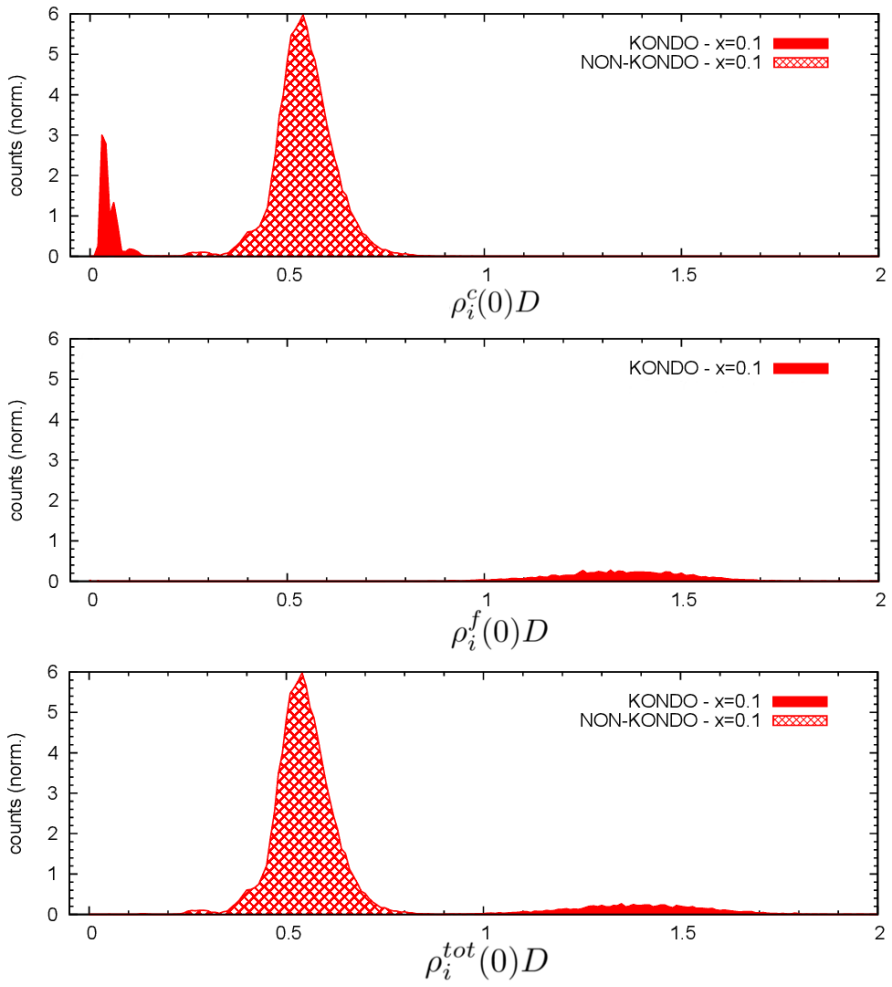

Figure 8.2: Distribution of the local density of states $\rho_i^c(0)$(top), $\rho_i^f(0)$ (center) and $\rho_i^{tot}(0)$ (bottom). Kondo and Non-Kondo sites distributions are plotted separately. Parameters are $J_K = D$, $x = 0.1$, $n_c = 0.5$ and $Z = 5$.

In the top figure of Fig. 8.2, $\rho_i^c(0)$ is distributed very close to zero for Kondo sites because conduction electrons in these sites are participating in the screening of local moments through Kondo effect (as already indicated by the distribution of r_i) and electronic excitations cost a large energy. For Non-Kondo sites the distribution is peaked at a finite value close to 0.5, indicating that conduction electrons in this sublattice have excitations close to the Fermi energy as in the non-interacting case. The value $\rho_i^c(0)D \approx 0.5$ is close to the value in the middle of the non-interacting DOS for $Z = 5$ Bethe lattice (see Figure C.1). The values of $\rho_i^f(0)$ (middle figure in Fig. 8.2) for Kondo sites are distributed around the value 1.2. This quantity roughly corresponds to the Kondo peak height and it is inversely proportional to the Kondo temperature.

ϕ-function

Another important quantity that will be largely discussed in this chapter is the function $\phi_i(\omega)$, defined by the relation:

$$G_{ii}^{cc}(\omega) \equiv G_0(\omega - \phi_i(\omega)) \tag{8.2}$$

Here $\phi_i(\omega)$ is employed to relate the site dependent c-electron Green's function $G_{ii}^{cc}(\omega)$ to the free electron Green's function in a Bethe lattice $G_0(\omega)$, which has an analytic expression (Eq. C.9):

$$G_0(\omega) = \frac{(Z-2)\omega - Z\omega\sqrt{1 - \frac{4t^2(Z-1)}{\omega^2}}}{2\left(Z^2t^2 - \omega^2\right)} \tag{8.3}$$

Using the reciprocal function of G_0, $R\left[G^0(\omega)\right]$(Eq. C.12), we have:

$$\omega - \phi_i(\omega) = R\left[G_{ii}^{cc}(\omega)\right] \tag{8.4}$$

$\phi_i(\omega)$ is a complex function defined as:

$$\phi_i(\omega) = \omega + \left(\frac{Z-2}{2G_{ii}^{cc}(\omega)}\right) - \left(\frac{Z}{2G_{ii}^{cc}(\omega)}\right)\sqrt{1 + 4t^2\left(G_{ii}^{cc}(\omega)\right)^2} \tag{8.5}$$

Let us restrict ourselves to the analysis of this quantity at the Fermi energy. $\phi_i(\omega = 0)$ is a complex number. The interpretation is the following[1]: the real part of $\phi_i(0)$ can be thought as an effective position of the conduction electron level with respect to the non-interacting density of states. The latter is bounded in the interval $[-D; D]$, since the energy scale is the half-bandwidth of the non-interacting problem. Then, if $\mathrm{Re}[\phi_i(0)]$ belongs to this interval for a given site, it means that the local electronic level lies in a region with a non-zero density of states for conduction electrons and the conduction electrons have an itinerant behavior. On the other hand, if $\mathrm{Re}[\phi_i(0)]$ lies outside the interval $[-D; D]$, the f-level energy lies outside the conduction band, being almost localized since the hybridization effect on it is small. This localization is reminiscent of a Kondo insulating state (from a local point of view), even if the system is neither periodic nor half-filled.

The interpretation to $\mathrm{Re}[\phi_i(0)]$ described above is exemplified in Figure 8.3. It represents the dilute regime of the Kondo Alloy ($x = 0.1$ and $n_c = 0.5$). In that case, the conduction electrons in Kondo sites form local singlets with the local moments, "pushing" the effective level to lower values and $\mathrm{Re}[\phi_i(0)] < -D$. The conduction electrons engaged in these bound states are blocked and do not contribute to the low-energy excitations. The remaining electrons are free to move in the depleted lattice of Non-Kondo sites, which is represented by values of $\mathrm{Re}[\phi_i(0)]$ lying inside the non-interacting conduction band. The quasiparticles in the system are the conduction electrons in Non-Kondo sites and their existence guarantees the metallic behavior of the system.

For completeness we also show in Fig. 8.3 the imaginary part of $\phi_i(0)$ in order to establish that $\phi_i(\omega)$ cannot be interpreted as the "local self-energy" of the interacting disordered problem. Our claim is based on the numerical finding that $\mathrm{Im}[\phi_i(0)]$ can assume positive values,

[1] In Appendix E $\phi_i(\omega)$ is shown in two limiting cases in which it has a simpler interpretation.

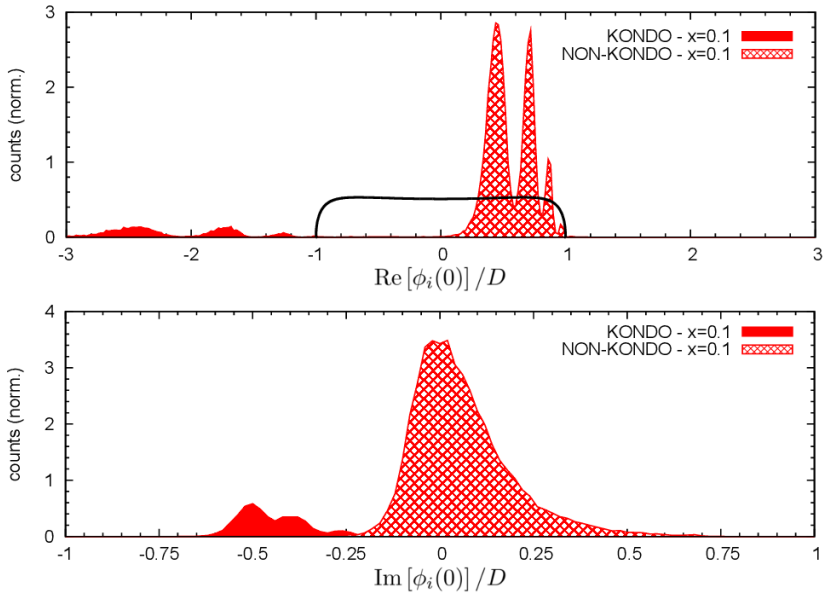

Figure 8.3: Distribution of the real (top) and imaginary (bottom) parts of $\phi_i(\omega)$ at the Fermi level. The value of parameters are $J_K = D$, $x = 0.1$ and $n_c = 0.5$.

while for a self-energy the relation $\mathrm{Im}[\Sigma(\mathbf{k},\omega)] \leq 0$ must be fulfilled to respect causality [3, 2]. But even if $\mathrm{Im}[\phi_i(0)]$ can be positive, the local density of states $\rho_i^c(0)$ remains non-negative in all cases. In Appendix E we present the expression for $\mathrm{Im}[\phi_i(0)]$ in the $Z \to \infty$ limit and we discuss the origin of such sign.

8.2 Concentration effects

Let us now present the results concerning the evolution of the distributions introduced in Section 8.1 as a function of the local moments concentration x. We consider two regimes, depending on the strength of Kondo interaction: the strong coupling and weak coupling case. A qualitative criterion to distinguish both regimes is given by the comparison between the analytical expression for the Kondo temperature (Eq.1.1.2) and its numerical estimative from the mean-field parameter r^2.The single impurity Kondo temperature follows the exponential formula $T_K = D\exp\left(-1/\rho_0^c(\mu)J_K\right)$ only in the weak coupling case. In the strong coupling case, T_K is proportional to J_K, which is the energy required to break the singlet state between one conduction electron and the impurity spin.

Since our mean-field calculations are done at zero temperature, we can estimate numerically its value from the mean-field parameter r^2_{imp} for the single impurity case. We compare it to $T_K^{(1)} = D\exp\left(-1/\rho_0^c(\mu)J_K\right)$, computed from the non-interacting density of states for the Bethe lattice (Figure C.1) with $Z = 5$. This expression of T_K gives a rough estimate of the Kondo temperature when J_K is small. Nevertheless Figure 8.4 shows the dependence of the ratio $(r^2_{imp}/D)/T_K^{(1)}$ for a single impurity as a function of J_K for a $Z = 5$ Bethe lattice with a

concentration $n_c = 0.5$ of conduction electrons. The ratio remains close to one for $J_K \leq 1$, indicating the limit of the weak coupling case. For a comparison, we present the ratio r^2_{imp}/J^2_K in the inset of Figure 8.4, which approaches its maximum value $r^2_{imp}/J^2_K = 1/4$ for large J_K. This value corresponds to the local average $< f^\dagger_{i\sigma} c_{i\sigma} >^2$ calculated for strong J_K.

Summarizing the discussion above, we will consider from now on as the weak coupling regime $J_K \lesssim D$ and the strong coupling regime $J_K \gtrsim 3D$.

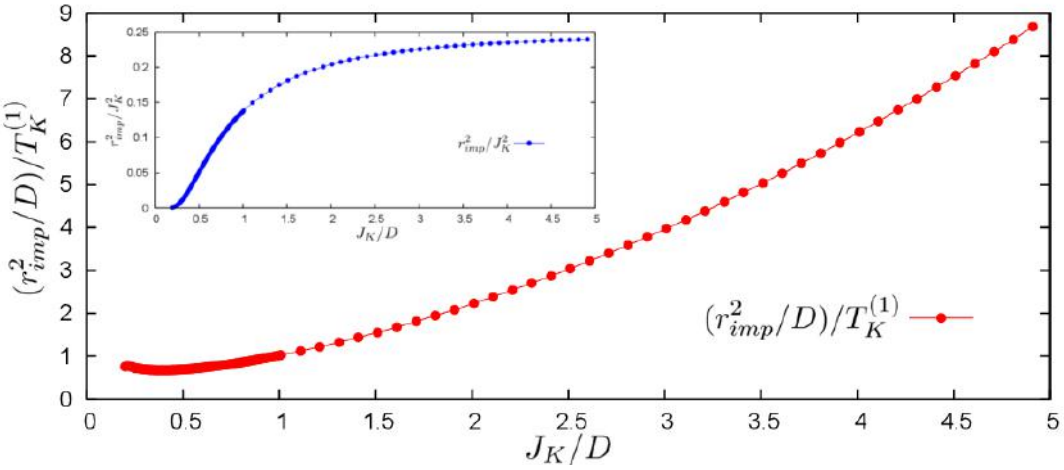

Figure 8.4: Energy scales of the single impurity Kondo problem in mean-field approximation. The ratio $(r^2_{imp}/D)/T^{(1)}_K \approx 1$ sets the weak coupling regime. In the inset, the ratio r^2_{imp}/J^2_K is shown. The strong coupling regime occurs when $r^2_{imp}/J^2_K \approx 1/4$. Results for a $Z = 5$ Bethe lattice with $n_c = 0.5$.

Let us now present the first results obtained from the statistical DMFT method. We start by the average value of the mean-field parameter r^2_i/J^2_K (or $< f^\dagger_{i\sigma} c_{i\sigma} >^2$, from Eq. 7.9) as a function of x computed in the strong ($J_K = 5D$) and the weak ($J_K = D$) coupling cases (Figure 8.5). In the strong coupling case, $\langle r_i \rangle^2 / J^2_K$ is almost a constant (close to $1/4$, its maximum value) for $x \leq n_c$, decreasing for $x > n_c$ until its reaches its minimum value in the lattice case ($x = 1$). For $J_K = D$, the average $\langle r_i \rangle^2 / J^2_K$ slightly decreases from the impurity ($x = 0.001$) to the lattice ($x = 1$) case and the change at $x = n_c$ is not visible. The strong coupling result is similar to those presented in Figure 7.1, which are obtained in a combination of mean-field approximation for the Kondo interaction and exact diagonalization in a square lattice[131]. The Figure 8.5 displays a general trend that will be seen in the following sections, namely a clear change in the system behavior at $x = n_c$, which is noticeable only when the Kondo interaction is sufficiently large.

8.2.1 Strong Coupling

In Section 6.1 it was discussed two well-known limits of the Kondo Alloy problem: the single impurity and the Kondo lattice. In the single impurity case, the physics at low T is dominated by the strong coupling fixed point($J_K \to \infty$). The Kondo lattice limit is characterized by a rich

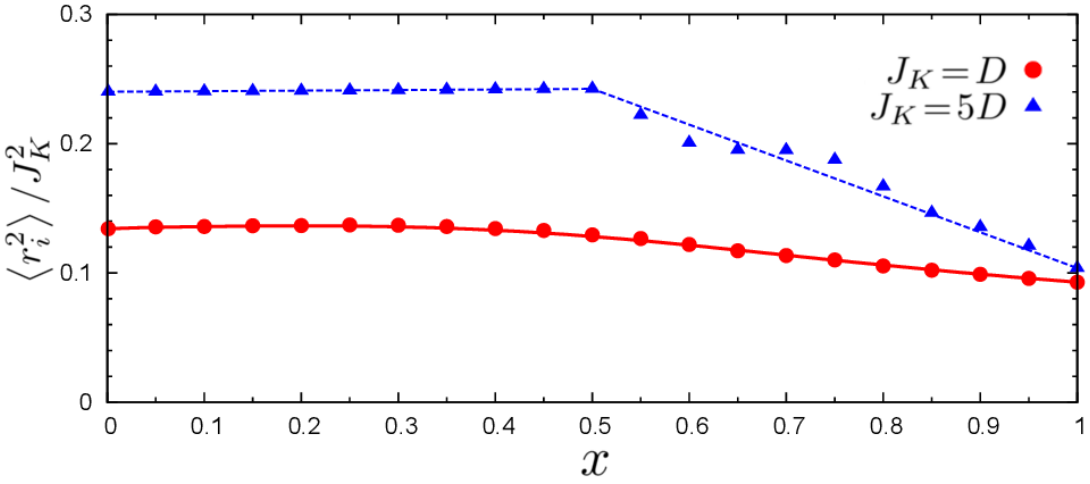

Figure 8.5: Average value of the mean field parameter r_i^2 as a function of x for $J_K = D$ (red circles) and $J_K = 5D$ (blue triangles). A kink is observed at $x = n_c$ ($n_c = 0.5$).

phase diagram where the Fermi liquid Kondo phase compete with RKKY dominated phases (see the Doniach diagram in Fig. 1.2). Here we consider only the FL ground states for the Kondo lattice regime. Besides, one of our motivations is to understand from numerical calculations the proposition of a "Lifshitz transition" done in Ref. [136] (Section 7.1.2), predicted in the strong coupling limit. Then, in this section we will discuss the possible signatures of this transition in terms of the statistics of local quantities and see if it is retained at smaller values of the Kondo parameter.

We focus on the the local density of states at the Fermi level. In Figure 8.6 we plot the distribution of the total density of states at the Fermi energy for different values of x and fixed $n_c = 0.5$. The distributions for Kondo and Non-Kondo sites are plotted separately in order to highlight the difference between the types of sites. For $x = 0.1$ ($x \ll n_c$) the distribution of $\rho_i^{tot}(0)$ has a peak close to $\rho_i^{tot}(0) = 0$ for Kondo sites and is distributed at finite values for Non-Kondo sites. This corresponds to the dilute regime of the model, where the Kondo sites are "locked" in singlet states while charge carriers can move almost freely on Non-Kondo sites. In this situation the Kondo sites locally behave as in an *insulator*.

By increasing the concentration of Kondo sites, assuming fixed n_c, the number of carriers in the lattice tends to reduce when x approaches n_c and the distribution of $\rho_i^{tot}(0)$ in Non-Kondo sites is broadened by this effect. For $x = n_c$ all the conduction electrons are located in Kondo sites and $\rho_i^{tot}(0) = 0$ is equal to zero for both Kondo and Non-Kondo sites. It corresponds to a Kondo Insulator regime exactly as predicted in Ref. [136]. Note that this state is more general than the insulating phase of the Kondo Lattice model at half-filling ($n_c = 1$), where periodicity creates a gap at the zone boundary and enhances the insulating behavior.

For $x = 0.9$ the distribution of $\rho_i^{tot}(0)$ for Kondo sites is located around $\rho_i^{tot}(0) \approx 1.2$, while the distribution for Non-Kondo sites is close to zero. This result indicates that the charge carriers are now moving in the sublattice of Kondo sites, while the Non-Kondo sites are empty, as it is expected from the analysis made in Section 7.1.2.

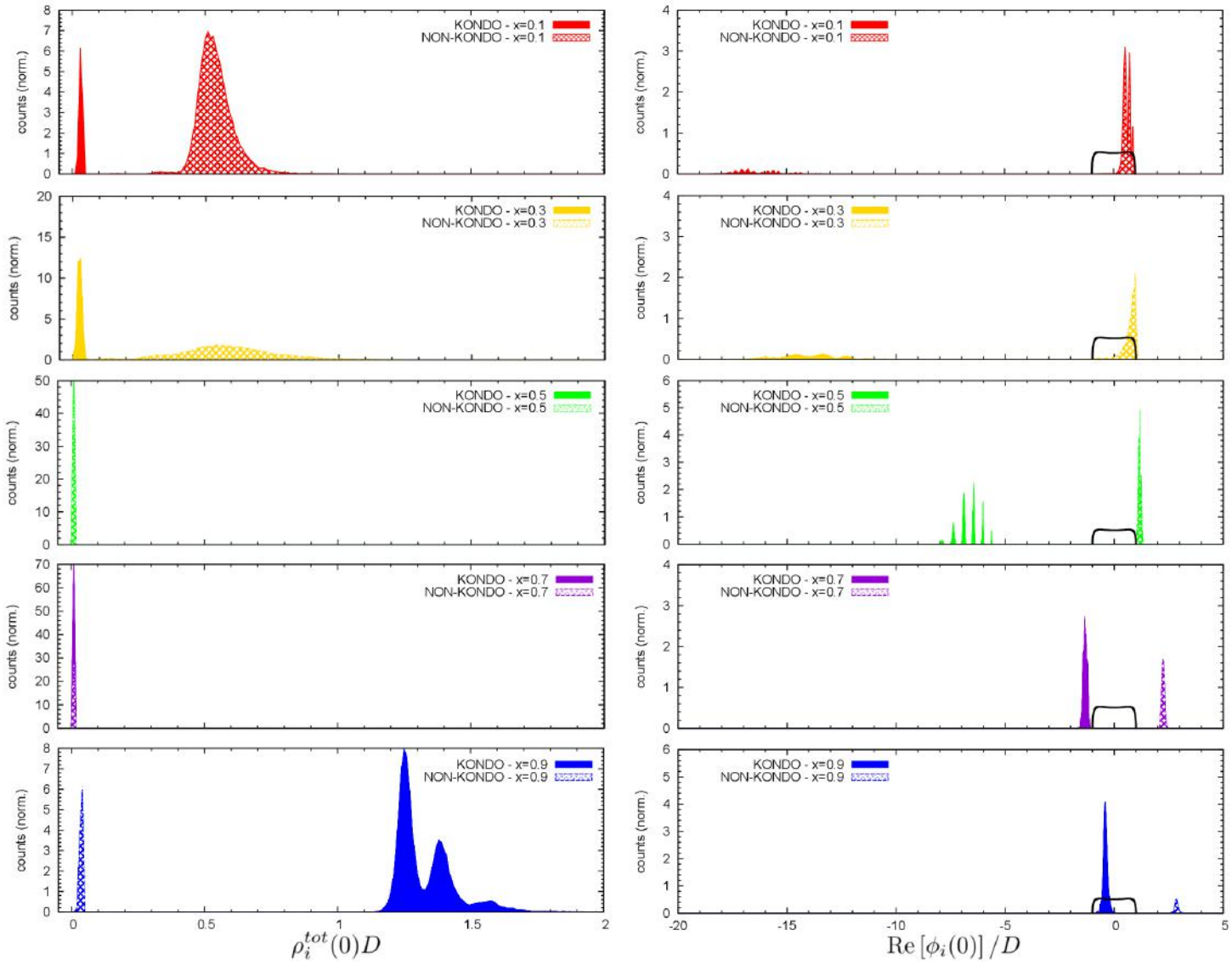

Figure 8.6: Distribution of the total density of states at the Fermi level in the strong coupling limit $J_K = 5D$. Five values of x are shown, ranging from 0.1 to 0.9, and the distributions are separated for Kondo (solid pattern) and Non-Kondo (hatched pattern) sites. The system evolves from a metallic state for Non-Kondo sites (*dilute regime*, $x = 0.1$ and 0.3), passing through an insulating state when $x \approx n_c$ ($x = 0.5$ and 0.7), and ends in a metallic state for Kondo sites (*concentrated regime*, $x = 0.9$).

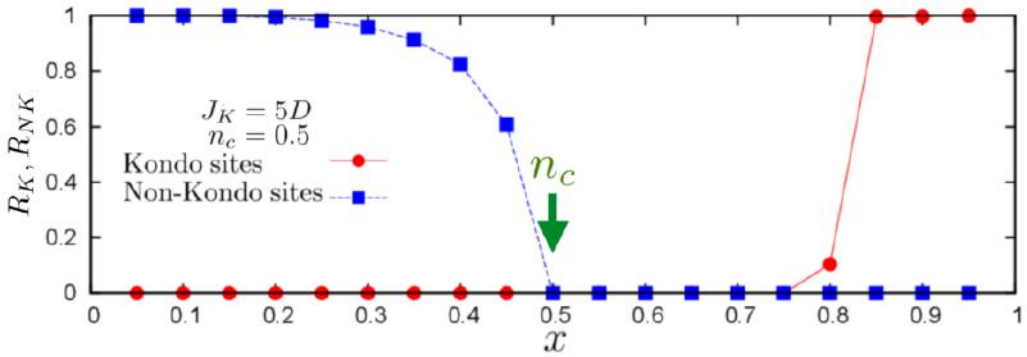

Figure 8.7: Concentration x dependence on the ratios of Kondo (red) and Non-Kondo (blue) sites in which $\mathrm{Re}\left[\phi_i(0)\right]$ lies inside the non-interacting conduction band. The point $x = n_c$ is marked by the vanishing ratio R_{NK} (Non-Kondo sites) when it is approched from the diluted side $x < n_c$. Both ratios are zero between $x = 0.5$ and $x \approx 0.75$, where the strong disorder and interactions leads to an insulating phase (see text). Other parameters are $J_K = 5D$ and $n_c = 0.5$ and lines are guides for the eyes.

The features depicted by the density of state can be further analyzed with respect to the function $\phi_i(0)$ introduced in Section 8.1. The sites in which the density of states are distributed at non-zero values have $|\mathrm{Re}\left[\phi_i(0)\right]| \leq D$, while for sites with $\rho_i^{tot}(0) \approx 0$ we have $|\mathrm{Re}\left[\phi_i(0)\right]| > D$.

Contrary to what happens in the $J_K \to \infty$ limit, the insulating regime is stable not only when $x = n_c$, but in a finite region around it. For instance, in Figure 8.6, an insulating phase is still observed at $x = 0.7$. Note that the insulating phase in not symmetric with respect to the point $x = n_c$, since at $x = 0.3$ the distribution is not peaked at zero and $|\mathrm{Re}\left[\phi_i(0)\right]| \leq D$ for Non-Kondo sites. The reason is the treatment of disorder by the Statistical DMFT employed here, in comparison to the treatment given by CPA and related methods.

One practical way to visualize the system dependence on the concentration x is to calculate the concentration of Kondo and Non-Kondo sites at which $|\mathrm{Re}\left[\phi_i(0)\right]| \leq D$, since it is an estimate of the fraction of sites containing extended states at the Fermi energy. Their formal definition are:

$$R_K = \frac{1}{xN} \sum_{i \in \mathcal{K}} \Theta\left(D - |\mathrm{Re}\left[\phi_i(0)\right]|\right) \tag{8.6}$$

$$R_{NK} = \frac{1}{(1-x)N} \sum_{i \notin \mathcal{K}} \Theta\left(D - |\mathrm{Re}\left[\phi_i(0)\right]|\right) \tag{8.7}$$

Here $\Theta(x)$ is the Heaviside function. In Figure 8.7 we plot the ratios R_K and R_{NK} as a function of the concentration x using the same parameters as in Figure 8.6. When $x < n_c$ the ratio R_{NK} is very close to unity, but it vanishes when $x = n_c$. Above this point the conduction electrons are all in the sublattice of Kondo sites. The ratio R_K is zero when $x < n_c$, since conduction electrons in Kondo sites are locked in singlets.

Remarkably the value of R_K is still zero above the transition point $x = n_c$ until $x \approx 0.8$. One would expect that the coherence effects should appear immediately at this point and R_K would increase with increasing x by the same reason as R_{NK} decreases at this point. This issue is related to a fundamental asymmetry between the diluted ($x < n_c$) and the concentrated ($x > n_c$) regime, indicating that the effective disorder seen by conduction electrons is larger in the concentrated case. Given that strong disorder leads to localization of electronic states (Anderson localization[145, 146]), it seems that two metal-insulator transitions occur, at $x = n_c = 0.5$ and at $x = 0.8$.This result, obtained only in the strong coupling regime, needs to be further studied.

8.2.2 Weak coupling

The strong coupling results serve as a bridge between our numerical calculations and the analytical considerations done in References [100, 96, 136], but it does not correspond to the physical limit. For that reason we further investigate concentration effects with a smaller Kondo interaction $J_K = D$. In Figure 8.8 we plot again the total density of states $\rho_i^{tot}(0)$ and $\mathrm{Re}\,[\phi_i(0)]$ for different concentrations of local moments, as in Figure 8.6. The electronic filling and the coordination number are fixed to $n_c = 0.5$ and $Z = 5$, respectively.

Firstly, we note that $\rho_i^{tot}(0)$ has a non-zero average value in any case, differently from the peaks $\rho_i^{tot}(0) \approx 0$ that appear in the strong coupling case. Since the Kondo effect is weaker here, the local singlets in Kondo sites are weakly bounded and the electronic states are never localized.

The distributions of $\mathrm{Re}\,[\phi_i(0)]$ show a smooth evolution from the diluted ($x \ll n_c$) to the concentrated ($x \gg n_c$) regime and we do not observe the "insulating phase" separating both regimes for $J_K = D$. Instead, at the point $x = n_c$ the distributions of $\mathrm{Re}\,[\phi_i(0)]$ are peaked near the band edges for both Kondo and Non-Kondo sites and there is a finite amount of sites for which $\mathrm{Re}\,[\phi_i(0)]$ is distributed inside the range $[-D; D]$. Considering the definition of $\mathrm{Re}\,[\phi_i(0)]$ (Eq. 8.2) and invoking the fact that the non-interacting Green's function G_0 is singular near the band edges, we may speculate that the presence of peaks at $\pm D$ for $\mathrm{Re}\,[\phi_i(0)]$ could lead to non-analyticities in the energy or temperature dependence of physical quantities, leading to Non-Fermi liquid behavior[150, 151, 152].

According to the discussion on Section 6.2.1 and references therein, an evidence for disorder-induced NFL behavior is a power-law distribution of Kondo temperatures, which gives a similar singularity in thermodynamical quantities. In Figure 8.9 the distribution of local Kondo temperatures is shown for $J_K = D$ and two local moment concentrations: $x = n_c = 0.5$ and $x = 0.9$. The local Kondo temperatures are obtained with the expression ($\rho_i^c(0)$ is the c-electrons local density of states)

$$T_{K_i} = D \exp\left(-\frac{1}{J_K \rho_i^c(0)}\right), \tag{8.8}$$

which is valid in the weak coupling regime. The statistical DMFT method provides the full distribution of $\rho_i^c(0)$ and, consequently, of T_{K_i}. Since the later has an exponential dependence, it is clear that it can be a broad distribution. For $x = n_c$, which marks the concentration region where NFL is expected from the analysis of Figure 8.8, a power-law distribution of T_{Ki}

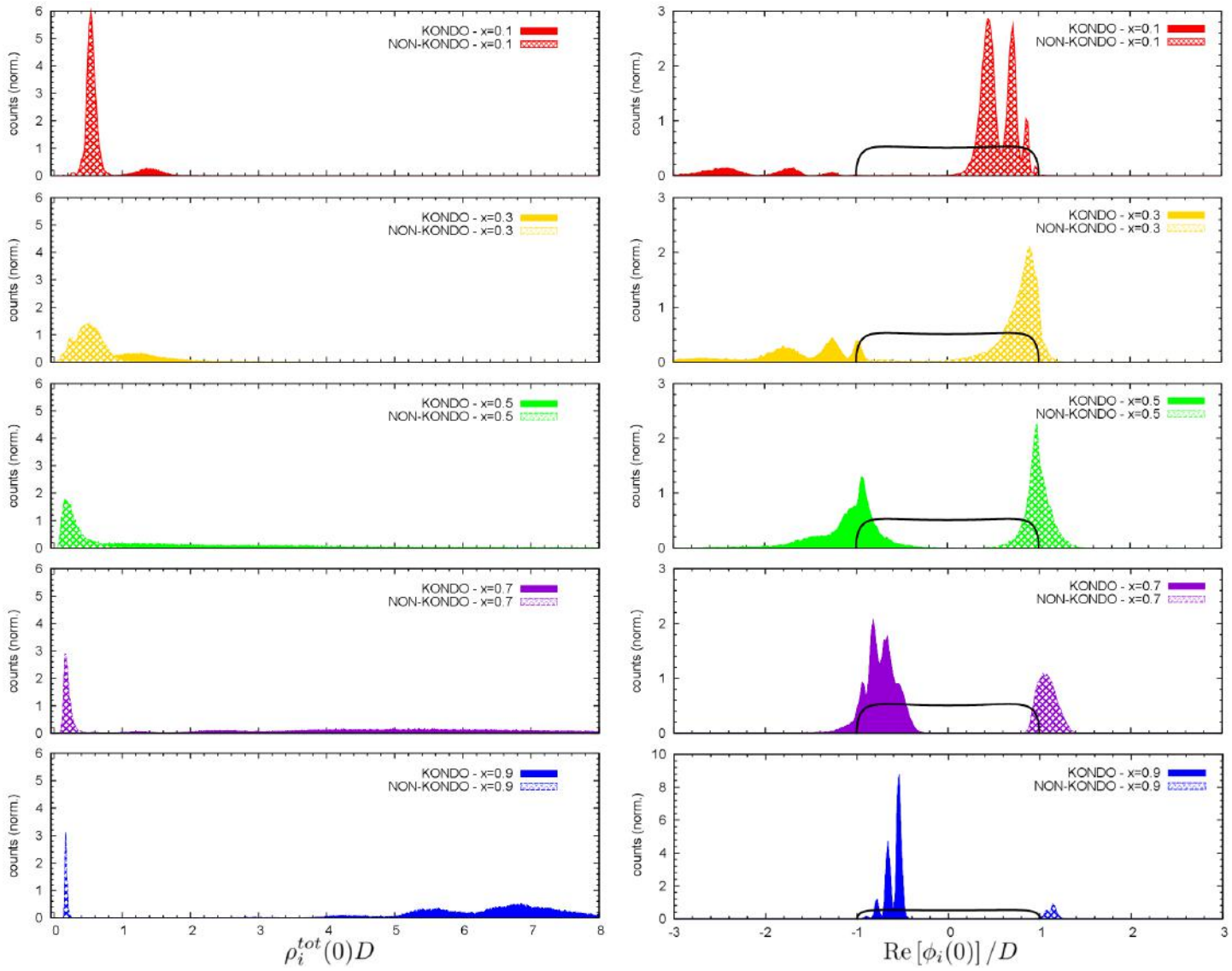

Figure 8.8: Distribution of the total density of states in the Fermi level at the weak coupling regime $J_K = D$. Five values of x are shown, ranging from 0.1 to 0.9, and the distributions are separated for Kondo (solid pattern) and Non-Kondo (hatched pattern) sites. The evolution around the point $x = n_c$ is smooth and $\mathrm{Re}\,[\phi_i(0)]$ of Kondo (Non-Kondo) progressively enters(quits) the non-interacting density of states. For $0.3 \leq x \leq 0.7$ the distribution of $\mathrm{Re}\,[\phi_i(0)]$ for both type of sites have a finite value. Other parameters are $n_c = 0.5$ and $Z = 5$.

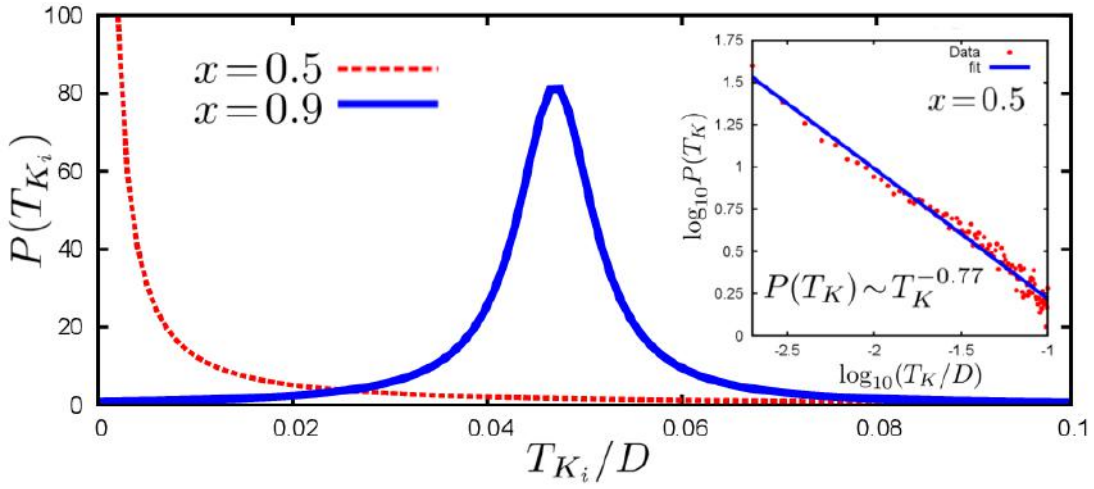

Figure 8.9: Distribution of Kondo temperatures $P(T_{K_i})$ (calculated from Eq. 8.8) in the weak coupling case ($J_K = D$) for $x = 0.5$ (red dashed line) and $x = 0.9$ (blue solid line). Other parameters are $n_c = 0.5$ and $Z = 5$. The power-law behavior of the $x = 0.5$ is an evidence of a Non-Fermi Liquid behavior that is expected when $x \approx n_c$. *Inset:* Double-logarithm plot of $P(T_{K_i})$ for $x = 0.5$. The obtained power-law exponent is -0.77.

is observed. On the other hand, for concentrations at which $\mathrm{Re}\,[\phi_i(0)]$ is distributed far from the band edges ($x = 0.9$), the distribution of Kondo temperatures vanishes for very low T_K. The complete analysis of NFL behavior as a function of J_K and x has not been made in the thesis, but it constitutes an important open question for further investigations.

In Figure 8.10 we show the ratios R_K and R_{NK} (defined in Eq.8.6 and Eq.8.7,respectively) as a function of x for $J_K = D$. Both ratios vary smoothly from their extrema values. The two ratios intersect when $x \approx n_c$ and their values are close to $1/2$. In the weak coupling regime insulating phase does not exist, with the exception of $x = n_c$, which is analogous to Kondo insulator, as explained above.

The evolution of local quantities with the concentration of local moments and Kondo coupling strength was presented in this section. There is an intermediate regime separating the cases of impurity and lattice, well marked for x close to n_c for large enough J_K. A particular signature of such transition is given by the distribution of $\mathrm{Re}[\phi_i(0)]$, which is located either inside or outside the non-interacting band. In the intermediate regime this quantity spreads around the non-interacting band edges.

In the strong coupling regime there is a clear difference between the cases $x < n_c$ and $x > n_c$, and this difference becomes weaker when J_K decreases. Such difference is expected in the strong coupling since the quasiparticles for $x < n_c$ are free, while for $x > n_c$ they are strongly interacting ($U \to \infty$), as we have explained in Section 7.1.2.

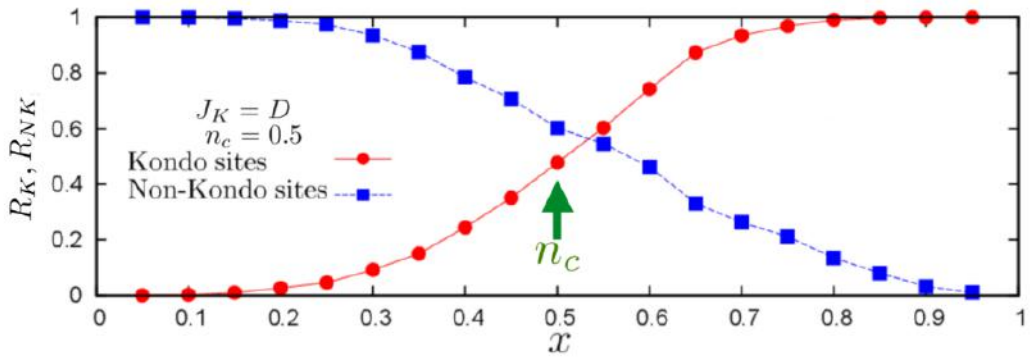

Figure 8.10: Ratios R_K and R_{NK}. Parameters are the same as in Fig. 8.8 and lines are guides for the eyes.

8.3 Neighboring effects

Interesting informations can be obtained by the analysis of distributions with respect to the local environment. Although the stochastic method that provides the construction of baths (with its appropriate probability distribution) does not allow to trace the full "genealogy" of each site, we have at least access to informations concerning the nearest neighbours and it is possible to decompose all the distributions defined in Section 8.1 in terms of the site environment. Defining N_K as the number of Kondo neighbors for a given site i, i.e. the number of sites composing the bath function $\Delta_i(\omega)$ that contains local moments, it is possible to compute the partial statistics by separating sites with different N_K ($0 \leq N_K \leq Z$).

In Figure 8.11 the distributions of $\mathrm{Re}[\phi_i(0)]$ are plotted for different number of neighboring Kondo sites for $x = n_c = 0.5$ and $J_K = D$. This set of parameters corresponds to the intermediate regime of weak coupling scenario (central plot(s) in Fig. 8.8) where $\mathrm{Re}[\phi_i(0)]$ is distributed around the band edges (partially inside, partially outside the non-interacting conduction band) for both Kondo and Non-Kondo sites. Since it was taken $Z = 5$ as in the last section, there are six possible values for N_K displayed in ascending order from the top ($N_K = 0$) to the bottom ($N_K = 5$).

The interpretation of Figure 8.11 is straightforward. The sites with $N_K = 0$ have a bigger probability to belong to a very large cluster (infinite, in the thermodynamic limit) of Non-Kondo sites, which possesses extended electronic states. This probability decreases progressively for increasing N_K and it becomes zero for $N_K = 5$, when all the Non-Kondo sites have localized states for their conduction electrons ($\mathrm{Re}[\phi_i(0)]$ lies outside $[-D; D]$. For Kondo sites the situation is precisely the opposite and extended states are most likely to exist for large N_K.

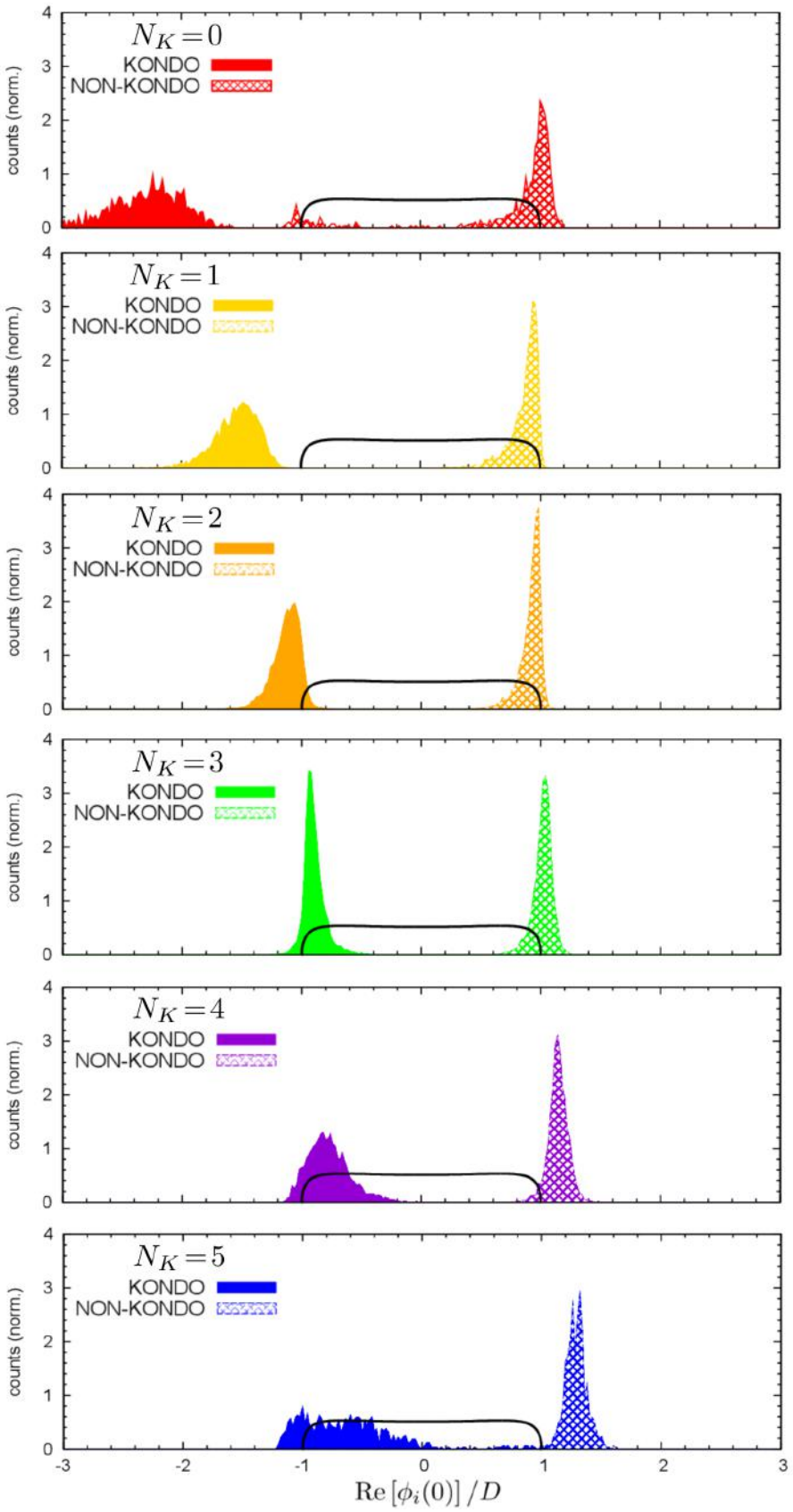

Figure 8.11: Distributions of $\mathrm{Re}\,[\phi_i(0)]$ for each value of N_K, the number of Kondo neighbors, for Kondo and Non-Kondo sites, considering a concentration $x = 0.5$. Other parameters are $Z = 5$, $n_c = 0.5$ and $J_K = D$.

8.4 Lower dimensions and percolation problem

Since the method introduced in Section 7.3 is valid for a Bethe lattice with any coordination number Z, we can address the issue of the KAM in low dimensions. In particular there are significant effects related to the absence of percolation of the two existent sublattices, formed by Kondo and Non-Kondo sites, that we will discuss in this section.

Percolation is an important concept in a classical description of conductivity in random media. For general aspects of percolation theory and physical examples, we refer to References [153, 154]. Here we will briefly explain its consequences for our problem of Kondo Alloys. The physical picture is the following: in the strong coupling analysis of the model and in the results presented in Section 8.2.1, we have argued that some sites behave as *insulators*. For instance, in the diluted regime (characterized by $n_c > x$) the Kondo sites play this role since conduction electrons are participating in singlets, as it was claimed by Nozières in Ref. [94]. In this case, the remaining electrons move in the lattice of Non-Kondo sites. Now there are two possible scenarios for the behavior of the remaining electrons: if the depleted lattice *percolates* these electrons will move in infinitely large clusters and their states (or their wave-functions) will be extended through the whole system, as it happens in a metal. On the other hand, if the depleted lattice *does not percolate*, electronic states are constrained to a finite region of the system. So a different behavior is expected whether the concentration of Non-Kondo sites exceeds the percolation threshold or not. The same issue is present in the concentrated regime ($n_c < x$), except that in this case it is the percolation (or not) of Kondo sites that matters.

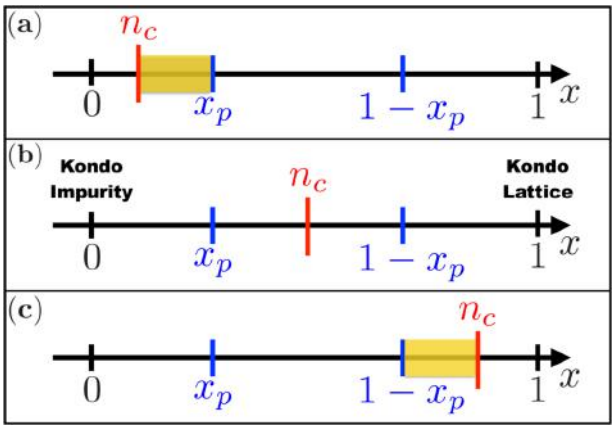

Figure 8.12: Percolation in the Kondo Alloy model for three different cases: **(a)** $n_c < x_p$, **(b)** $x_p < n_c < 1 - x_p$ and **(c)** $1 - x_p < n_c$. The shadowed yellow areas indicate intervals in which percolation does not take place for one type of lattice sites. For instance, in case **(a)** the Kondo sites do not percolate in the interval $n_c < x < x_p$, while in **(c)** the same happens to Non-Kondo sites in the interval $1 - x_p < x < n_c$. In case **(b)** percolation is never an issue, as expected for lattices with low percolation threshold and an intermediate n_c. Note that in our further example (using $Z = 3$) $x_p = 1 - x_p$, then the case **(b)** can only occur for $n_c = x_p$.

The percolation threshold for a Bethe lattice is $x_p = 1/(Z-1)$[153]. In the diluted regime $x < n_c$ of the Kondo Alloy model the absence of percolation takes place if the concentration

of Non-Kondo sites $1-x$ is smaller than the percolation threshold x_p. This gives the first condition:

$$1-x_p<x<n_c \tag{8.9}$$

In the concentrated regime $x>n_c$, the absence of percolation of Kondo sites happens for $x<x_p$.This gives the second condition:

$$n_c<x<x_p. \tag{8.10}$$

When one of these two conditions (in Eqs.8.9 and 8.10) is realized, there is a percolation problem.

For a lattice with a low percolation threshold, one of the two conditions presented above can be satisfied only in extreme cases, when n_c is close to the half-filling or almost zero. In the usually employed infinity Z Bethe lattice these conditions are never satisfied. So far, we have shown results for a lattice with $Z=5$ and $n_c=0.5$, in which percolation always happens. Then, in order to investigate the possible issue of the lack of percolation, we need to consider a lattice with a bigger percolation threshold and different concentrations n_c.

Our analysis is based again on the quantity $\mathrm{Re}[\phi_i(0)]$, defined in Eq.8.2. According to the discussions in Section 8.1, the distinction between localized and extended electronic states at the Fermi energy can be simplified by the comparison of $\mathrm{Re}[\phi_i(0)]$ and the non-interacting density of states.

In Figure 8.13 we present the ratios R_K and R_{NK}, given by Eqs.8.6 and 8.7, as a function of the local moment concentration x for $J_K=5D$ (left) and $J_K=2D$ (right). Three different electronic fillings are chosen: $n_c=0.25$, $n_c=0.5$ (the percolation threshold) and $n_c=0.75$.

For $n_c=0.25$ and $J_K=5D$, R_{NK} progressively decreases with increasing x, being close to zero for $x=n_c$, while in Kondo sites R_K is zero through this range of concentrations. Between $x=n_c$ and $x=x_p=0.5$ the ratios R_K and R_{NK} are zero *for both type of sites* and R_K increases only for $x\approx 0.55>x_p$. This is related to the lack of Kondo sites percolation when $n_c<x<x_p$, indicating the absence of extended states close to the Fermi energy in both sub-lattices. The absence of percolation in the interval $n_c<x<x_p$ is still visible for $J_K=2D$ and both ratios are very small in this region.

For $n_c=0.75$ the same effect appears in the Non-Kondo sites. R_{NK} decreases until it reaches a value close to zero for $x=1-x_p$. For $1-x_p<x<n_c$ the Non-Kondo sub-lattice does not percolate and the metallic behavior is expected to be lost. Extended states will appear in Kondo sites after crossing the point $x=n_c$. This clearly happens for $J_K=2D$, while for $J_K=5D$ the interval in x in which both ratios vanish extends for $x>n_c$ due to the very strong Kondo interaction. An insulating phase is seen up to $x=0.95$. The ratio R_K is expected to increase above this value and for $x=1$ (not shown) it must be equal to one again.

When n_c is chosen to be the percolation threshold none of these effects are visible, since percolation issues are not reachable. Instead there is a dip for both curves at the crossing point $n_c=x$ for $J_K=2D$. It corresponds to an insulating phase that marks this transition in the strong coupling limit. For $J_K=5D$ there are two metal-insulator transitions for $x=0.45$ and $x=0.8$, but they are probably related to the Anderson localization (see Figure 8.7 and discussions therein) and not to the lack of percolation. We note that the asymmetry between

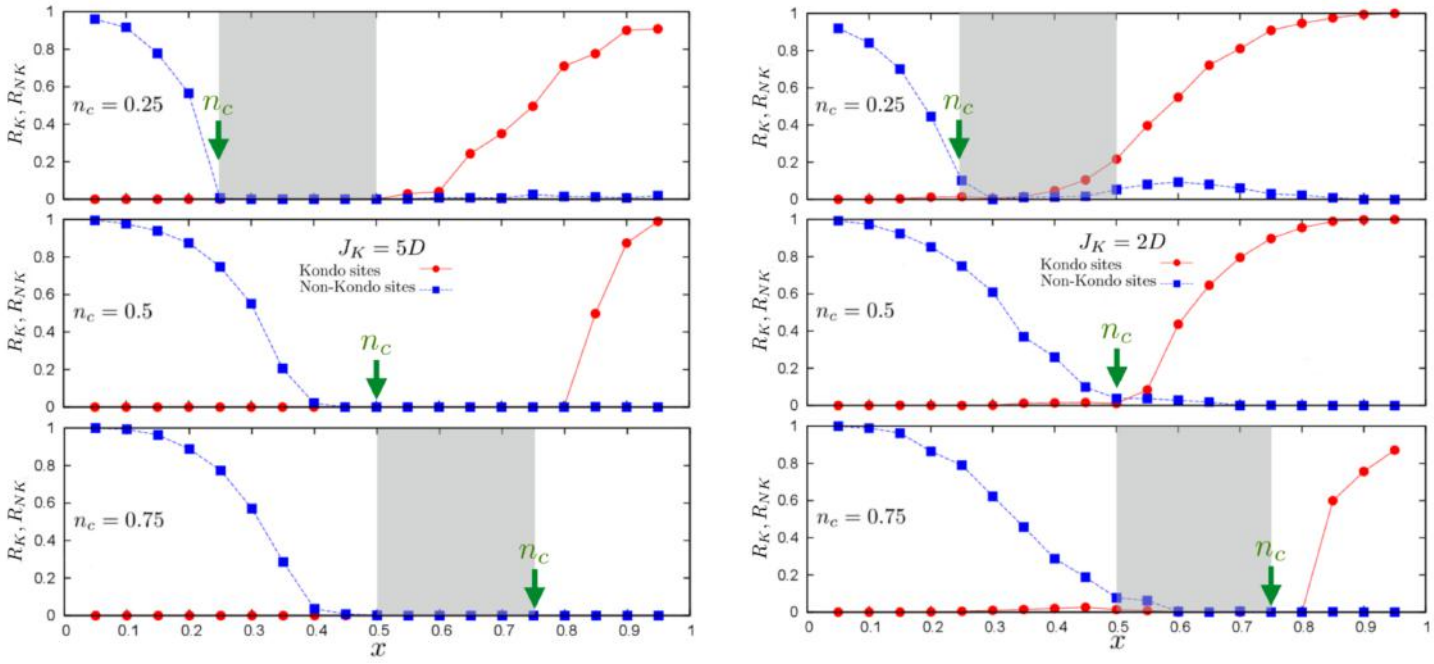

Figure 8.13: Ratios R_K and R_{NK} (defined in Eqs.8.6 and 8.7) as a function of x for $J_K = 5D$ (**left**) and $J_K = 2D$ (**right**) in a $Z = 3$ Bethe lattice. The electronic fillings are fixed in three different values: $n_c = 0.25$ (top), $n_c = 0.5$ (middle) and $n_c = 0.75$ (bottom). These values are indicated by the green arrow on the plots and the horizontal ticked line represents the percolation threshold $x_p = 0.5$ ($x_p = 1 - x_p$). Grey regions on the plot indicate where percolation is expected to be absent (see Fig.8.12).

the cases $x < n_c$ and $x > n_c$, due to the different types of quasiparticles (free or strongly interacting) is seen again for $J_K = 5D$.

In Figure 8.14 we repeat the previous plot for $J_K = D$. In the weak coupling regime, the regions where the percolation is lost are not clearly visible. Instead, the only apparent feature is the "transition" at $n_c = x$, signaled by the interception of Kondo and Non-Kondo sites' curves (as in 8.10). As a conclusion, the effects of localization of electronic states and the percolation problem disappear if the Kondo interaction is weak.

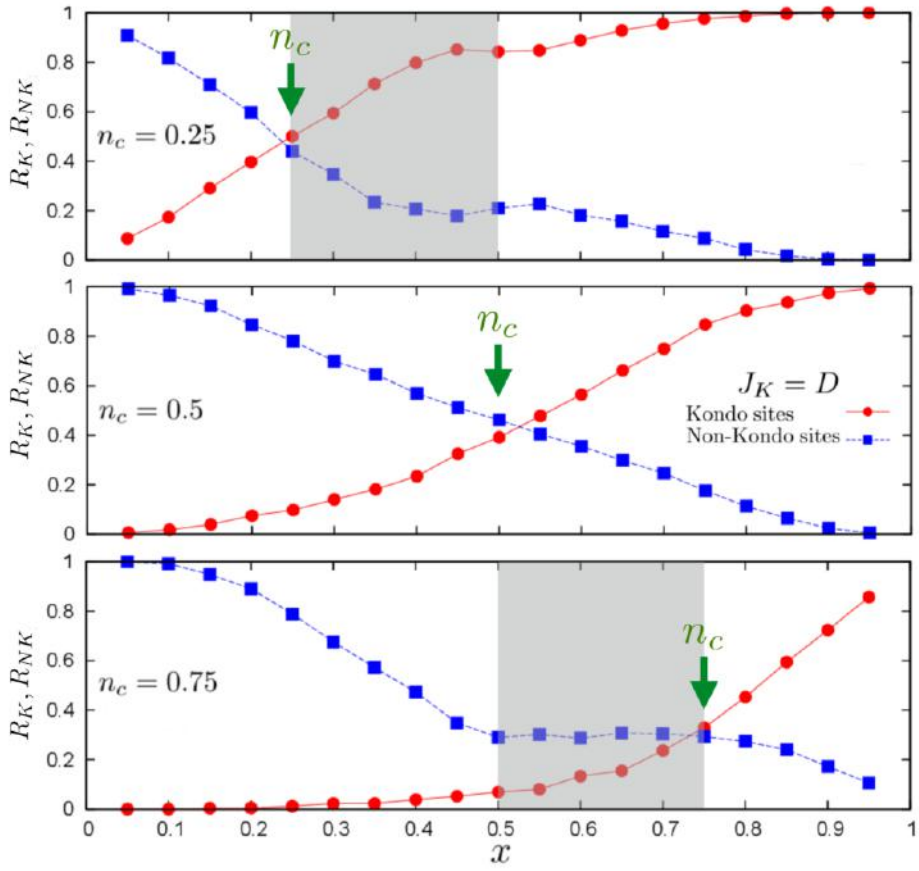

Figure 8.14: Ratios R_K and R_{NK} as a function of x for $J_K = D$ in a $Z = 3$ Bethe lattice. The electronic fillings are fixed in three different values: $n_c = 0.25$ (top), $n_c = 0.5$ (middle) and $n_c = 0.75$ (bottom).

8.5 Summary

In this chapter we have presented the results of the Kondo Alloy model (Eq. 7.1) obtained from the Statistical Dynamical Mean-Field Theory presented in Section 7.3. This method has as a principal feature the ability to access the distributions of local quantities in the model, being some of them introduced in Section 8.1. In this work we restrict ourselves mainly in the distributions of quantities at the Fermi energy, in special, the density of states (Eq. 8.1) and the ϕ-function (Eq. 8.2).

In Section 8.2 we have shown how these two quantities evolved from the dilute ($x \ll n_c$) to the concentrated ($x \gg n_c$) regimes in the strong ($J_K = 5D$) and weak ($J_K = D$) coupling scenarios. In the strong coupling we could identify two metal-insulator transitions at $x = n_c = 0.5$ and $x = 0.75$ separating both regimes. While the system was expected to be an insulator at the point $x = n_c$ from the $J_K \to \infty$ limit analysis (Section 7.1.2), the insulating region above this point is a new feature of the KAM and we believe that it is connected to the localization of electronic states due to strong disorder. In the weak coupling scenario the metal-insulator transitions disappear and the passage from the dilute to the concentrated regimes is smooth. For intermediate concentrations ($x \approx n_c$), we have seen that te distributions of $\mathrm{Re}\,[\phi_i(0)]$ are peaked in the band edges. This result suggests that disorder for weak interactions can lead to a Non-Fermi liquid behavior, which is a precursor of the metal-insulator transition seen at strong interaction. The case $x = n_c$ was further investigated in Section 8.3, where we have shown the partial distributions of $\mathrm{Re}\,[\phi_i(0)]$ for sites containing different numbers of Kondo sites as neighbors. The results indicate that Kondo sites have a behavior closer to the dense case ($x > n_c$) the more they are surrounded by other Kondo sites (forming clusters). This corroborates the idea that the disorder provided by different local environments dominates the intermediate concentration regimes.

In Section 8.4 we have addressed the percolation issue in the context of the Kondo Alloy model. The absence of percolation can affect the formation of metallic states in both regimes (dilute and dense) of the model, as it is discussed in Figure 8.12. For this purpose, we have presented results for the Bethe lattice with $Z = 3$ (whose percolation threshold is $x_p = 0.5$) and different concentrations of conduction electrons. Using the ratios R_K and R_{NK} (Eqs. 8.6 and 8.7), we have shown that the lack of percolation introduces new insulating regions in the phase diagram of KAM for intermediate and strong J_K interactions. These regions can be further increased by disorder, as seen in Section 8.2.

Chapter 9

Conclusions and perspectives

In Part II we have studied the Kondo Alloy model within the Statistical Dynamical Mean-Field Theory and a mean-field approximation for the Kondo interaction. The method allows to go beyond the Coherent Potential Approximation and includes inhomogeneities from different local environments. The procedure is shown to be exact [146, 115] in a Bethe lattice of finite coordination number.

The central results presented in this work are distributions of local quantities that allow a complete characterization of the problem, even if physical observables are given in terms of averaged quantities. Apart from the usual quantities discussed in the context of Kondo physics, as the mean-field parameters r_i and λ_i or the local density of states $\rho_i(\omega) = (-1/\pi)\mathrm{Im}[G_{ii}(\omega + i0^+)]$, we have introduced a new function $\phi_i(\omega)$ and we have analyzed it close to the Fermi energy. This function is interpreted as a measure of the extended/localized nature of the local electronic states.

In a first step we have examined the distributions of $\rho_i^{tot}(0)$ and $\mathrm{Re}\,[\phi_i(0)]$ by changing the concentration of local moments x and the strength of the Kondo interaction J_K. In the strong coupling scenario we have found two metal-insulator transitions in the intermediate concentration range ($x \approx n_c$) that separate the dilute and dense regimes of KAM. Our results show an asymmetry around the point $x = n_c$ if Kondo interaction is strong, what can be understood in terms of the different nature of the quasiparticles (free or strongly correlated) seen in the $J_K \to \infty$ limit. In particular, we have suggested that the insulating phase observed for $x \gtrsim n_c$ is related to the combined effects of disorder and the strong correlations, leading to localization of electronic states. For smaller J_K disorder is expected to produce Non-Fermi liquid behavior, which is suggested from our results of $\mathrm{Re}\,[\phi_i(0)]$ when $x \approx n_c$. These two features will be analyzed in more details in future works.

In order to determine in which region Non-Fermi Liquid behavior could occur due to disorder within our theoretical approach, it is crucial to calculate the temperature dependence of physical quantities such as the magnetic susceptibility, the specific heat or the electrical conductivity. It can be done after an adaptation of the method to perform finite temperature calculations of the mean-field parameters or by using a different impurity solver.

A second aspect discussed in this work is the dimensionality effects. We remind that such

effects are enhanced in the case of a big percolation threshold and a large Kondo interaction, which is usually not the case of the typical Kondo systems which have been experimentally studied up to now. Nevertheless such issues might be useful for the study of Kondo effect in nanostructures, which have a higher degree of controllability.

Apart from the calculations of physical observables at finite temperature, another highly desirable perspective is to take into account the effects of magnetism in the Kondo Alloy model, neglected in the present work. While it is well stablished that magnetic ordered ground states are possible in the Kondo Lattice and spin glass behavior is observed in many systems with diluted impurities, it is unknown how these phases evolve with the concentration of magnetic moments. It would be interesting to study the interplay between magnetism and Kondo effect in the KAM. Also it is fair to speculate that the magnetism would be more sensitive to the percolation issues. The study of magnetic phases in KAM is a priori beyond the scope of the statistical DMFT method.

Appendix A

Hubbard-I approximation for the EPAM

The method chosen to solve the Extended Periodic Anderson model hamiltonian (Equation 3.1) is based on the truncation of the equation of motion for the electronic propagators. In principle the equation of motion for a given Green's function leads to higher-order terms for hamiltonian containing two(or high)-body terms. The truncation will be inspired by the so called Hubbard-I approximation[69, 70, 71]. The major drawback of this approximation in the context of the Hubbard model is the existence of a Mott-insulating regime for the half-filled correlated band for a finite value of U. For the Periodic Anderson model this issue does not hold since the f-orbitals are dispersionless.

In Section 3.3.2 the complete Green's functions for the EPAM were derived in a more pedagogical form. Here we will perform the same approximations directly in the equation of motion of the EPAM. A similar derivation is done for the Periodic Anderson model (Eq. 1.9) in Ref. [155].

For convenience we will consider the following form of the hamiltonian in Eq.3.1:

$$\mathcal{H}_{EPAM} = -\sum_{i,j\sigma}(t_{ij} - \overline{\epsilon}_c\delta_{ij})c^{\dagger}_{i\sigma}c_{j\sigma} + \sum_{i\sigma}\widetilde{\varepsilon}_{f,\sigma}f^{\dagger}_{i\sigma}f_{i\sigma} + \frac{U}{2}\sum_{i\sigma}\hat{n}^{f}_{i\overline{\sigma}}\hat{n}^{f}_{i\sigma} + V\sum_{i\sigma}\left(c^{\dagger}_{i\sigma}f_{i\sigma} + f^{\dagger}_{i\sigma}c_{i\sigma}\right) - U_{fc}n_cn_f \quad \text{(A.1)}$$

The hamiltonian above is written in its site representation, t_{ij} being the hopping integral. The mean-field approximation for U_{fc} term is already included, as discussed in Section 3.3.1, and we define $\overline{\epsilon}_c \equiv U_{fc}n_f$ for shortness. The relation between t_{ij} and the band dispersion $\epsilon(\mathbf{k})$ (defined in Eq. 3.1) is given through a Fourier transformation:

$$-\sum_{i,j\sigma}t_{ij}c^{\dagger}_{i\sigma}c_{j\sigma} = \sum_{\mathbf{k}\sigma}\epsilon(\mathbf{k})c^{\dagger}_{\mathbf{k}\sigma}c_{\mathbf{k}\sigma}$$

The equation of motion for a fermionic propagator[1] $G^{ab}_{i\sigma,j\sigma'}(\omega) \equiv \ll a_{i\sigma}\,; b^{\dagger}_{j\sigma'} \gg$ in frequency

[1]We recall that the Zubarev's notation[72] for Green's functions is used in this Appendix.

representation is:

$$\omega \ll a_{i\sigma}\,;b^{\dagger}_{j\sigma'}\gg = \left\langle \{a_{i\sigma};b^{\dagger}_{j\sigma'}\}\right\rangle + \ll [a_{i\sigma};H]\,;b^{\dagger}_{j\sigma'}\gg . \tag{A.2}$$

For the conduction electrons we have:

$$\omega \ll c_{i\sigma}\,;c^{\dagger}_{i\sigma}\gg = 1 - \sum_{j} t_{ij} \ll c_{j\sigma}\,;c^{\dagger}_{i\sigma}\gg + \overline{\epsilon}_c \ll c_{i\sigma}\,;c^{\dagger}_{i\sigma}\gg + V \ll f_{i\sigma}\,;c^{\dagger}_{i\sigma}\gg \tag{A.3}$$

For f-electrons the equation of motion is:

$$\omega \ll f_{i\sigma}\,;f^{\dagger}_{i\sigma}\gg = 1 + \widetilde{\varepsilon}_{f\sigma} \ll f_{i\sigma}\,;f^{\dagger}_{i\sigma}\gg + U \ll \hat{n}^{f}_{i\overline{\sigma}} f_{i\sigma}\,;f^{\dagger}_{i\sigma}\gg + V \ll c_{i\sigma}\,;f^{\dagger}_{i\sigma}\gg \tag{A.4}$$

In a similar way, for the mixed Green's Functions $G^{cf}_{\sigma}(\mathbf{k},\omega) \equiv \ll c_{i\sigma};f^{\dagger}_{i\sigma}\gg$ and $G^{fc}_{\sigma}(\mathbf{k},\omega) \equiv \ll f_{i\sigma}\,;c^{\dagger}_{i\sigma}\gg$:

$$\omega \ll c_{i\sigma}\,;f^{\dagger}_{i\sigma}\gg = -\sum_{j} t_{ji} \ll c_{j\sigma}\,;f^{\dagger}_{i\sigma}\gg + \overline{\epsilon}_c \ll c_{i\sigma}\,;f^{\dagger}_{i\sigma}\gg + V \ll f_{i\sigma}\,;f^{\dagger}_{i\sigma}\gg \tag{A.5}$$

$$\omega \ll f_{i\sigma}\,;c^{\dagger}_{i\sigma}\gg = \widetilde{\varepsilon}_{f\sigma} \ll f_{i\sigma}\,;c^{\dagger}_{i\sigma}\gg + U \ll \hat{n}^{f}_{i\overline{\sigma}} f_{i\sigma}\,;c^{\dagger}_{i\sigma}\gg + V \ll c_{i\sigma}\,;c^{\dagger}_{i\sigma}\gg \tag{A.6}$$

Note that in Eqs. A.4 and A.6 it appears higher-orders Green's functions. Their equations of motion are:

$$\begin{aligned}\omega \ll \hat{n}^{f}_{i\overline{\sigma}} f_{i\sigma}\,;f^{\dagger}_{i\sigma}\gg = &< \hat{n}^{f}_{i\overline{\sigma}} > + \widetilde{\varepsilon}_{f\sigma} \ll \hat{n}^{f}_{i\overline{\sigma}} f_{i\sigma}\,;f^{\dagger}_{i\sigma}\gg + U \ll \hat{n}^{f}_{i\overline{\sigma}} f_{i\sigma}\,;f^{\dagger}_{i\sigma}\gg \\ &+ V \ll n_{f,i\overline{\sigma}} c_{i\sigma}\,;f^{\dagger}_{i\sigma}\gg + V \ll (f^{\dagger}_{i\overline{\sigma}} c_{i\overline{\sigma}} - c^{\dagger}_{i\overline{\sigma}} f_{i\overline{\sigma}}) f_{i\sigma}\,;f^{\dagger}_{i\sigma}\gg\end{aligned} \tag{A.7}$$

$$\begin{aligned}\omega \ll \hat{n}^{f}_{,i\overline{\sigma}} f_{i\sigma}\,;c^{\dagger}_{i\sigma}\gg = &\widetilde{\varepsilon}_{f\sigma} \ll \hat{n}^{f}_{i\overline{\sigma}} f_{i\sigma}\,;c^{\dagger}_{i\sigma}\gg + U \ll \hat{n}^{f}_{i\overline{\sigma}} f_{i\sigma}\,;c^{\dagger}_{i\sigma}\gg \\ &+ V \ll \hat{n}^{f}_{i\overline{\sigma}} c_{i\sigma}\,;c^{\dagger}_{i\sigma}\gg + V \ll (f^{\dagger}_{i\overline{\sigma}} c_{i\overline{\sigma}} - c^{\dagger}_{i\overline{\sigma}} f_{i\overline{\sigma}}) f_{i\sigma}\,;c^{\dagger}_{i\sigma}\gg\end{aligned} \tag{A.8}$$

In this generic Hubbard-I approximation we settle ($a^{\dagger}$ standing for both $c^{\dagger}$ and $f^{\dagger}$):

$$\begin{aligned}\ll \hat{n}^{f}_{i\overline{\sigma}} c_{i\sigma}\,;a^{\dagger}_{i\sigma}\gg &= n_{f,i\overline{\sigma}} \ll c_{i\sigma}\,;a^{\dagger}_{i\sigma}\gg \\ \ll (f^{\dagger}_{i\overline{\sigma}} c_{i\overline{\sigma}} - c^{\dagger}_{i\overline{\sigma}} f_{i\overline{\sigma}}) f_{i\sigma}\,;a^{\dagger}_{i\sigma}\gg &= 0\end{aligned}$$

Using these relations, Eqs. A.7 and A.8 express the high-order Green's functions in terms of Green's functions with two operators, allowing the set of equations in Eqs. A.3-A.6 to be solved after a Fourier transformation in k-space. Explicitly:

$$(\omega - \widetilde{\varepsilon}_c(\mathbf{k}))\, G^{cc}_{\sigma}(\mathbf{k},\omega) = 1 + V G^{fc}_{\sigma}(\mathbf{k},\omega) \tag{A.9}$$

$$(\omega - \widetilde{\varepsilon}_{f\sigma})\, G^{ff}_{\sigma}(\mathbf{k},\omega) = 1 + V G^{cf}_{\sigma}(\mathbf{k},\omega) + U < \hat{n}^{f}_{\overline{\sigma}} > \left(\frac{1 + V G^{cf}_{\sigma}(\mathbf{k},\omega)}{\omega - \widetilde{\varepsilon}_{f\sigma} - U} \right) \tag{A.10}$$

$$(\omega - \widetilde{\varepsilon}_c(\mathbf{k}))\, G^{cf}_{\sigma}(\mathbf{k},\omega) = V G^{ff}_{\sigma}(\mathbf{k},\omega) \tag{A.11}$$

$$(\omega - \widetilde{\varepsilon}_{f\sigma})\, G^{fc}_{\sigma}(\mathbf{k},\omega) = V G^{cc}_{\sigma}(\mathbf{k},\omega) + U < \hat{n}^{f}_{\overline{\sigma}} > \left(\frac{V G^{cc}_{\sigma}(\mathbf{k},\omega)}{\omega - \tilde{\varepsilon}_{f\sigma} - U} \right) \tag{A.12}$$

Here the relation $\widetilde{\varepsilon}_c(\mathbf{k}) \equiv \epsilon(\mathbf{k}) + \overline{\epsilon}_c$ (Eq. 3.7) was used. After some algebra:

$$G_\sigma^{cc}(\mathbf{k},\omega) = \frac{1}{\omega - \widetilde{\varepsilon}_c(\mathbf{k}) - \left(1 + \frac{U<\hat{n}_{\overline{\sigma}}^f>}{\omega - \widetilde{\varepsilon}_{f\sigma} - U}\right)\frac{V^2}{\omega - \widetilde{\varepsilon}_{f\sigma}}} \tag{A.13}$$

$$G_\sigma^{ff}(\mathbf{k},\omega) = \frac{\left(1 + \frac{U<\hat{n}_{\overline{\sigma}}^f>}{\omega - \widetilde{\varepsilon}_{f\sigma} - U}\right)}{\omega - \widetilde{\varepsilon}_{f\sigma} - \left(1 + \frac{U<\hat{n}_{\overline{\sigma}}^f>}{\omega - \widetilde{\varepsilon}_{f\sigma} - U}\right)\frac{V^2}{\omega - \widetilde{\varepsilon}_c(\mathbf{k})}} \tag{A.14}$$

The equations above are the complete Green's functions of EPAM in Hubbard-I approximation for *a finite value* of the Coulomb repulsion U. We will further simplify these expressions by taking the $U \to \infty$ limit.

Infinite U limit

In Hubbard-I approximation, the Coulomb interaction appears in the expression for Green's functions through the frequency-dependent quantity

$$1 + \frac{U n_{f,\overline{\sigma}}}{\omega - \tilde{\varepsilon}_{f\sigma} - U},$$

which renormalizes the hybridization and gives the spectral weight for the lower Hubbard subband. Its denominator can be expanded in powers of $1/U$ in the limit of large correlation:

$$1 + \frac{U n_{f,\overline{\sigma}}}{\omega - \tilde{\varepsilon}_{f\sigma} - U} \xrightarrow{U \to +\infty} 1 - n_{f,\overline{\sigma}}$$

We define

$$p_\sigma \equiv 1 - n_{f,\overline{\sigma}}, \tag{A.15}$$

which allows us to write the Green's functions in Eqs.A.13 and A.14 compactly as:

$$G_\sigma^{cc}(\mathbf{k},\omega) = \frac{1}{(g_\sigma^{cc}(\mathbf{k},\omega))^{-1} - p_\sigma V^2 g_\sigma^{ff}(\omega)} \tag{A.16}$$

$$G_\sigma^{ff}(\mathbf{k},\omega) = \frac{1}{(g_\sigma^{ff}(\omega))^{-1} - V^2 g_\sigma^{cc}(\mathbf{k},\omega)} \tag{A.17}$$

having defined

$$g_\sigma^{ff}(\omega) \equiv \frac{p_\sigma}{\omega - \tilde{\varepsilon}_{f\sigma}} \tag{A.18}$$

$$g_\sigma^{cc}(\mathbf{k},\omega) \equiv \frac{1}{\omega - \tilde{\varepsilon}_{c\sigma}(\mathbf{k})} \tag{A.19}$$

The Equations A.16 and A.17 are identical to Eqs. 3.24 and 3.25 derived in Section 3.3.3.

For completeness the mixed Green's functions $G_\sigma^{cf}(\mathbf{k},\omega)$ and $G_\sigma^{fc}(\mathbf{k},\omega)$ are also presented:

$$G_\sigma^{cf}(\mathbf{k},\omega) = g_\sigma^{cc}(\mathbf{k},\omega) V G_\sigma^{ff}(\mathbf{k},\omega) \tag{A.20}$$

$$G_\sigma^{fc}(\mathbf{k},\omega) = g_\sigma^{ff}(\omega) V G_\sigma^{cc}(\mathbf{k},\omega) \tag{A.21}$$

Appendix B

Magnetic Susceptibility for the EPAM

Here we will derive the analytical expression of the magnetic susceptibility in the paramagnetic phase of the EPAM (Eq.4.11) at zero temperature. This derivation is based on an expansion of the equations for $n_{f,\uparrow}$ and $n_{f,\downarrow}$ when an infinitesimal external magnetic field h_{ext} is applied to the system. It is possible to write the magnetic response $\chi_0 = m_f/h_{ext}$ in terms of the parameters of the problem in the absence of magnetic fields. χ_0 can be evaluated using the self-consistent results obtained in Chapter 4.1.

For practical matters, it is easier to separate the calculation in two cases, depending on the chemical potential position μ with respect to the lower and upper energy band (defined in Eqs.3.38-3.41.

μ in the lower energy band

Let us consider first that the chemical potential μ lies below the hybridization gap. In this case, the integration must be performed only in the lower part of the density of states, defined between ω_1 and ω_2 (Eqs.3.38 and 3.39). The f-electron magnetization is given by:

$$m_f = \int_{\omega_{1,\uparrow}}^{\mu} d\omega \rho_{\uparrow}^{ff}(\omega) - \int_{\omega_{1,\downarrow}}^{\mu} d\omega \rho_{\downarrow}^{ff}(\omega) \tag{B.1}$$

Using Eq.4.19, the expression for the f-electron density of states is

$$\rho_{\sigma}^{ff}(\omega) = \frac{1}{2D} \frac{p_{\sigma}^2 V^2}{\left(\omega - \widetilde{\varepsilon}_{f\sigma}\right)^2}, \tag{B.2}$$

The parameters $\widetilde{\varepsilon}_{f\sigma}$ and p_{σ} are defined by the equations 4.13 and 4.14, respectively. Performing the integrals in Eq.B.1, one gets:

$$m_f = \frac{p_{\uparrow}^2 V^2}{2D} \left(\frac{1}{\omega_{1,\uparrow} - \widetilde{\varepsilon}_{f,\uparrow}} - \frac{1}{\mu - \widetilde{\varepsilon}_{f,\uparrow}} \right) - \frac{p_{\downarrow}^2 V^2}{2D} \left(\frac{1}{\omega_{1,\downarrow} - \widetilde{\varepsilon}_{f,\downarrow}} - \frac{1}{\mu - \widetilde{\varepsilon}_{f,\downarrow}} \right) \tag{B.3}$$

We consider now the application of a very small magnetic field h_{ext} that will polarize the system. It will produce a magnetization $m_f = \chi_0 h_{ext}$ to be calculated from the expression above, which depends on h_{ext} through the spin-dependent coefficients p_σ, $\widetilde{\varepsilon}_{f,\sigma}$ and $\omega_{1,\sigma}$. The dependence in h_{ext} is direct for the first two parameters[1]:

$$p_\sigma = 1 - n_{f\overline{\sigma}} = 1 - \frac{n_f}{2} - \frac{\overline{\sigma} m_f}{2} \equiv p_0 + \sigma \frac{\chi_0 h_{ext}}{2}$$
$$\widetilde{\varepsilon}_{f,\sigma} = \widetilde{\varepsilon}_{f,0} - \sigma g_f h_{ext}$$

In the same order, we have:

$$p_\sigma^2 \approx p_0^2 + \sigma h_{ext} \chi_0 p_0 \tag{B.4}$$

The dependence on h_{ext} in $\omega_{i,\sigma}$ comes from the parameters above, but a Taylor expansion is required. Up to the first order in h_{ext}, we have (from Eqs. 3.38):

$$\omega_{1,\sigma} - \widetilde{\varepsilon}_{f,\sigma} = \omega_{1,0} - \widetilde{\varepsilon}_{f,0} + \sigma h_{ext} \left[\frac{g_f}{2} - \frac{g_f \overline{E}_0(-D)}{2\Delta_0(-D)} - \frac{\chi_0 V^2}{4\Delta_0(-D)} \right]$$

For shortness, the following definitions are employed in the expression above:

$$\overline{E}_0(-D) = \frac{\widetilde{\varepsilon}_c(-D) - \widetilde{\varepsilon}_{f,0}}{2} \tag{B.5}$$
$$\Delta_0(-D) = \sqrt{[\overline{E}_0(-D)]^2 + p_0 V^2} \tag{B.6}$$

After a first-order Taylor expansion in h_{ext}, the denominators in Eq. B.3 are:

$$\frac{1}{\omega_{1,\sigma} - \widetilde{\varepsilon}_{f\sigma}} = \frac{1}{\omega_{1,0} - \widetilde{\varepsilon}_{f,0}} \left[1 - \sigma h_{ext} \left(\frac{g_f}{2} - \frac{g_f \overline{E}_0(-D)}{2\Delta_0(-D)} - \frac{\chi_0 V^2}{4\Delta_0(-D)} \right) \left(\frac{1}{\omega_{1,0} - \widetilde{\varepsilon}_{f,0}} \right) \right] \tag{B.7}$$

$$\frac{1}{\mu - \widetilde{\varepsilon}_{f\sigma}} = \frac{1}{\mu - \widetilde{\varepsilon}_{f,0}} \left[1 - \sigma h_{ext} \left(\frac{1}{\mu - \widetilde{\varepsilon}_{f,0}} \right) \right] \tag{B.8}$$

Gathering all the terms up to the first order in h_{ext} and defining $\chi_0 \equiv m_f / h_{ext}$, we get the closed expression:

$$\begin{aligned} \chi_0 =& \frac{p_0^2 V^2}{2D} \left[-2 \left(\frac{1}{\omega_{1,0} - \widetilde{\varepsilon}_{f,0}} \right)^2 \left(\frac{g_f}{2} - \frac{g_f \overline{E}_0(-D)}{2\Delta_0(-D)} - \frac{\chi_0 V^2}{4\Delta_0(-D)} \right) + 2 g_f \left(\frac{1}{\mu - \widetilde{\varepsilon}_{f,0}} \right)^2 \right] \\ &+ \frac{p_0 \chi_0 V^2}{2D} 2 \left[\frac{1}{\omega_{1,0} - \widetilde{\varepsilon}_{f,0}} - \frac{1}{\mu - \widetilde{\varepsilon}_{f,0}} \right] \end{aligned} \tag{B.9}$$

[1] Through this section the parameters indexed by the subscript 0 correspond to the values in the absence of magnetic field.

The solution of the equation above for χ_0 is:

$$\chi_0 = \frac{C_0}{1 - C_1} \tag{B.10}$$

The coefficients C_0 and C_1 are given by:

$$C_0 = \frac{p_0^2 V^2}{D}\left[-\left(\frac{1}{\omega_{1,0} - \widetilde{\varepsilon}_{f0}}\right)^2 \left(\frac{g_f}{2} - \frac{g_f \overline{E}_0(-D)}{2\Delta_0(-D)}\right) + g_f \left(\frac{1}{\mu - \widetilde{\varepsilon}_{f,0}}\right)^2\right] \tag{B.11}$$

$$C_1 = \frac{p_0^2 V^2}{D}\left(\frac{1}{\omega_{1,0} - \widetilde{\varepsilon}_{f,0}}\right)^2 \frac{V^2}{4\Delta_0(-D)} + \frac{p_0 V^2}{D}\left[\frac{1}{\omega_{1,0} - \widetilde{\varepsilon}_{f,0}} - \frac{1}{\mu - \widetilde{\varepsilon}_{f,0}}\right] \tag{B.12}$$

The expressions above can be further simplified by using the expression for $\rho_0^{ff}(\omega)$ and n_f:

$$C_0 = g_f \rho_0^{ff}(\omega_{1,0})\left(\frac{\overline{E}_0(-D) - \Delta_0(-D)}{\Delta_0(-D)}\right) + 2 g_f \rho_0^{ff}(\mu) \tag{B.13}$$

$$C_1 = \rho_0^{ff}(\omega_{1,0}) \frac{V^2}{2\Delta_0(-D)} + \frac{n_f}{p_0} \tag{B.14}$$

μ in the upper energy band

Let us now deal with the case in which the chemical potential μ in the absence of magnetic field lies in the upper energy band. In this case the expression for the f-electron magnetization is:

$$m_f = \int_{\omega_{1,\uparrow}}^{\omega_{2,\uparrow}} d\omega \rho_\uparrow^{ff}(\omega) + \int_{\omega_{3,\downarrow}}^{\mu} d\omega \rho_\uparrow^{ff}(\omega) - \left(\int_{\omega_{1,\downarrow}}^{\omega_{2,\downarrow}} d\omega \rho_\downarrow^{ff}(\omega) + \int_{\omega_{3,\downarrow}}^{\mu} d\omega \rho_\downarrow^{ff}(\omega)\right) \tag{B.15}$$

Performing a similar calculation as done in the previous case, one gets the following equation:

$$\chi_0 = \frac{B_0}{1 - B_1} \tag{B.16}$$

In this case the coefficients are:

$$B_0 = g_f \left[\rho_0^{ff}(\omega_{1,0})\left(\frac{\overline{E}_0(-D) - \Delta_0(-D)}{\Delta_0(-D)}\right) - \rho_0^{ff}(\omega_{2,0})\left(\frac{\overline{E}_0(+D) - \Delta_0(+D)}{\Delta_0(+D)}\right) + \rho_0^{ff}(\omega_{3,0})\left(\frac{\overline{E}_0(-D) + \Delta_0(-D)}{\Delta_0(-D)}\right) + 2\rho_0^{ff}(\mu)\right] \tag{B.17}$$

$$B_1 = \frac{V^2}{2}\left[\rho_0^{ff}(\omega_{1,0})\frac{1}{\Delta_0(-D)} - \rho_0^{ff}(\omega_{2,0})\frac{1}{\Delta_0(+D)} - \rho_0^{ff}(\omega_{3,0})\frac{1}{\Delta_0(-D)}\right] + \frac{n_f}{p_0} \tag{B.18}$$

In both cases the expressions for χ_0 must be evaluated numerically from the self-consistent parameters determined in Section 4.1.

Appendix C

Some results on Bethe lattices

Non-interacting density of states

In this Appendix the expressions for the density of states of free electrons in a Bethe lattice of coordination Z. will be derived. We start by the tight-binding hamiltonian:

$$\mathcal{H} = -\sum_{ij} t_{ij} c_i^\dagger c_j \tag{C.1}$$

All the hoppings between nearest neighbors will be considered as equal, so $t_{ij} = t/2\sqrt{K}$ ($K = Z - 1$) if i and j are adjacent sites. We follow the same lines in Section 7.2.2 and define a self-energy associated to the non-local term (hopping). The electronic Green's function in a site i is written as:

$$G_{ii}(\omega) = \frac{1}{\omega - \Delta_i(\omega)} \tag{C.2}$$

The expression of $\Delta_i(\omega)$ is:

$$\Delta_i(\omega) = t^2 \sum_{j=1}^{Z} G_{jj}^{(i)}(\omega) \tag{C.3}$$

The function $G_{jj}^{(i)}(\omega)$ is the cavity Green's function (defined in Section 7.2.2), i.e. the Green's function at the site j excluding the site i of the system . It has the same form as Eq. C.9:

$$G_{jj}^{(i)}(\omega) = \frac{1}{\omega - \Delta_j^{(i)}(\omega)} \tag{C.4}$$

Note that:

$$\Delta_j^{(i)}(\omega) = t^2 \sum_{k=1}^{K} G_{kk}^{(ij)}(\omega) = t^2 \sum_{k=1}^{K} G_{kk}^{(j)}(\omega) \tag{C.5}$$

Here the sum is performed over $K = Z - 1$ neighboring sites, since one neighbor is already excluded. The last equality holds because in a Bethe lattice there is only one path that connects the sites i and k (through the site j), so $G_{kk}^{(ij)}(\omega) = G_{kk}^{(j)}(\omega)$.

For an homogeneous system (no disorder), we can re-express $G_{jj}^{(i)}(\omega) = G_{ii}^{(0)}(\omega)$ and $\Delta_j^{(i)}(\omega) = \Delta_i^{(0)}(\omega)$ for all i and j. We can combine Eqs. C.4 and C.5 in a closed expression

$$\Delta_i^{(0)}(\omega) = \frac{t^2 K}{\omega - \Delta_i^{(0)}(\omega)}, \tag{C.6}$$

whose solution is

$$\Delta_i^{(0)}(\omega) = \frac{\omega}{2}\left[1 - \sqrt{1 - \frac{4t^2K}{\omega^2}}\right]. \tag{C.7}$$

The negative sign of the square root is chosen to give $\Delta_i^{(0)}(\omega) = 0$ if $t = 0$. Equation C.3 now gives:

$$\Delta_i(\omega) = \frac{2t^2 Z}{\omega\left[1 + \sqrt{1 - \frac{4t^2K}{\omega^2}}\right]} = \frac{Z\omega}{2K}\left[1 - \sqrt{1 - \frac{4t^2K}{\omega^2}}\right] \tag{C.8}$$

Finally, one can get the expression for the local Green's function as:

$$\begin{aligned} G_{ii}(\omega) &= \frac{1}{\omega - \frac{Z\omega}{2K}\left[1 - \sqrt{1 - \frac{4t^2K}{\omega^2}}\right]} \\ &= \frac{2K}{(Z-2)\omega + Z\omega\sqrt{1 - \frac{4t^2K}{\omega^2}}} \\ &= \frac{(Z-2)\omega - Z\omega\sqrt{1 - \frac{4t^2K}{\omega^2}}}{2\left(Z^2t^2 - \omega^2\right)} \end{aligned} \tag{C.9}$$

The density of states is obtained from the imaginary part of the retarded Green's function:

$$\rho(\omega) = -\frac{1}{\pi}\mathrm{Im}\left(G_{ii}(\omega + i0^+)\right) = \frac{\sqrt{\omega^2 - 4Kt^2}}{2\pi(Zt^2 - \omega^2/Z)} \tag{C.10}$$

In Figure C.1 we plot the density of states for Bethe lattices of different coordination numbers, including the semi-elliptic density of states (for $Z \to \infty$). Interestingly, the density of states for $Z = 5$ is quite similar to the flat density of states.

Lastly, the reciprocal function of $G(\omega)$, defined as $R[G(x)] = x$, is given by the solution of

$$R^2 + \frac{Z-2}{G}R - \left(Z^2t^2 + \frac{Z-1}{G^2}\right) = 0, \tag{C.11}$$

which gives:

$$R = -\left(\frac{Z-2}{2G}\right) + \frac{Z}{2G}\sqrt{1 + 4t^2G^2} \tag{C.12}$$

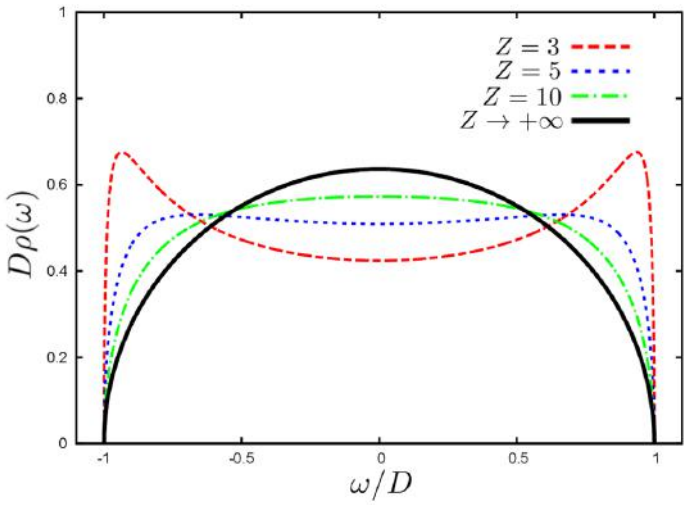

Figure C.1: Density of states for free-electrons in a Bethe lattice of different coordination number Z. The energy is renormalized by the half-bandwidth $D=2\sqrt{K}t$ $(K=Z-1)$.

Limit of infinite coordination number

The expressions above simplify in the $Z \to \infty$ limit. In this case one must renormalize the hopping parameters $t \to t/\sqrt{Z}$ to keep the kinetic energy finite. Using this scaling and taking $Z \to \infty$ in Equation C.9, the following Green's function is obtained:

$$G_{ii}(\omega) = \frac{\omega - \sqrt{1 - \frac{4t^2}{\omega^2}}}{2t^2} \tag{C.13}$$

The corresponding density of states for the expression above has the well-known semi-elliptic form:

$$\rho_i(\omega) = \frac{\sqrt{\omega^2 - 4t^2}}{2\pi t^2} \tag{C.14}$$

Lastly, one can show that the reciprocal function of $G(\omega)$ in the limit of infinite coordination number is simply:

$$R = t^2 G + \frac{1}{G} \tag{C.15}$$

Appendix D

Matsubara's sum at zero temperature

In this Appendix it is shown how to calculate Matsubara's sums at zero temperature in order to solve the mean-field equations for the Kondo problem (Eqs. 7.15 and 7.16). The calculations performed here are developed in details in Chapter 3 of Ref.[2].

Let us take for example $G_{ii}^{ff}(\tau = 0^-)$. Using its Fourier transformation, we have ($\beta \equiv 1/T$ is the inverse temperature):

$$G_{ii}^{ff}(\tau = 0^-) = \lim_{\tau \to 0^-} \frac{1}{\beta} \sum_{i\omega_n} e^{-i\omega_n \tau} G_{ii}^{ff}(i\omega_n), \tag{D.1}$$

The sum in the right hand side extends over the infinite set of fermionic Matsubara's frequencies:

$$i\omega_n = i\frac{(2n+1)\pi}{\beta}. \tag{D.2}$$

Using the property $G_{ii}^{ff}(i\omega_n) = \left(G_{ii}^{ff}(-i\omega_n)\right)^*$ and trigonometric relations, the sum can be restricted to positive frequencies

$$G_{ii}^{ff}(\tau = 0^-) = \lim_{\tau \to 0^-} \frac{2}{\beta} \sum_{\omega_n > 0} \left[\cos(\omega_n \tau) \mathrm{Re}\left(G_{ii}^{ff}(i\omega_n)\right) + \sin(\omega_n \tau) \mathrm{Im}\left(G_{ii}^{ff}(i\omega_n)\right)\right] \tag{D.3}$$

The limit $\tau \to 0^-$ can be taken directly in the first term of the sum, since $G_{ii}^{ff}(i\omega_n) \sim 1/(i\omega_n)$ for large ω_n and $\mathrm{Re}\left(G_{ii}^{ff}(i\omega_n)\right)$ tends to zero faster than $1/\omega_n$ as ω_n tends to infinity. The second term has important contributions only when ω_n is large (i.e., $\omega_n \tau \sim 1$), so we can replace the imaginary part of $G_{ii}^{ff}(i\omega_n)$ by its asymptotic value $1/(i\omega_n)$ and transforms the sum into an integral (if $T = 0$) through:

$$\frac{1}{\beta} \sum_{\omega_n > 0} \to \int_0^{+\infty} \frac{d(i\omega)}{2\pi} \tag{D.4}$$

Then[1]:

$$\lim_{\tau\to 0^-}\frac{2}{\beta}\sum_{\omega_n>0}\sin(\omega_n\tau)\mathrm{Im}\left(G_{ii}^{ff}(i\omega_n)\right)=\lim_{\tau\to 0^-}\left[-\frac{1}{\pi}\int_0^{+\infty}\frac{\sin(\omega\tau)}{\omega}\right]=\frac{1}{2} \tag{D.5}$$

After the considerations above, one can finally write:

$$G_{ii}^{ff}(\tau=0^-)=\frac{2}{\beta}\sum_{\omega_n>0}\mathrm{Re}\left(G_{ii}^{ff}(i\omega_n)\right)+\frac{1}{2} \tag{D.6}$$

In principle the sum in Equation D.6 can be performed numerically for a given temperature T, although the convergence can be an issue at low temperatures. We are interested in the zero temperature behavior of the system, therefore it is desirable to transform the sum at finite T into its zero temperature equivalent. This is done by the relation in Eq. D.4, leading to:

$$G_{ii}^{ff}(\tau=0^-)=\frac{1}{\pi}\int_0^{+\infty}d\omega\mathrm{Re}\left(G_{ii}^{ff}(\omega)\right)+\frac{1}{2} \tag{D.7}$$

Here the integration is performed along the positive imaginary axis and the index n was dropped to explicit that it a continuous variable (in contrast to the finite T frequencies). Analogously one can evaluate $\left\langle c_i^\dagger c_i\right\rangle$, which determines the local occupation of conduction electrons, by:

$$\left\langle c_i^\dagger c_i\right\rangle=G_{ii}^{cc}(\tau=0^-)=\frac{1}{\pi}\int_0^{+\infty}d\omega\mathrm{Re}\left(G_{ii}^{cc}(\omega)\right)+\frac{1}{2} \tag{D.8}$$

The third average to be computed is $< f_i^\dagger c_i >$. The only difference from the other two averages comes from the asymptotic limit of the mixed Green's function [2] $G_{ii}^{cf}(i\omega_n)\sim 1/(i\omega_n)^2$ for large ω_n. Based on the same lines of the argument given between Eq.D.3 and Eq.D.4, one can show that the factor asymptotic limit of the first term in Eq.D.3 is zero (instead of $1/2$). Then:

$$G_{ii}^{cf}(\tau=0^-)=\frac{1}{\pi}\int_0^{+\infty}d\omega\mathrm{Re}\left(G_{ii}^{cf}(\omega)\right) \tag{D.9}$$

[1] Here it was used $\int_0^{+\infty}\frac{\sin(\omega\tau)}{\omega}=\frac{\pi}{2}sign(\tau)$

[2] The functional form of the Green's function is presented in its matrix form in Eqs.7.26.

Appendix E

Some limits of $\phi_i(\omega)$

In Chapter 8 we have introduced a site-dependent complex function $\phi_i(\omega)$ formally defined through the relation:

$$G_{ii}^{cc}(\omega) \equiv G_0(\omega - \phi_i(\omega)) \tag{E.1}$$

The interpretation of its real part at the Fermi energy was provided in Section 8.1: it measures the effective position of the conduction electron level with respect to the non-interacting density of states, indicating if the site behaves locally as a "conductor" or "insulator". Given that the expression for $\phi_i(\omega)$ in Equation 8.5 is not simple to understand, it is desirable to analyze in details some limiting cases in which $\phi_i(\omega)$ has a simpler form. In this Appendix, two cases will be considered: the Kondo Lattice limit ($x = 1$) and the $Z \to \infty$ limit. The former case served as the starting point for the definition of $\phi_i(\omega)$, although it corresponds to the *clean* case (without disorder).

Kondo Lattice

The first example that shows what is $\phi_i(\omega)$ comes from the Kondo lattice within the mean-field approximation. In this case the system possesses translational invariance and the local Green's functions are the same for all sites, namely:

$$G_{KL}^{cc}(\omega) = \frac{1}{\omega + \mu - \Delta_{KL}(\omega) - \frac{r_{KL}^2}{\omega + \lambda_{KL}}} \tag{E.2}$$

$$G_{KL}^{ff}(\omega) = \frac{1}{\omega + \lambda_{KL} - \frac{r_{KL}^2}{\omega + \mu - \Delta_{KL}(\omega)}} \tag{E.3}$$

Here r_{KL}^2 and λ_{KL} are the mean-field parameters for the Kondo lattice to be determined self-consistently and $\Delta_{KL}(\omega)$ is the bath function given by:

$$\Delta_{KL}(\omega) = Zt^2 G_{KL}^{cc,(o)}(\omega) \tag{E.4}$$

The structure of these equations for $G_{KL}^{cc}(\omega)$ is the same as seen in Equations C.9 to C.6 in Appendix C. In fact, performing the *change of variable* $\omega \to \omega + \mu - \frac{r_{KL}^2}{\omega + \lambda_{KL}}$, one concludes

that:

$$G^{cc}_{KL}(\omega) = G_0\left(\omega + \mu - \frac{r^2_{KL}}{\omega + \lambda_{KL}}\right) \tag{E.5}$$

The equation above permit us to write the complete c-electron Green's function for the Kondo Lattice in terms of the non-interacting c-electrons Green's function. This result, here explicitly developed for the Bethe Lattice, is independent of the lattice structure, being a general property of the mean-field approximation. Comparing Eqs.E.5 and E.1, we have:

$$\phi_{KL}(\omega) = \frac{r^2_{KL}}{\omega + \lambda_{KL}} + \mu \tag{E.6}$$

Note that $\phi_{KL}(0)$ is a real number at the Fermi energy. If the shift $\phi_{KL}(0) = r^2_{KL}/\lambda_{KL}$ is sufficiently large so that G_0 in Eq. E.5 is zero, then the chemical potential for the Kondo lattice lies in the hybridization gap and the system is in an insulating state (Kondo Insulator). For instance, this situation happens in the half-filled($n_c = 1$) Kondo lattice: the mean-field parameter λ_{KL} is zero and the shift $-r^2_{KL}/\lambda_{KL}$ diverges [1]. As a consequence, the function $\phi_i(0)$ can be seen as a local generalization of this parameter in which not only the Kondo interaction is considered, but also different environments.

Limit of large coordination number

A second limit in which $\phi_i(\omega)$ has a simple expression (and, equivalently, a simple interpretation) is when the coordination number is $Z \to \infty$. In this limit, the Bethe lattice relations derived in Appendix C are simpler. For instance, using the reciprocal function in Eq. C.15, one gets for a Kondo site i:

$$\phi_i(\omega) = \Delta_i(\omega) - t^2 G^{cc}_{ii}(\omega) + \frac{r^2_i}{\omega + \lambda_i} + \mu \tag{E.7}$$

If $Z \to \infty$, then the bath function $\Delta_i(\omega)$ is a sum over infinity lattice sites, which is the average value of $G^{cc}(\omega)$.

$$\Delta_i(\omega) = t^2 \overline{G^{cc}_{ii}}(\omega) \tag{E.8}$$

This limit corresponds to the so called Coherent Potential Approximation. The expression of $\phi_i(\omega)$ in a Kondo site is then:

$$\phi_i(\omega) = t^2\left(\overline{G^{cc}_{ii}}(\omega) - G^{cc}_{ii}(\omega)\right) + \frac{r^2_i}{\omega + \lambda_i} + \mu \tag{E.9}$$

From the expression above we see that $\phi_i(\omega)$ has two contributions. The first one measures the difference between the local Green's function $G^{cc}_{ii}(\omega)$ and its average value. The second contribution is non-zero only for Kondo sites and measures the scattering potential from the local moment on the conduction electrons. This term is a real quantity at the Fermi energy.

The imaginary part of $\phi_i(0)$ at the Fermi energy has the following expression:

$$\mathrm{Im}\phi_i(0) = \pi t^2\left(\rho^c_i(0) - \overline{\rho^c}(0)\right) \tag{E.10}$$

[1] This argument can be extended for $n_c > 1$ by invoking particle-hole symmetry.

The sign of $\mathrm{Im}\phi_i(0)$ can be whether positive or negative, depending on how much the local density of states is shifted with respect to its average. For a finite value of Z, the expression of $\phi_i(\omega)$ is complicated, but one can speculate from its $Z \to \infty$ value that $\mathrm{Im}\phi_i(0)$ would measure the local density of states shift compared to the local bath at the Fermi energy ($\Delta_i(0)$), being the last quantity also site-dependent in a disordered system.

Appendix F

Renormalized Perturbation Expansion

In this Appendix we will derive a general expansion for hybridization function $\Delta_i(i\omega_n)$ for a disordered system in terms of cavity Green's functions, to be employed in Section 7.2.2. The method employed for this purpose is the so-called renormalized perturbation expansion, which is discussed in details in the Appendix F of Reference [143].

For the sake of simplicity we will consider here the tight-binding hamiltonian:

$$\mathcal{H} = \sum_i \epsilon_i c_i^\dagger c_i - \sum_{i,j} t_{ij} c_i^\dagger c_j \tag{F.1}$$

This hamiltonian is written in the usual notation (with spin index omitted). ϵ_i is a local energy and t_{ij} is the hopping integral, which is non-zero only for nearest-neighbors sites i and j. We are going to consider the local term as an unperturbed hamiltonian $\mathcal{H}_0$ and the hopping term to be treated as a perturbation $\mathcal{H}_1$. The Green's function for the unperturbed hamiltonian is diagonal in site representation and it is given by:

$$g_{ii}(i\omega_n) = \frac{1}{i\omega_n - \epsilon_i} \tag{F.2}$$

The expression for the full Green's function $G_{ij}(i\omega_n)$ is given by a Dyson equation:

$$G_{ij}(i\omega_n) = g_{ij}(i\omega_n) + \sum_{k,l} g_{ik}(i\omega_n) t_{kl} G_{lj}(i\omega_n) \tag{F.3}$$

We remind that $g_{ij}(i\omega_n) = \delta_{ij} g_{ii}(i\omega_n)$. The equation above can be written as the following infinite serie:

$$G_{ij}(\omega) = g_{ij}(\omega) + \sum_{k,l} g_{ik}(\omega)\ t_{kl}\ g_{lj}(\omega) + \sum_{k,l,m,n} g_{ik}(\omega)\ t_{kl}\ g_{lm}(\omega)\ t_{mn}\ g_{nj}(\omega) + ... \tag{F.4}$$

The infinite terms on the right hand side of Eq. F.4 describe all the possible paths that an electron can take to go from site i to site j. Through the whole set of paths one can

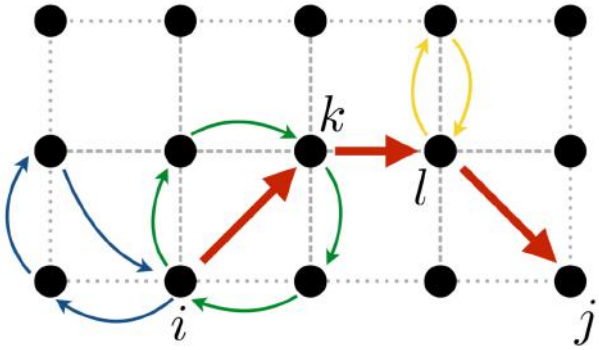

Figure F.1: Schematic picture representing paths connecting the sites i and j in a square lattice, which is related to $G_{ij}(i\omega_n)$ in Eq.F.5. The skeleton path $i \to k \to l \to j$ (red thick arrows) is a path that does not contain any loop. Three loops corrections to this particular skeleton path are shown in the thin arrows and renormalizes this path, as it is explained in the text. Note that the loop correction in green cannot be taken into account twice in sites i and k, then cavity Green's functions as $G^{(i)}_{kk}(i\omega_n)$ must be used to avoid double counting.

identify *skeleton paths*, in which each site is visited by the electron one time only (the path is *self-avoiding*). The paths containing loops can be "decomposed" in terms of a skeleton path multiplied by a loop correction, then the expansion in Eq.F.4 can be resummed in terms of skeleton paths with appropriate loops corrections.

The loops corrections correspond to all intermediate paths that start and return to the same visited site in the skeleton path, as represented bu the thin lines in Fig. F.1. They must be computed systematically in order to avoid double-counting. For example, let us consider the skeleton path $i \to k \to l \to j$ in $G_{ij}(i\omega_n)$ (the thick red lines in Fig. F.1). The loop corrections for the first site(i) correspond to all the paths starting and ending in this site, which corresponds to $G_{ii}(i\omega_n)$. The corrections for the next visited site contain all the paths starting and ending in k, *except* those passing through i, which are already accounted in the correction for i (for example, the green path in Figure F.1). For that reason, the loop corrections in k is given by the *cavity Green's function* $G^{(i)}_{kk}(i\omega_n)$, which is the local Green's function in k having excluded the site i of the problem [1]. The corrections in the other visited sites follow the same procedure and Eq. F.4 can be written as:

$$G_{ij}(i\omega_n) = \sum_{\substack{\text{skeleton paths} \\ i \to j}} G_{ii}(i\omega_n) t_{ik} G^{(i)}_{kk}(i\omega_n) t_{kl} G^{(i,k)}_{ll}(i\omega_n) t_{lm} ... G^{(i,k,l,m,...)}_{jj}(i\omega_n) \tag{F.5}$$

For $G_{ii}(i\omega_n)$, we can write Eq.F.5 as

$$G_{ii}(i\omega_n) = g_{ii}(i\omega_n) + G_{ii}(i\omega_n)\Delta_i(i\omega_n)g_{ii}(i\omega_n), \tag{F.6}$$

[1] The exclusion of i can be formally done for the hamiltonian in Eq. F.1 by taking $\epsilon_i \to \infty$

in which we have defined $\Delta_i(i\omega_n)$ as:

$$\Delta_i(i\omega_n) \equiv \sum_{\substack{\text{skeleton paths} \\ i\to i}} t_{ik}G^{(i)}_{kk}(i\omega_n)t_{kl}G^{(i,k)}_{ll}(i\omega_n)t_{lm}...t_{zi} \tag{F.7}$$

Equation F.6 can be rewritten by using Eq.F.2:

$$G_{ii}(i\omega_n) = \frac{1}{i\omega_n - \epsilon_i - \Delta_i(i\omega_n)} \tag{F.8}$$

The Equations F.7 and F.8 are the principal result of this appendix. The function $\Delta_i(i\omega_n)$ takes into account all the hopping terms starting and ending in the site i through a summation over self-avoiding paths in the lattice. The drawback of writing such sum is in its coefficients, which contains cavity Green's functions of many (infinite) "orders". However the same procedure described above can be used to determine $G^{(i)}_{kk}(i\omega_n)$ or any other cavity Green's function. Explicitly:

$$G^{(i)}_{kk}(i\omega_n) = \frac{1}{i\omega_n - \epsilon_k - \Delta^{(i)}_k(i\omega_n)} \tag{F.9}$$

$$\Delta^{(i)}_{kk}(i\omega_n) = \sum_{\substack{\text{skeleton paths} \\ k\to k}} t_{kl}G^{(i,k)}_{ll}(i\omega_n)t_{lm}G^{(i,k,l)}_{mm}(i\omega_n)t_{mn}...t_{zk} \tag{F.10}$$

In general, there is an infinite number of equations needed to determine all Green's functions for an infinite and regular lattice, then the equations above are not very useful. One way to simplify them is to consider a Bethe lattice[146, 143], what we will do in the following.

Particular case: Bethe lattice

Bethe lattice is a loop-free structure, which means that there is a unique path connecting two sites i and j in the lattice. Thus the only skeleton path that keeps in Eq.F.7 is $i \to j \to i$, so:

$$\Delta_i(i\omega_n) = \sum_{j=1}^{Z} t_{ij}G^{(i)}_{jj}(i\omega_n)t_{ji} = \sum_{j=1}^{Z} t^2 G^{(i)}_{jj}(i\omega_n) \tag{F.11}$$

In this equation, the sum is performed on the j sites neighbors of i (Z is the lattice coordination number). We also considered that all the hopping integrals are equal to t. Similarly, we have for $\Delta^{(i)}_{jj}(i\omega_n)$:

$$\Delta^{(i)}_j(i\omega_n) = \sum_{k=1}^{Z-1} t^2 G^{(ij)}_{kk}(i\omega_n) = \sum_{k=1}^{Z-1} t^2 G^{(j)}_{kk}(i\omega_n) \tag{F.12}$$

Here the sum is over $Z-1$ sites, given that one neighboring site was excluded. In the last equality we use the relation $G^{(ij)}_{kk}(i\omega_n) = G^{(j)}_{kk}(i\omega_n)$, which is valid in the Bethe lattice since the exclusion of site j automatically excludes i. All the cavity Green's functions with two or more excluded sites are equivalent to one with a single site removed and the hierarchy of equations is reduced to Eqs. F.11 and F.12.

Bibliography

[1] A. C. Hewson, *The Kondo problem to heavy fermions*, Vol. 2 (Cambridge University Press, 1997).

[2] A. A. Abrikosov, L. P. Gorkov, and I. E. Dzyaloshinski, *Methods of quantum field theory in statistical physics* (Dover Publications, 1975).

[3] G. D. Mahan, *Many-Particle Physics* (Springer Science & Business Media, 2000).

[4] P. W. Anderson, Phys. Rev. **124**, 41 (1961).

[5] E. C. Stoner, Proc. R. Soc. A , 372 (1938).

[6] J. R. Schrieffer and P. A. Wolff, Phys. Rev. **149**, 491 (1966).

[7] J. Kondo, Progress of Theoretical Physics **32**, 37 (1964).

[8] W. de Haas, J. de Boer, and G. van dën Berg, Physica **1**, 1115 (1934).

[9] P. W. Anderson, J. Phys. C: Solid State Phys. **3**, 2436 (1970).

[10] K. G. Wilson, Rev. Mod. Phys. **47**, 773 (1975).

[11] B. Barbara, J. Boucherle, J. Buevoz, M. Rossignol, and J. Schweizer, Solid State Communications **24**, 481 (1977).

[12] S. Doniach, Physica B+ C **91**, 231 (1977).

[13] S. Doniach, in *Theoretical and Experimental Aspects of Valence Fluctuations and Heavy Fermions* (Springer, 1987) pp. 179–185.

[14] P. Coleman, "Heavy fermions: Electrons at the edge of magnetism," in *Handbook of Magnetism and Advanced Magnetic Materials* (John Wiley & Sons, Ltd, 2007).

[15] P. Gegenwart, Q. Si, and F. Steglich, nature physics **4**, 186 (2008).

[16] Q. Si and F. Steglich, Science **329**, 1161 (2010).

[17] F. Steglich, J. Aarts, C. D. Bredl, W. Lieke, D. Meschede, W. Franz, and H. Schäfer, Phys. Rev. Lett. **43**, 1892 (1979).

[18] G. R. Stewart, Rev. Mod. Phys. **73**, 797 (2001).

[19] H. v. Löhneysen, T. Pietrus, G. Portisch, H. G. Schlager, A. Schröder, M. Sieck, and T. Trappmann, Phys. Rev. Lett. **72**, 3262 (1994).

[20] G. R. Stewart, Rev. Mod. Phys. **56**, 755 (1984).

[21] K. Andres, J. E. Graebner, and H. R. Ott, Phys. Rev. Lett. **35**, 1779 (1975).

[22] S. Cotton, *Lanthanide and actinide chemistry* (John Wiley & Sons, 2013).

[23] J. Lawrence, P. Riseborough, and R. Parks, Reports on Progress in Physics **44**, 1 (1981).

[24] K. Gschneidner, L. Eyring, and G. Lander, *Handbook on the physics and chemistry of rare earths*, Vol. 32 (Elsevier, 2002).

[25] E. Franceschi and G. L. Olcese, Phys. Rev. Lett. **22**, 1299 (1969).

[26] K. Gschneidner and R. Smoluchowski, Journal of the Less Common Metals **5**, 374 (1963).

[27] J.-P. Rueff *et al.*, Phys. Rev. Lett. **96**, 237403 (2006).

[28] J. M. Lock, Proc. Phys. Soc. B **70**, 566 (1957).

[29] C. Varma, Rev. Mod. Phys. **48** (1976).

[30] D. Khomskii, Physics-Uspekhi **879** (1979).

[31] J. Coey and O. Massenet, in *Valence Instabilities and Related Narrow-Band Phenomena*, edited by R. Parks (Springer US, 1977) pp. 211–228.

[32] M. B. Maple and D. Wohlleben, Phys. Rev. Lett. **27**, 511 (1971).

[33] M. B. Maple and D. Wohlleben, AIP Conference Proceedings **18**, 447 (1974).

[34] B. Sales, Journal of Low Temperature Physics **28**, 107 (1977).

[35] I. Nowik, in *Valence Instabilities and Related Narrow-Band Phenomena*, edited by R. Parks (Springer US, 1977) pp. 261–273.

[36] M. Löwenhaupt and E. Holland-Moritz, Journal of Applied Physics **50**, 7456 (1979).

[37] J.-P. Rueff, *Strongly Correlated Electrons at High Pressure*, Habilitation à diriger des recherches, Université Pierre et Marie Curie - Paris VI (2007).

[38] A. Fernandez-Pañella, *Ytterbium-based heavy fermion compounds under extreme conditions : a new instrumentation to tackle fundamental questions*, Ph.D. thesis, Université de Grenoble (2012).

[39] M. Campagna, G. Wertheim, and E. Bucher, in *Rare Earths*, Structure and Bonding, Vol. 30 (Springer Berlin Heidelberg, 1976) pp. 99–140.

[40] F. D. M. Haldane, Phys. Rev. Lett. **40**, 416 (1978).

[41] L. Falicov and J. Kimball, Phys. Rev. Lett. **22**, 997 (1969).

[42] M. Neupane *et al.*, Nature Comm. **4** (2013), 10.1038/ncomms3991.

[43] C. G. Da Silva and L. Falicov, Solid State Communications **17**, 1521 (1975).

[44] D. Khomskii and A. Kocharjan, Solid State Communications **18**, 985 (1976).

[45] A. Hewson and P. Riseborough, Solid State Communications **22**, 379 (1977).

[46] I. Singh, A. Ahuja, and S. Joshi, Solid State Communications **34**, 65 (1980).

[47] J. Freericks and V. Zlatić, Rev. Mod. Phys. **75**, 1333 (2003).

[48] M. Croft, J. H. Weaver, D. J. Peterman, and A. Franciosi, Phys. Rev. Lett. **46**, 1104 (1981).

[49] A. Franciosi, J. H. Weaver, N. Martensson, and M. Croft, Phys. Rev. B **24**, 3651 (1981).

[50] S. M. Shapiro, J. D. Axe, R. J. Birgeneau, J. M. Lawrence, and R. D. Parks, Phys. Rev. B **16**, 2225 (1977).

[51] J. W. Allen and R. M. Martin, Phys. Rev. Lett. **49**, 1106 (1982).

[52] M. Lavagna, C. Lacroix, and M. Cyrot, Physics Letters A **90**, 210 (1982).

[53] C. Lacroix and M. Cyrot, Phys. Rev. B **20**, 1969 (1979).

[54] K. Held, A. K. McMahan, and R. T. Scalettar, Phys. Rev. Lett. **87**, 276404 (2001).

[55] A. K. McMahan, K. Held, and R. T. Scalettar, Phys. Rev. B **67**, 075108 (2003).

[56] A. K. McMahan, Phys. Rev. B **72**, 115125 (2005).

[57] G. Kotliar, S. Y. Savrasov, K. Haule, V. S. Oudovenko, O. Parcollet, and C. A. Marianetti, Rev. Mod. Phys. **78**, 865 (2006).

[58] Y. Onishi and K. Miyake, J. Phys Soc. Jpn. **69**, 3955 (2000).

[59] Y. Onishi and K. Miyake, Physica B: Condensed Matter **281**, 191 (2000).

[60] A. Holmes, D. Jaccard, and K. Miyake, Phys. Rev. B **69**, 024508 (2004).

[61] S. Watanabe, A. Tsuruta, K. Miyake, and J. Flouquet, Phys. Rev. Lett. **100**, 236401 (2008).

[62] S. Watanabe and K. Miyake, J. Phys Soc. Jpn. **79**, 033707 (2010).

[63] S. Watanabe, A. Tsuruta, K. Miyake, and J. Flouquet, J. Phys Soc. Jpn. **78**, 104706 (2009).

[64] S. Watanabe, M. Imada, and K. Miyake, J. Phys Soc. Jpn. **75**, 043710 (2006).

[65] I. Hagymási, J. Sólyom, and O. Legeza, Phys. Rev. B **90**, 125137 (2014).

[66] Y. Saiga, T. Sugibayashi, and D. Hirashima, J. Phys Soc. Jpn. **77**, 114710 (2008).

[67] V.-N. Phan, A. Mai, and K. Becker, Phys. Rev. B **82**, 045101 (2010).

[68] S. Watanabe and K. Miyake, J. Phys.: Condens. Matter **23**, 094217 (2011).

[69] J. Hubbard, Proc. R. Soc. A **276**, 238 (1963).

[70] J. Hubbard, Proc. R. Soc. A **277**, 237 (1964).

[71] F. Gebhard, *Metal-Insulator Transitions* (Springer, 1997).

[72] D. Zubarev, Soviet Physics Uspekhi **3**, 320 (1960).

[73] S. Burdin, *Le réseau Kondo à basse température : du liquide de Fermi au liquide de spin*, Ph.D. thesis, Université de Grenoble (2001).

[74] R. L. Burden and J. D. Faires, Numerical Analysis. Prindle, Weber & Schmidt, Boston, MA., pp. x **676** (1985).

[75] W. Nolting and A. Ramakanth, *Quantum theory of magnetism* (Springer Science & Business Media, 2009).

[76] G. G. Reddy, D. Meyer, S. Schwieger, A. Ramakanth, and W. Nolting, J. Phys.: Condens. Matter **12**, 7463 (2000).

[77] N. Majlis, *The quantum theory of magnetism* (World Scientific, 2000).

[78] J. Flouquet and H. Harima, ArXiv e-prints (2009).

[79] A. Fernandez-Pañella, D. Braithwaite, B. Salce, G. Lapertot, and J. Flouquet, Phys. Rev. B **84**, 134416 (2011).

[80] A. Fernandez-Pañella, V. Balédent, D. Braithwaite, L. Paolasini, R. Verbeni, G. Lapertot, and J.-P. Rueff, Phys. Rev. B **86**, 125104 (2012).

[81] A. Miyake, F. Honda, R. Settai, K. Shimizu, and Y. Ōnuki, J. Phys Soc. Jpn. **81**, SB054 (2012).

[82] A. Yasui, S.-I. Fujimori, I. Kawasaki, T. Okane, Y. Takeda, Y. Saitoh, H. Yamagami, A. Sekiyama, R. Settai, T. D. Matsuda, Y. Haga, and Y. Ōnuki, Phys. Rev. B **84**, 195121 (2011).

[83] T. Mazet, D. Malterre, M. François, C. Dallera, M. Grioni, and G. Monaco, Phys. Rev. Lett. **111**, 096402 (2013).

[84] T. Mazet, D. Malterre, M. François, L. Eichenberger, M. Grioni, C. Dallera, and G. Monaco, Phys. Rev. B **92**, 075105 (2015).

[85] C. Segre, M. Croft, J. Hodges, V. Murgai, L. Gupta, and R. Parks, Physical Review Letters **49**, 1947 (1982).

[86] L. Fournes, B. Chevalier, B. Lloret, and J. Etourneau, Zeitschrift für Physik B Condensed Matter **75**, 501 (1989).

[87] V. Guritanu, S. Seiro, J. Sichelschmidt, N. Caroca-Canales, T. Iizuka, S. Kimura, C. Geibel, and F. Steglich, Physical review letters **109**, 247207 (2012).

[88] S. Seiro and C. Geibel, J. Phys.: Condens. Matter **23**, 375601 (2011).

[89] A. Mitsuda, S. Hamano, N. Araoka, H. Yayama, and H. Wada, J. Phys Soc. Jpn. **81**, 023709 (2012).

[90] J. Melsen, J. Wills, B. Johansson, and O. Eriksson, Journal of Alloys and Compounds **209**, 15 (1994).

[91] P. Coleman, AIP Conference Proceedings **629**, 79 (2002).

[92] A. Sumiyama, Y. Oda, H. Nagano, Y. Onuki, K. Shibutani, and T. Komatsubara, J. Phys Soc. Jpn. **55**, 1294 (1986).

[93] Y. Ōnuki and T. Komatsubara, Journal of magnetism and magnetic materials **63**, 281 (1987).

[94] P. Nozières, Journal of Low Temperature Physics **17**, 31 (1974).

[95] P. Nozières, Ann. Phys. Fr. **10**, 19 (1985).

[96] P. Nozières, Eur. Phys. J. B **6**, 447 (1998).

[97] S. Burdin, A. Georges, and D. R. Grempel, Phys. Rev. Lett. **85**, 1048 (2000).

[98] S. Burdin and V. Zlatić, Phys. Rev. B **79**, 115139 (2009).

[99] T. Costi and N. Manini, Journal of Low Temperature Physics **126**, 835 (2002).

[100] C. Lacroix, Solid State Communications **54**, 991 (1985).

[101] M. Oshikawa, Phys. Rev. Lett. **84**, 3370 (2000).

[102] P. d. V. du Plessis, A. Strydom, R. Troc, T. Cichorek, C. Marucha, and R. Gers, J. Phys.: Condens. Matter **11**, 9775 (1999).

[103] M. Maple, M. de Andrade, J. Herrmann, Y. Dalichaouch, D. Gajewski, C. Seaman, R. Chau, R. Movshovich, M. Aronson, and R. Osborn, Journal of Low Temperature Physics **99**, 223 (1995).

[104] B. Andraka and G. R. Stewart, Phys. Rev. B **47**, 3208 (1993).

[105] H. v. Löhneysen, A. Rosch, M. Vojta, and P. Wölfle, Rev. Mod. Phys. **79**, 1015 (2007).

[106] P. Misra, in *Heavy-Fermion Systems*, Handbook of Metal Physics, Vol. 2, edited by P. Misra (Elsevier, 2008) pp. 51 – 86.

[107] M. A. Continentino, Phys. Rev. B **47**, 11587 (1993).

[108] P. Nozières and A. Blandin, Journal de Physique **41**, 193 (1980).

[109] D. L. Cox, Phys. Rev. Lett. **59**, 1240 (1987).

[110] E. Miranda, V. Dobrosavljević, and G. Kotliar, Phys. Rev. Lett. **78**, 290 (1997).

[111] A. H. Castro Neto, G. Castilla, and B. A. Jones, Phys. Rev. Lett. **81**, 3531 (1998).

[112] O. O. Bernal, D. E. MacLaughlin, H. G. Lukefahr, and B. Andraka, Phys. Rev. Lett. **75**, 2023 (1995).

[113] V. Dobrosavljević, T. R. Kirkpatrick, and B. G. Kotliar, Phys. Rev. Lett. **69**, 1113 (1992).

[114] D. Tanasković, E. Miranda, and V. Dobrosavljević, Phys. Rev. B **70**, 205108 (2004).

[115] E. Miranda and V. Dobrosavljevic, Reports on Progress in Physics **68**, 2337 (2005).

[116] E. Miranda, V. Dobrosavljevic, and G. Kotliar, J. Phys.: Condens. Matter **8**, 9871 (1996).

[117] S. Nakatsuji, S. Yeo, L. Balicas, Z. Fisk, P. Schlottmann, P. G. Pagliuso, N. O. Moreno, J. L. Sarrao, and J. D. Thompson, Phys. Rev. Lett. **89**, 106402 (2002).

[118] S. Nakatsuji, D. Pines, and Z. Fisk, Phys. Rev. Lett. **92**, 016401 (2004).

[119] P. Scoboria, J. Crow, and T. Mihalisin, J. Appl. Phys. **50**, 1895 (1979).

[120] F. Ragel, P. d. V. du Plessis, and A. Strydom, J. Phys. Chem. Solids **71**, 1694 (2010).

[121] S. Nakamura, M. Endo, H. Yamamoto, T. Isshiki, N. Kimura, H. Aoki, T. Nojima, S. Otani, and S. Kunii, Phys. Rev. Lett. **97**, 237204 (2006).

[122] H. Hodovanets, S. L. Bud'ko, W. E. Straszheim, V. Taufour, E. D. Mun, H. Kim, R. Flint, and P. C. Canfield, Phys. Rev. Lett. **114**, 236601 (2015).

[123] Y. Itoh, K. Umeo, and H. Kadomatsu, Journal of alloys and compounds **315**, 11 (2001).

[124] A. P. Pikul, U. Stockert, A. Steppke, T. Cichorek, S. Hartmann, N. Caroca-Canales, N. Oeschler, M. Brando, C. Geibel, and F. Steglich, Phys. Rev. Lett. **108**, 066405 (2012).

[125] G. Knopp, A. Loidl, R. Caspary, U. Gottwick, C. Bredl, H. Spille, F. Steglich, and A. Murani, Journal of Magnetism and Magnetic Materials **74**, 341 (1988).

[126] G. Knebel, M. Brando, J. Hemberger, M. Nicklas, W. Trinkl, and A. Loidl, Phys. Rev. B **59**, 12390 (1999).

[127] A. P. Pikul, C. Geibel, N. Oeschler, M. E. Macovei, N. Caroca-Canales, and F. Steglich, Phys. Status Solidi B **247**, 691 (2010).

[128] K. Hoshino and Y. Kurata, J. Phys. F: Met. Phys. **9**, 131 (1979).

[129] Y. Kurata, J. Phys. F: Met. Phys. **10**, 893 (1980).

[130] S. Burdin and P. Fulde, Phys. Rev. B **76**, 104425 (2007).

[131] R. K. Kaul and M. Vojta, Phys. Rev. B **75**, 132407 (2007).

[132] C. Grenzebach, F. B. Anders, G. Czycholl, and T. Pruschke, Phys. Rev. B **77**, 115125 (2008).

[133] J. Otsuki, H. Kusunose, and Y. Kuramoto, J. Phys Soc. Jpn. **79**, 114709 (2010).

[134] Z.-z. Li and Y. Qiu, Phys. Rev. B **43**, 12906 (1991).

[135] S. Wermbter, K. Sabel, and G. Czycholl, Phys. Rev. B **53**, 2528 (1996).

[136] S. Burdin and C. Lacroix, Phys. Rev. Lett. **110**, 226403 (2013).

[137] I. Lifshitz, Soviet Physics JEPT **11**, 1130 (1960).

[138] N. Read and D. M. Newns, J. Phys. C: Solid State Phys. **16**, 3273 (1983).

[139] D. M. Newns and N. Read, Advances in Physics **36**, 799 (1987).

[140] P. Coleman, Phys. Rev. B **29**, 3035 (1984).

[141] C. Lacroix, Journal of Magnetism and Magnetic Materials **100**, 90 (1991).

[142] A. Georges, G. Kotliar, W. Krauth, and M. Rozenberg, Rev. Mod. Phys. **68**, 13 (1996).

[143] E. N. Economou, *Green's Functions in Quantum Physics*, Vol. 7 (Springer Science & Business Media, 2006).

[144] E. Feenberg, Phys. Rev. **74**, 206 (1948).

[145] P. W. Anderson, Phys. Rev. **109**, 1492 (1958).

[146] R. Abou-Chacra, D. Thouless, and P. Anderson, J. Phys. C: Solid State Phys. **6**, 1734 (1973).

[147] V. Dobrosavljević and G. Kotliar, Phys. Rev. Lett. **71**, 3218 (1993).

[148] V. Dobrosavljević and G. Kotliar, Phys. Rev. Lett. **78**, 3943 (1997).

[149] V. Dobrosavljević and G. Kotliar, Phil. Trans. R. Soc. A **356**, 57 (1998).

[150] E. Miranda and V. Dobrosavljević, Physica B: Condensed Matter **259-261**, 359 (1999).

[151] E. Miranda and V. Dobrosavljević, Phys. Rev. Lett. **86**, 264 (2001).

[152] M. C. O. Aguiar, E. Miranda, and V. Dobrosavljević, Phys. Rev. B **68**, 125104 (2003).

[153] D. Stauffer and A. Aharony, *Introduction to percolation theory* (CRC press, 1994).

[154] V. Shante and S. Kirkpatrick, Advances in Physics **20**, 325 (1971).

[155] B. H. Bernhard and C. Lacroix, Phys. Rev. B **60**, 12149 (1999).